Master's Thesis, Department of Geosciences

Reactions involving S-scapolite and sulphides during reworking of granulite facies anorthosites, Lindås Nappe, western Norway

Jennifer Karin Porter

UNIVERSITY OF OSLO
FACULTY OF MATHEMATICS AND NATURAL SCIENCES

Reactions involving S-scapolite and sulphides during reworking of granulite facies anorthosites, Lindås Nappe, western Norway

Jennifer Karin Porter

Master's Thesis in Geosciences

Discipline: Geology

Department of Geosciences

Faculty of Mathematics and Natural Sciences

University of Oslo

December 2014

Supervisor: Håkon Austrheim

This work is published digitally through DUO – Digitale Utgivelser ved UiO

http://www.duo.uio.no

It is also catalogued in BIBSYS (http://www.bibsys.no/english)

Cover photo: Taken from Espetveit Mine on Holsnøy looking northwest to Hilland Mine on Radøy along the main Hilland fault. The orange waste rock from the mine can be seen in the central-left portion of the picture.

UNIVERSITY OF OSLO

Abstract

The Faculty of Mathematics and Natural Sciences
Department of Geociences

Master of Science

Reactions involving S-scapolite and sulphides during reworking of granulite facies anorthosites, Lindås Nappe, western Norway

by Jennifer Karin Porter

High sulphur scapolite is one of the only minerals stable at lower crustal conditions that contains the volatile species SO_4^{2-} and CO_3^{2-}. S-scapolite is found within granulite anorthosites worldwide, including those in the Lindås Nappe of western Norway. High S-scapolites occur together with Fe-, Cu- and Ni-sulphides in close proximity to known Cu-mineralised occurrences. This thesis studies the relationship between the sulphur in scapolite and sulphides through changes in metamorphic grade and deformation; and whether the break down of scapolite has the potential to contribute to sulphide mineralisation. Textural analysis, field relationships and mineral reactions are studied using electron microprobe images, mineral chemistry and supplemented with stable sulphur isotope analysis.

Two types of granulite facies S-scapolite are identified: within the groundmass of anorthosites, containing 3.8 wt.% SO_3, and within metasomatic veins of anorthosites and jotunites, which consist of up to 7.2 wt.% SO_3. Amphibolite facies scapolites contain less sulphate, between 1.0 and 4.0 wt.% SO_3. At amphibolite facies conditions, sulphate content in scapolite is reduced, and scapolite breaks down with the addition of CO_2 and H_2O, to form epidote or amphibole. Epidote and amphibole, formed after scapolite, always contain micron-sized sulphide blebs within their grain boundaries. Redox reactions through the creation of ferric (Fe^{3+}) iron in forming epidote and amphibole can partially account for the reduction of sulphate in scapolite to form sulphides. The amount of sulphur in S-scapolite accounts for much of the sulphur in the sulphide blebs. With advanced hydration and shearing, scapolite-derived sulphides, together with sulphides from other sources, can be mobilised to form larger mineralisations.

Acknowledgements

I would like to thank the following people plus my friends and classmates for their help with this thesis. Surely without them, my foray back into student life would not have gone as smoothly or been so positive.

Håkon Austrheim - sharing unending enthusiasm, knowledge of your rocks in western Norway, and projecting cheerful patience continually; no one could have a better advisor

Audhild Austrheim - hospitality, room and board in Westlandet, freshly caught crab dinner and wine

Gunborg Bye Fjeld – rock crushing, saw expert, mineral separation lab assistance, including impromptu Norwegian lessons

Muriel Erambert - master of the EMP, extraordinary knowledge of mineral compositions and producer of beautiful and informative element maps

Salahalldin Akhavan - thin section expert and saw-fuse fixer

Harald Strauss - kindly allowing use of the Stable Isotope Lab at the Institut für Geologie und Mineralogie of Westfälische Universität in Münster.

Jan Egil Wanvik at NGU - providing ancient reports on long closed mining operations

Bjørn Jamtveit - helpful comments and suggestions on reaction balancing and geochemistry

Alex Gebhardt and *Lisbeth Langhammer* - translating wartime German geology reports

Niels Warnecke - field assistance, picture taking and overall concern for scapolite

Greg Saunders - amazing ability to waste time playing with MatLab code, in doing so, created some most appreciated programs, making this thesis so much prettier

Contents

List of Figures

List of Tables

Abbreviations

Ab	albite
am	amphibole
AN	anorthosite
An	anorthite
ap	apatite
apfu	atoms per formula unit
BSE	back-scattered electron
bt	biotite
C	Celsius
cc	calcite
chl	chlorite
cpx	clinopyroxene
czo	clinozoisite
DJM	methylene iodide
EMP	electron microprobe
ep	epidote
fsp	feldspar
grt	garnet
ilm	ilmenite
hem	hematite
Kspr	potassium feldspar
ky	kyanite
LILE	large-ion lithophile element
Ma	marialite
Me	meionite

ms	muscovite
NGU	Norges Geologiske Undersøkelse
op	opaque mineral
opx	orthopyroxene
ox	oxide
PDB	Pee Dee Belemnite
pgt	pigeonite
pl	plagioclase
ppl	plane-polarised
ppm	parts per million
px	pyroxene
qtz	quartz
REE	rare earth element
rt	rutile
scp	scapolite
SEM	scanning electron microscope
slv	silvialite
spl	spinel
STD	standard deviation
sul	sulphide
ttn	titanite
vs.	versus
w.	with
wall	wallrock
xpl	cross-polarised
zrn	zircon

Sulphide formulas

chalcopyrtie	cpy	$CuFeS_2$
cubanite	cub	$CuFe_2S_3$
millerite	mil	NiS
pentlandite	pn	$(Fe,Ni)_9S_8$
pyrite	py	FeS_2
pyrrhotite	po	$Fe_{1-x}S$
violarite	vio	$Fe^{2+}Ni_2^{3+}S_4$

Chapter 1

Introduction

1.1 Objective

Scapolite is known to occur in many granulite facies terranes of the world (Coolen, 1982; Hoefs et al., 1981; Okrusch et al., 1979; von Knorring and Kennedy, 1958) as one of the few volatile-bearing minerals stable in the lower crust. Scapolite has three end members in its compositional spectrum: marialite (high Na, Cl), meionite (high Ca, CO_3) and silvialite. High sulphur- and Ca-bearing scapolite, silvialite, is stable at high temperatures and pressures, and is a characteristic mineral in 'dry' granulites world wide. As granulites make up the lower continental crust, the lower crust may constitute an important reservoir for both S and C not previously accounted for in the sulphur and carbon cycles.

Based on a model of the continent crust, the lower crust is 10 km thick and composed of granulites, with 5 modal % scapolite of 5 wt.% SO_3. The middle crust is 5 km thick, composed of amphibolites and 1 modal % scapolite of 2.5 wt.% SO_3. Caquineau (2012) calculated that from this model, sulphur contained in scapolites equals the amount of S present in the oceans. Thus, the composition and amount of scapolites in the lower crust, and their behaviour during metamorphism and metasomatism is critical to obtain a better constrained S-cycle.

As S must be reduced from +6 in scapolite to -2 to enter sulphides, the reactions involving S-scapolite may be of economic importance. Within the studied Lindås Nappe, former important sulphide mines, Hosanger Nickel Mine, and Espetveit and Hilland Cu-mines, are located in S-scapolite bearing granulite (Bjørlykke, 1949; Caquineau, 2012). The latter two mines are located along the same fault zone transecting the granulites.

This thesis presents field, petrographic, mineral chemical and isotope data on scapolite from granulites in the Bergen Arcs. In particular, it focuses on the metamorphic reactions transforming granulites to amphibolites in an area adjacent to the Hilland and Espetveit Cu mines in order to assess the possibility that the sulphur from scapolites contributes to sulphide-mineralisation.

The connection between the sulphur content in scapolite, the metamorphic grade of a rock and its extent of deformation are studied. This connection is tested to assess if, and to what extent, the sulphur content in scapolite contributes to mineralisation along shears and fault zones, as it breaks down from pressure/temperature changes via fluid introduction and/or deformation.

Scapolite is one of the main fluid volatile sources for lower crustal processes involving metasomatism and granulite facies metamorphism (Newton and Manning, 2004). Breakdown of scapolite

to form high fluid pressure may also embrittle the lower crust and explain lower crustal seismicity. Finally, sulphides formed from breakdown of scapolites may influence the electrical conductivity of the lower crust.

If a connection can be made between the presence and composition of scapolite in lower crustal rocks, and its release of sulphur as a sulphide, grade change and deformation, this will potentially have significant consequences on the study of scapolite as it relates to sulphidisation, conductivity and seismicity within rocks formed in the lower crust.

1.2 Geological setting

Western Noway is comprised of a series of nappes of Caledonian (Silurian to Early Devonian) age, thrusted onto Mesoproteozoic Sveconorwegian basement. The study area is located within the Lindås Nappe, in the Bergen Arcs thrust sheets (Figure 1.1). The Lindås Nappe is part of the Middle Allochthon suite and is comprised of anorthosites, gabbros and diorites of the hypersthene-bearing charnockite suite of rocks (Kolderup and Kolderup, 1940). This suite of rocks was formed through magmatic crystallisation in the Proterozoic, between 1 237 and 951 Ma ago (Bingen et al., 2001). The package of rocks underwent granulite facies metamorphism during the Sveconorwegian (Grenvillian) orogeny at approximately 929 Ma (Bingen et al., 2001).

The granulites of the Lindås Nappe have been partly eclogitised, as well as retrogressed to amphibolite facies assemblages, along fractures and shears. Eclogitisation implies that this package of rocks was brought down to high pressure levels, deep in the crust. This has been correlated to subduction of Baltica under Laurentia early during the Caledonian orogeny, between 460 and 420 Ma ago (Bingen et al., 2001; Boundy et al., 1997; Glodny et al., 2008). Amphibolites have been dated as younger than the eclogites, 414 Ma (Glodny et al., 2008); however, this date may represent a separate fluid infiltration event rather than a stage of cooling. The rock packages were consequently detached and brought up into the overlying, and now exposed, succession of rocks in the Lindås Nappe. As a result, a mix of eclogitised and amphibolitised rocks can be found along fractures and shears in the area, together with the older, preserved granulite facies anorthosite-charnockite suite rocks.

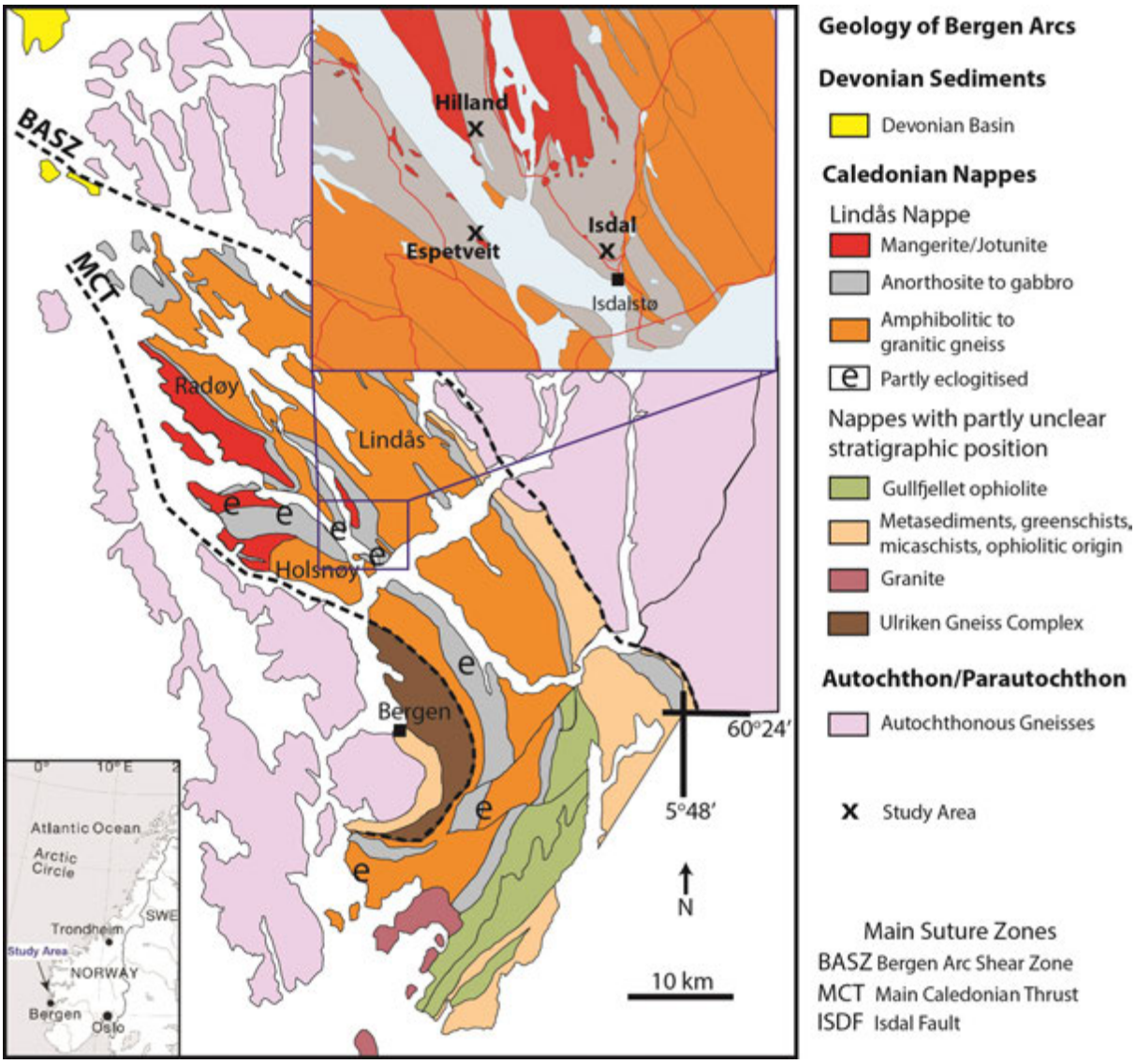

FIGURE 1.1: A location map of the Bergen Arcs area of western Norway, showing the three main studied areas: Isdal, Hilland and Espetveit in the upper inset (modified from Ragnhildstveit and Helliksen (1997)).

1.2.1 Regional geology

The main rock types of the study areas are anorthosites, gabbroic anorthosites, and anorthositic gabbros of granulite facies to amphibolite facies mineralogy. The granulites are thought to have formed at 800-900°C and at <10 kbars (Austrheim and Griffin, 1985), or approximately 60 km depth. The formation of the granulite event is estimated to have concluded by the end of the Sveconorwegian orogeny. The granulites exhibit a texture of a pyroxene core surrounded by plagioclase, then garnet concentric rings, or coronas. The coronas are thought to form from an

anorthositic gabbro parent, through two sub-solidus stages creating two pyroxenes: orthopyroxene (opx) and clinopyroxene (cpx), along with garnet (grt) from olivine and plagioclase (pl) (Cohen et al., 1988). The age of the coronas is calculated to be between 905 and 912 Ma, which is indistinguishable from the age of the formation of the granulites themselves.

The granulites have been partially eclogitised, as well as amphibolitised, along shears zones that can be anastomosing and of variable thickness, ranging from centimetres to 100 metres across. These shears can act as a sharp boundary between the different metamorphic grades, and allow for these processes to occur over as little as centimetre distances (Austrheim, 1990). Eclogites are found on the islands of Holsnøy and Radøy, as wells as the western part of Lindås, some of which have been retrogressed to reflect amphibolite facies conditions. The foliation of the amphibolite and eclogite facies shear zones is aligned with the Bergen Arcs. The eclogite and amphibolite deformation has been dated using Rb-Sr to approximately 400 Ma, which is coincident with the emplacement of the Bergen Arc nappes during the Caledonian orogeny (Austrheim and Griffin, 1985; Cohen et al., 1988).

It has been proposed that the time taken to eclogitise and amphibolitise the granulites in the Lindås Nappe is as short as 13 Ma (Camacho et al., 2005). $^{40}Ar/^{39}Ar$ studies show that the subduction and exhumation had to have been faster than the thermal equilibration of the rocks, and the temperatures would have been less than 400°C. This theory could explain why the eclogite and amphibolite facies rocks occur with the original granulites in a meta-stable configuration, and why some of the granulite blocks underwent brittle deformation. In this case, the amphibolites in the Lindås Nappe are thought to be contemporaneous in formation with the eclogites.

Another proposal by Roffeis et al. (2012) suggests there is a gradient in pressure increasing from east to west and the eclogites are confined to the western part of the Nappe, predominately on Holsnøy. If this is the case, the amphibolites in the east are younger, as proposed in Glodny et al. (2008). They claim the Rb-Sr isochron ages, 414.2 ± 2.8 Ma, date a fluid-induced recrystallisation event, not a stage of cooling. In either case, the rocks of the Hilland and Espetveit areas studied for this thesis fall on the boundary between the eclogite and anorthosite zones, as both mineralogical assemblages are found.

The amphibolite facies mineralogy of the anorthosite rocks consists of plagioclase (from An_{30} to An_{65}), chlorite, hornblende, apatite, epidote and minor biotite, dated to 407± 7 Ma (Austrheim and Griffin, 1985). The more evolved mangerite, which contains K-feldspar and Fe-Ti

oxides in the granulite stage, develops more biotite, titanite and rutile during amphibolite facies retrogression; and when deformed, becomes a micaceous gneiss.

The amphibolite mineralogy occurs both within shear zones, and outside as a 'static' recrystallisation (Austrheim, 1978). The amphibolite foliation within shears is truncated and discontinuous. The change in mineralogy is associated with a change in colour from a lilac-grey to a bright white. It has been estimated that approximately 90% of the anorthosites in the Lindås Nappe have been amphibolitised (Mukai et al., 2014). The change in mineralogy of the shear zones to a different facies, and the shear zones' close proximity to, and sharp contact with, the granulite facies mineralogy leads to believe that the deformation of the rock aided in the reactions, taking pseudo-stable mineral assemblages into a mineralogical assemblage in equilibrium with the external conditions. Reduction of grain size and increase in surface area, coupled with an introduction of fluids into assessable pathways are thought to contribute to the onset of mineralogical reactions (Austrheim and Griffin, 1985).

In this thesis, the granulite transition to amphibolite facies anorthosite, coupled with other constituents of the hypersthene-bearing anorthosite-mangerite-charnockite suite rocks, are studied. Scapolite exists as a minor constituent in the original granulite facies anorthosite and gabbro-anorthosites, as well as in cross-cutting veins across regional faults and localised shear zones.

Also within the study area, many mineralised zones exist that are located along these faults and shear zones. These mineralisations include former copper and Fe-Ti mines. This study has been carried out to include two formerly worked copper mines along one of these regional faults, with a comparison done with other faults along which no economic mineralisations have been identified.

1.2.2 Mine site geology

Two former mine sites lie within the survey areas. The first is near the village of Espetveit on the eastern shore of Holsnøy (Figure 3.7). The second is found near the western shore of Radøy, at the northern end of Hillandsvatnet (Fig. 3.5). Both occur along the same northeast trending fault which cross-cuts the region, and can be traced across several islands (Fig. 2.1).

Both the Hilland and Espetveit Mines lie on the same northeast trending structure, and within fault-associated quartz-rich breccia. They were mined by Welsh workers of same company, 'Norway Copper Co.', from 1879-83. More resources were invested in Espetveit, but they lost

money until the declaration of bankruptcy in 1883 (Fasting, 1909). A connection between the Hilland Mine on Radøy, and Espetveit Mine on Holsnøy was noted by the early miners, as the mineralised zones lie on the same northeast trending lineament. This connection was limited, however, to observation. No further studies were done regarding any connection between the mines as they were of limited economic interest.

The Espetveit mine has also been referred to in NGU reports as the Adelaid(e) Mine (Fasting, 1909; Sandvik, 1977). Two water filled shafts and one adit can be seen today, built on the same quartz-rich zone that strikes 030°, coincident with the main strike of the fault. The main shaft lies 400 m from, and 50 m above sea level. It was sunk to 70 m and served as a base for transverse digging. The quartz vein is nearly vertically dipping, up to 2 metres wide containing sulphides, of which half were pyrite, the other half chalcopyrite. The main commodity of interest was copper, found within extremely irregular flecks of chalcopyrite (cpy) in quartz. The grade was estimated to be 0.25% Cu, though miners noted richer amounts of ore were found where the vein dip was less steep. Not much ore remained in the adits by 1909.

The mine site to the northwest of the lake Hillandsvatnet on Radøy has been referred to as Hillandsklubben, Grønskaret and Gangstøen (Fasting, 1909; Haber, 1940; Sandvik, 1977) in the mining reports. These may refer to different adits or shafts of the same mineralised zone, but in this thesis, are collectively referred to as the Hilland Mine for simplicity. Only one water-filled vertical shaft was found in the area during field investigations.

The Hillandsklubben mine is described as having as an average copper grade of less than 1% over a 2 to 3 metre thickness, with rich ore samples analysed at 1.4% Cu (Sandvik, 1977). All other metal concentrations were found to be negligible. Copper mineralisation was within 0-0.5 m wide sporadic veins, containing mainly uneconomic quantities of chalcopyrite. The shaft is reported to lie 500 metres SE of Grønskaret, but is currently flooded and; therefore, unobservable.

Grønskaret Mine, what is believed to be the main mine site, lies on the same lineation as Espetveit, striking 30° NE (Fasting, 1909). There was an adit and a shaft at surface, though only the shaft remains, and is now inaccessible. The shaft reportedly was 20 m deep, and had at least 3 different horizontal adits dug in search for the continuation of the main vein; which lies approximately 6-8 metres below surface. The mineralisation found in quartz veins was predominantly chalcopyrite and pyrite. The quartz veins strike 10° NE and dip 70-80° to the west, are irregular and are rarely over 0.5 m thick. Approximate Cu percent was estimated

to be 0.5% (Fasting, 1909). The mineralisation was reported to be poorly formed grains of cpy, up to 1 cm in size (Haber, 1940).

A 15 m deep, NNE trending shaft was built at Gangstøen (Haber, 1940). Ore was hosted in a 1-2 m wide, nearly vertical, quartz-filled vein, dipping steeply to the south, on a significant fault. The vein could be seen and followed in a limited fashion along the direction of the fault toward the Espetveit Mine across the water. Occurrences of chalcopyrite were not of mineable quantities, and frequent secondary malachite mineralisation was seen at surface (see Page 23).

1.3 Scapolite

Scapolite is a feldspathoid similar to a plagioclase, forming a solid-solution series with Na and Ca end-members, marialite (Ma) and meionite (Me): $Na_4Al_3Si_9O_{24}Cl$ and $Ca_4Al_6Si_6O_{24}CO_3$. Ca may be replaced by Sr and K, and carbonate may be substituted with SO_4 in the meionite. Like feldspar, scapolite is a tectosilicate, but forms in environments that are silica deficient. The main difference in its structure is the presence of a large space between the tetrahedra of AlO_4 and SiO_4 into which large anions of primarily SO_4^{2-}, CO_3^{2-} and Cl^- can be accommodated. A figure demonstrating the structure of sulphur-rich scapolite, silvialite, is shown in Figure 1.2.

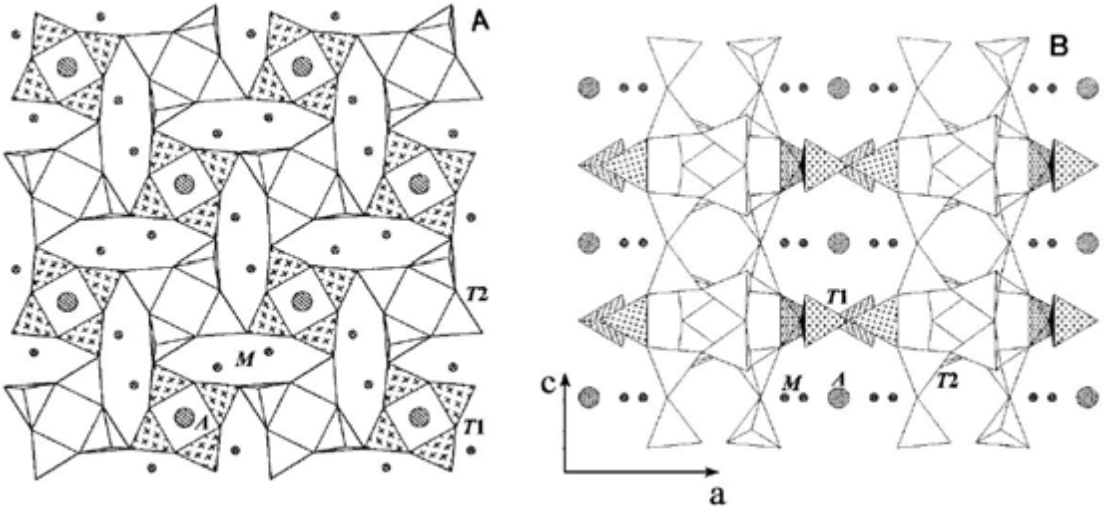

FIGURE 1.2: The structure of a silvialite crystal showing the Si and Al tetrahedra, the 'A' site containing the anions SO_4 and CO_3 (large circles) and the 'M' site containing the Ca and Na atoms (small circles). (A) Left is a view perpendicular to the *c*-axis and (B) Right is perpendicular to the *a*-axis, from Teertstra et al. (1999).

The generalised formula for scapolite can be expressed as $M_4Z_{12}O_{24}A$. Like the plagioclase series, the framework of scapolite consists of tetrahedral sheets with Si or Al in the tetrahedral

cation position (Z). These cations sum to 12. The M position is the sum of Ca, Sr, Na and K, and is equal to 4. The anion position is a large space filled with primarily Cl^-, CO_3^{2-}, SO_4^{2-}, though minor OH^- and F^- can also exist in this site. Due to its similarity to the plagioclase series, the chemical formula for scapolite can also be written as $3NaAlSi_3O_8$ (or 3Ab) + NaCl for marialite, and $3CaAl_2Si_2O_8$ (or 3An) + $CaCO_3$ for meionite.

There is a coupled substitution between the two end-members up to Me_{75}, where Na_3Si_2Cl is substituted with $Ca_3Al_2CO_3$. For values between Me_{75} and Me_{100}, the replacement changes to $NaCa_3Al_5Si_7O_{24}CO_3$ and $Ca_4Al_6Si_6O_{24}CO_3$ through exchange of NaSi and CaAl, as in plagioclase (Evans et al., 1969). For the values of meionite above Me_{75}, anion exchange is complete.

A negative correlation was found between Ca content and Si atoms, and a similar, but positive correlation between Si and Na; as there is coupled substitution of Na and Si with Ca and Al. Charge balance between these elements is also obtained through exchange of divalent ions, CO_3^{2-} and SO_4^{2-}, with Cl^-. However, there is not as strong a correlation between S and C ions with Ca, as reported by Evans et al. (1969). They also present the definition of Me content to be Ca/(Ca+Na), in which marialite is Me_{0-25}, dipyre is Me_{25-50}, mizzonite is Me_{50-75} and meionite is Me_{75-100}. In this thesis, this definition of Me content is used, but as most of the samples in this area are mizzonite in composition, for simplicity, meionite is used to express samples from $Me_{(50-100)}$ and marialite is used for Me_{0-50}.

1.3.1 Silvialite

Silvialite is the sulphate rich end member of the meionite series described by Teertstra et al. (1999). The CO_3 in the meionite structure is substituted with SO_4 in the anion site, giving the end-member formula $Ca_4Al_6Si_6O_{24}SO_4$. Sodium does exist within its structure; however, as the chemical make-up is closer to that of mizzonite. Teertstra et al. (1999) gave the definition of silvialite as having over 50% of the anionic site filled by sulphate. Work completed by Chappell and White (1968) and confirmed by Lovering and Widdowson (1968) determined the sulphur occupies the anion position as the sulphate (SO_4^{2-}) radical.

Silvialite can occur as an upper-mantle garnet-granulite xenolith, and is documented as a primary cumulate phase in an alkali basalt at high temperatures and pressures (900-1000°C and 8-12 kbars) (Teertstra et al., 1999). Silvialite is generally associated with plagioclase of An_{45}, cpx, pyrope almandine garnet ($Pyr_{44}Alm_{40}Grs_{16}$), spinel and calcic amphibole. The calcium

content in the plagioclase found with silvialite is similar to, or lower than that of the silvialite. The highest recorded and published sulphur content in S-scapolites was found at Furua, Tanzania, at 6.4 wt.% SO_3 (Coolen, 1980; Hoefs et al., 1981).

1.3.2 Occurrence

Generally, scapolite is considered to be a metamorphic or metasomatic mineral. Marialite, the Na and correspondingly Cl-rich end member, has been found within sediments in which albitisation has taken place, or in which the host rock has been infiltrated with Cl-rich fluids, such as those found in Kragerø, Norway (Engvik et al., 2011, 2008). Many occurrences of Cl-rich scapolite form in calc-silicates, dolomites, marbles, evaporites or regions of metamorphism in calcareous rocks or alkali metasomatism (Serdyuchenko, 1975). Scapolite has also been observed within a chondritic meteorite (Alexander et al., 1987), although this is likely due due Cl-metasomatism. It has been described in these situations as a sensitive indicator of metasomatic fluid composition (Jiang et al., 1994).

Scapolites described as meionitic are found in granulites, such as those in the Grenville Province in Canada, and the Bergen Arcs of Norway (Moecher et al., 1992). Harley and Buick (1992) recorded the presence of a Ca-CO_3-rich scapolite in calcsilicate rocks in East Antarctica.

Sulphate-rich scapolite, or silvialite, is also of restricted provenance, occurring in granulites in Queensland (Rudnick and Taylor, 1987; Stolz, 1987; Teertstra et al., 1999) and within other granulites such as Tanzania (Hoefs et al., 1981) and on the Kola peninsula (Rozen et al., 1977).

Although considered a metamorphic mineral, scapolite has also been described as primary in tephra megacrysts in Chaîne des Puys, France and Hoggar, Algeria (Boivin and Camus, 1981), and in pegmatites in New Zealand (Blattner and Black, 1980). The sulphate-rich scapolite of the Whitestone Anorthosite of Canada has also been described as texturally primary (Moecher et al., 1992). High sulphur meionitic scapolite described by Boivin and Camus (1981) as the primary mineral in volcanic tephra, is sourced from high-pressure phenocrysts, from magma of hydrated upper mantle. They postulate that due to the relative scarcity of scapolite as a primary phase, the conditions leading to its precipitation would have been nearly unique.

Meionite, the carbonate end member, is stable only at temperatures above approximately 800°C and over most pressures (Goldsmith, 1976), see Figure 1.3a. Newton and Goldsmith (1975) found that meionite can be stable to very high pressures and temperatures (3 GPa and 1500°C).

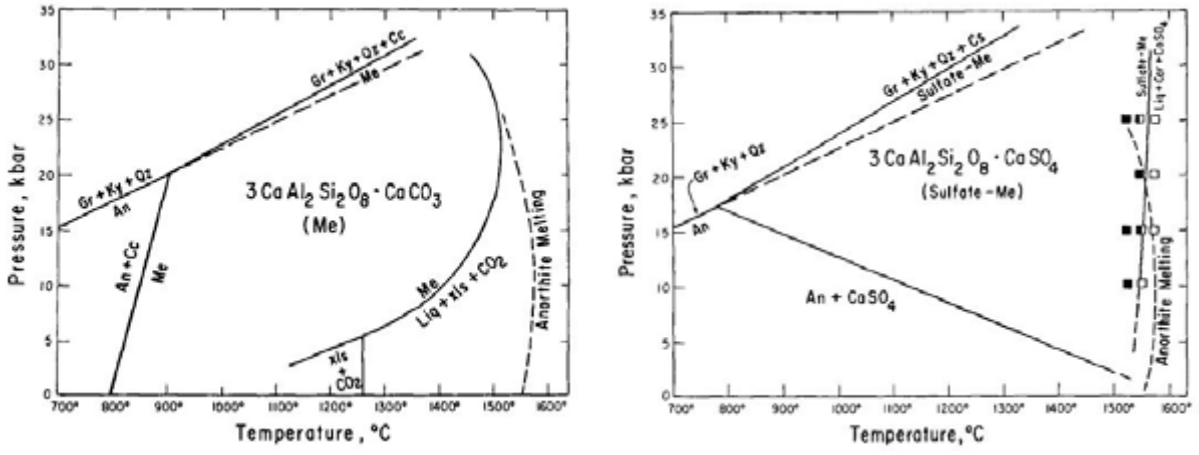

(A) (B)

FIGURE 1.3: A) The stability field of meionite showing it is stable above 800°C. Anorthite is the low temperature and pressure phase, existing with calcite below this temperature. The upper limit shows the breakdown of Me to grt + ky + qtz + cc above 20 kbars at 900°C. B) The stability field of silvialite showing the sulphate scapolite end member is stable at even higher pressures than that of meionite. Figures are from Goldsmith (1976).

Kwak (1977) and Chappell and White (1968) found evidence for the occurrence of SO_4^{2-} in scapolite increases as a function of temperature. Goldsmith (1976) confirmed this experimentally, showing that stability of silvialite is actually at higher P and T than meionite (see Fig. 1.3b). Also above 20 kbars, it melts at higher temperatures than anorthite. The stability of scapolite falls within conditions of crystallisation as a primary phase.

Scapolites are not stable as an eclogite mineral phase. Carbonates and sulphates found in eclogite mineralogy in the Bergen Arcs are thought to come from the breakdown of granulite facies scapolites (Boundy et al., 2002), as pressure increased to eclogites facies conditions.

1.3.2.1 Granulites

Scapolite is present in many granulite rock packages, including the Grenville Province, Canada, the Furua complex, Tanzania (Coolen, 1980; Hoefs et al., 1981), East Antarctica (Harley and Buick, 1992), McBride volcanic province Queensland, Australia (Rudnick and Taylor, 1987), Kola Peninsula, Bergen Arcs, and the Western Gneiss region of Norway (Austrheim et al., 2003), among others. The composition of the majority of scapolites within these terranes is sulphate-rich meionite.

Granulites have been noted as important lower crust constituents. Many granulites contain scapolite, which is known to occur as both primary and secondary phases (Lovering and White, 1964). It has been noted that scapolite is the mineral in the lower crust containing the greatest quantities of volatiles, such as C, S, Cl, F and OH within its structure (Coolen, 1982; Goldsmith, 1976). Consequently, presence of scapolite may have a significant impact on metasomatism and ore-forming activity in the continental crust.

Lovering and White (1964) noted that the percentage of sulphur within the structure increases with metamorphic grade, and attempted to predict metamorphic grade based on sulphur content. They suggested that the lower crust, specifically beneath Australia, could be as much as 5% primary scapolite. Also noted was the calcium to sodium ratio in plagioclase was likely based on the mineral assemblages with which plagioclase formed; whereas the Ca/Na ratio in scapolite was likely predicated on metamorphic grade. They suggested that the occurrence of high sulphur scapolite is restricted to granulite facies rocks.

1.3.2.2 Amphibolites

Amphibolite facies rocks are also known to contain scapolite, though at a lesser Me content, ie: at Mary Kathleen, Queensland, Australia (Ramsay and Davidson, 1970). Here it was found that scapolite from calcareous rocks contained a higher Na content than metavolanics. The postulation being that the volatile content in the rock fluids was the determining factor in the composition of the scapolite, not the rock composition itself. The fluids affected the scapolite composition in a way that was dependent on whether the system was open or closed, and whether volatiles cold be sourced outside the immediate rock package.

The Mt. Lofty area of Australia also contains scapolite, forming in amphibolite-greenschist facies rocks with low sulphur values (Kwak, 1977). Kwak (1977) also found a systematic increase in the Me content of the scapolite as metamorphic grade increased from greenschist through upper amphibolite metamorphism, from Me_{50} to Me_{66}.

1.3.3 Mineralisation

Scapolite has been reported from a number of economically interesting mineralised occurrences. Many skarns have been described, such as the Sangan iron deposits in Iran (Boomeri et al., 1997), and the Fe-Cu-Au skarn in Missouri (Lowell and Noll Jr, 2001). The scapolites in these

deposits are of high Cl content, reflecting the high X_{NaCl} in the formation fluids. Scapolite is also found in Fe-ore and magnetite deposits in Sweden and Russia. The scapolite here is found with the ores, and deposited simultaneously as replacement reactions with the host rock (Ekström, 1972).

Scapolite has been described as being directly related to the formation of sulphide deposits in Kiruna, northern Sweden (Romer et al., 1996) and the Pb-Zn deposit in Qinling China (Jiang et al., 1994). It forms as a replacement of plagioclase, in small veins, porphyroblasts and as alteration halos. Sources of the scapolite within these complexes are suggested to be either from infiltration of Cl-rich brines or the reaction of plagioclase with calcite and halite (Frietsch et al. (1997) and references therein). Austrheim et al. (2008) report Cl-scapolite from the Langøya Fe-mines of southern Norway.

High S-scapolites are found in nickel and gold deposits in Canada. Both are skarn deposits that formed sulphide-gold ore bodies. There was no direct relationship found linking the Cl content and the Ca:Na ratio of the pre-existing host rock (Pan et al., 1994).

The scapolite in the Mt. Lofty area, South Australia (Kwak, 1977) is associated with copper sulphide mineralisation. This scapolite is of the Cl-rich variety, and he noted that the sulphur content in the scapolites was consistently low despite being in contact with sulphide mineralisation. Kwak (1977) found it 'remarkable' that scapolite found associated with sulphide veins (also containing calcite) had no sulphate in its structure. He attributed the low sulphate content to the low metamorphic grade of the mineralised rocks.

Serdyuchenko (1975) noted that Archean terranes derived from evaporites, such as anhydrite, or other sulphates and salts, may be the source to the scapolite found in present day metasediments in areas such as those in Scandinavia, the Canadian shield and Australia, as these rocks are associated with mineralisation. He postulated that high-S scapolites formed from sulphate deposits are of special interest because they may contain enough sulphur to be released under certain conditions and re-deposited as sulphides.

The predominant amount of literature describing scapolite-ore body associations, describe it as a syn-depositional to post-depositional mineral. The first person to recognise that high sulphur scapolite bearing granulites could be a source for sulphide mineralisation was Wilson (1969, 1974). He recognised shear zones within these terranes could introduce water into the granulites at lower metamorphic grade. This lowers the stability of sulphate within the scapolite

structure, freeing the sulphur to potentially combine with metals, such as Cu, to form sulphides. He proposed that the Cu can be sourced from the opx within the granulites.

1.4 Fluids and deformation

To transform a granulite facies rock with anhydrous minerals to eclogites or amphibolites with abundant hydrous phases, addition of water is required. Reactions can be independent of the original mineralogy, dependent on the fluids penetrating the rock and the conditions of deformation, ie: sheared anorthosite and mangerite will eclogitise at the same external conditions (Austrheim, 1987; Austrheim and Griffin, 1985). Element exchange involved in these reactions is controlled by fluids using the shear zones as conduits of movement. Any change in fluid composition, including volatile content, such as CO_3^{2-}, Cl^- and SO_4^{2-}, has a large effect on the resultant composition. Fluids move more quickly through the rock package during metamorphic events (Bickle and Mckenzie, 1987). A fluid-driven reaction front exists, evidenced by the sharp boundary between local areas where fluid is able to infiltrate; and in some cases, fluids are observed to penetrate 0.5 m into undeformed anorthosite along grain boundaries and fractures (Mattey et al., 1994).

How fluids move through impermeable rocks such as crystalline granulites, and how the fluids affect rock strength and rheology of the rock have been studied in the Bergen Arcs by Mukai et al. (2014) and Boundy et al. (1992). Fluid infiltration along shear zones is of special interest in this area as it is likely that localised and directed fluid infiltration controlled the amphibolitisation or eclogitisation of the granulites (Austrheim and Griffin, 1985), changing the grade of the rock along specific channels and introducing hydrated mineral assemblages, stable under differing pressure and temperature conditions.

Metasomatic processes have been used to describe changes in rocks via fluid induced, and couple dissolution and reprecipitation reactions (Putnis, 2002; Putnis and Austrheim, 2010). Albitisation and scapolitisation are processes through which whole and partial rock replacement has occurred. Fluids introduce ions such as Na, K and Si and replace them with Ca and Al, through structurally controlled fluid movement, restricted along fractures and structural weaknesses. Plagioclase can alter to scapolite, through processes related to dissolution and reprecipitation (Engvik et al., 2009; Putnis and Austrheim, 2010).

Important characteristics of dissolution and reprecipitation reactions described by Engvik et al. (2008) include an increase in porosity within the produced minerals, a sharp reaction front, and a preservation of parent mineral dimensions and crystallographic orientation. These processes are lithologically independent and controlled primarily by structure. They noted that the metasomatic fronts occur progressively outward from, and normal to, fractures.

Mineralisation and ore bodies are known to be associated with albitisation and scapolitisation (Engvik et al., 2008). The fluids and conditions that remove Ca and Al from a system, also have removed Fe and Ti, allowing for concentration of these ions as ore-forming bodies. Scapolitised bodies are then depleted in Fe, Ti and heavy metals.

1.5 Stable isotope geochemistry

Sulphur isotopes are used to investigate the provenance of sulphides in ore deposits because sulphur is both an important constituent in the mineralisation and a ligand that transports metals. Sulphur occurs in every natural environment, including granulites; therefore, investigating properties of this sulphur provides knowledge of its origin. Sulphur isotopes can give information regarding the origin and temperature of formation fluids of a rock or ore deposit, the composition of the hydrothermal fluid of the depositing the minerals, and conditions of deposition, pH and fO_2 (Hoefs, 2009).

Sulphur has four naturally occurring isotopes: ^{32}S (the most abundant at 94.93%), ^{33}S, ^{34}S (the second most abundant at 4.29%) and ^{36}S (Rosman and Taylor, 1998). The isotopic composition of a substance is given as:

$$\delta^{34}S = \left[\frac{(^{34}S/^{32}S)_{sample} - (^{34}S/^{32}S)_{standard}}{(^{34}S/^{32}S)_{standard}}\right] * 10^3‰ \tag{1.1}$$

The traditional standard used to compare the sulphur ratios has been from the triolite (FeS) of the Canyon Diablo meteorite (CDT). Small inconsistencies of up to 0.4‰ δ^{34}S in the CDT have led to the development of a new standard called Vienna-CDT (Hoefs, 2009).

Figure 1.4 shows the wide range of δ^{34} S values that can exist in certain environments, though generally, a high positive δ^{34}S value indicates surface water infiltration, such as sea water or from evaporites. According to Faure and Mensing (2005), ore deposits formed in igneous conditions have δ^{34}S values nearing 0 ‰ δ^{34}S.

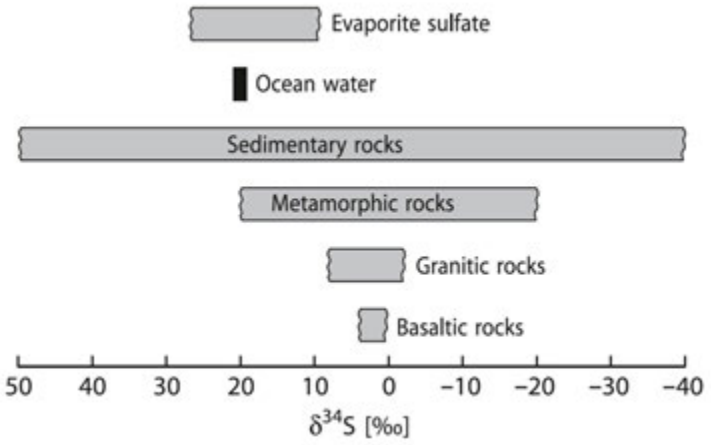

FIGURE 1.4: Typical δ^{34}S values of specific geologic sulphur reservoirs (Hoefs, 2009).

Sulphur in the magmatic system is quite complex as it occurs as sulphate and sulphide minerals, as well as a gaseous phase of more than one species (SO_2, H_2S). Sulphur can also go preferentially into an immiscible sulphide phase of melt, or stay dissolved within the main melt phase.

Oxygen, carbon and sulphur isotopes of scapolite bearing rocks, and their changes from granulite facies to eclogite or amphibolite facies rocks, through fluid infiltration and deformation have been studied by many researchers (Evans et al., 2014; Hoefs et al., 1981; Mattey et al., 1994; Van Wyck et al., 1996; Yoshino and Satish-Kumar, 2001). Their studies provide information on global earth processes, identifying fluid sources, such as from mantle or crustal sediments, and their possible subduction and reintroduction into the lower crust.

For example, Yoshino and Satish-Kumar (2001) theorise, based on carbon isotopes from carbon-rich scapolites of the Koistan Arc in Pakistan, the C-scapolite formed in the mid-crust and were sourced from juvenile mantle. The associated sulphate-rich, lower crustal scapolites exhibit heavier δ^{13}C isotopes, suggesting sources of carbon from carbonates subducted to deep levels in the crust.

The scapolite granulites in Furua Tanzania, in which scapolite makes up to 30 vol.%, were shown to have 0.3 to 3.6 ‰ δ^{34}S (Hoefs et al., 1981), which is also indicative of a deep mantle source. These rocks were formed between 750 and 850°C and 0.7-1.1 GPa. Also noted, the δ^{34}S increases in the greenschist and amphibolite facies, to +15.7‰, also a function of source, not metamorphic grade, as the rocks were derived from evaporites (Hoefs et al., 1981).

Evans et al. (2014) recognise the importance of sulphur isotope studies in identifying the source of fluids and the geometry of fluid flow from subducted sediments in eclogite and blueschist facies mineral assemblages.

Carbon isotopes in the Bergen Arcs area have also been studied. The meta-anorthosites of the Bergen Arcs gave $\delta^{13}C$ values of -6.8 to -2.7‰ PDB, which indicates the CO_2 is derived from a mafic melt emplaced in the lower crust or upper mantle (Moecher et al., 1994). Specific to the study area, Van Wyck et al. (1996) studied the oxygen isotopic compositions of eclogites and granulites on Holsnøy, finding there was disequilibrium during eclogitisation. They postulated there have been at least two stages of fluid infiltration based on carbonate isotope data, with calcite precipitation during retrograde metamorphism. The fluid source for the retrogression is not local, but derived from dewatering sediments, possibly from underlying, less deformed rock units (Van Wyck et al., 1996).

Shear zones on Holsnøy mark a sharp reaction front from granulite to eclogite facies metamorphism. Conditions of eclogitisation are constrained to 700°C and over 1.7 GPa pressure. Eclogitisation introduced H_2O-rich fluids which penetrated 0.5 m into the original granulite, away from shears (Mattey et al., 1994). Garnets preserved fluids from the original anorthosite with an isotopic composition of a mantle source. Fluids associated with eclogites and retrogressed eclogites are isotopically distinct. Non-deformed anorthosite was found to be impervious to CO_2-rich fluids, which resulted in a distinct isotope front. The strong front marks how far CO_2 was able to penetrate the wallrock, and is limited to only wallrock that was being deformed (Mattey et al., 1994). Within the eclogites of Holsnøy, this changed the $\delta^{13}C$ signature from mantle source, to +9‰.

Chapter 2

Methodology

2.1 Field data acquisition

During the periods 22.08.13 through 24.08.13, and 10.07.14 through 13.07.14, geological fieldwork was carried out on the islands of Holsnøy, Radøy and Lindås in the Bergen Arcs, approximately 30 km north of Bergen in western Norway. Fieldwork included mapping of geological contacts and recording structural relationships in detail around the Hilland and Espetveit Mines. Supplemental mapping was carried out along structures at a regional level within the Bergen Arcs. Hand samples were collected at the Hilland, Isdal and Espetveit locations. All mapping points, geological and structural data, and sample locations are plotted in Figures 2.1, 3.2, 3.5 and 3.7.

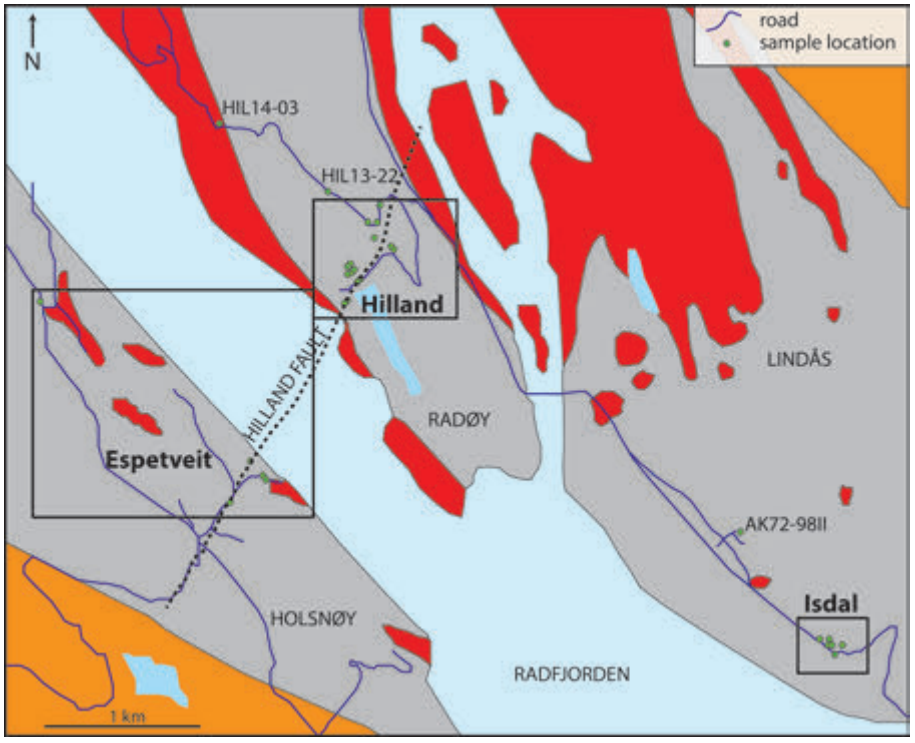

FIGURE 2.1: A location map of the three studied areas, indicated as black boxes the areas of Hilland, Isdal and Espetveit. Detailed versions of these maps are shown in Figures 3.2, 3.5 and 3.7, respectively. Regional geology is as in Figure 1.1.

In total, 59 rock samples were taken over the 2013 and 2014 field seasons: 12 at Isdal, 32 at Hilland and five at Espetveit. A further 11 samples were taken during regional mapping for supplementary study. For a list of all samples taken, their locations and a brief description of each, see Table A.1 in Appendix A.

2.2 Sample preparation

Selected rock samples were chosen for specific studies, analysing methods were determined and samples were prepared for analysis accordingly. Samples to be analysed by thin section were cut and given to the thin section lab at the University of Oslo, Department of Geosciences, for preparation. Polished thin sections of approximately 30 μm thickness were produced for optical microscope and electron microprobe (EMP) analysis.

2.3 Optical microscopy

Thin sections were used for silicate and sulphide investigation under a transmitted and reflected light microscope. Mineralogy, textural and structural relationships were recorded. Photographs were taken, saved electronically and specific thin sections were chosen for further study with the EMP.

2.4 Electron microprobe

Thin sections were analysed using a Cameca SX 100 Electron Microprobe at the University of Oslo. The electron microprobe (EMP) uses electrons emitted by a heated tungsten filament, through a narrow opening of a Wehnelt cylinder held at negative potential. The electrons are accelerated down a column toward a sample specimen using a voltage differential created by an anode plate. The electrons are focussed in the column with electromagnetic lens condensers which determine the amount of current, angle and diameter of the beam directed at the sample. The electron beam hits the sample, exciting electrons within an atom, and given enough energy (in kV), it 'kicks out' inner shell electrons of the atom. These electrons are replaced by others in different electron shells. This process emits a characteristic X-ray proportional to the energy difference in the electron shell energies (ie: a $K_{\alpha 1}$ X-ray is emitted when an electron moves from the L_{III} to K shell).

The EMP is used to do a quantitative analysis of the elements in a sample. This is accomplished using wave dispersive spectrometry (WDS). WDS is based on Bragg's Law ($n\lambda = 2d\sin\theta$) whereby X-ray waves of a certain wavelength θ diffract through a crystal with constructive interference at a certain angle θ. Each element has a unique wavelength that diffracts at a different

angle θ. The angle at which the wavelength diffracts is dependent on the d-spacing that is unique to each crystal. Crystals of different d-spacings are needed to detect elements of increasing light to heavy atomic (Z) values. A back scattered electron (BSE) image then can be analysed for minerals of lighter element total compositions as appearing darker, ie: plagioclase, and minerals containing higher total atomic number totals appearing lighter, ie: sulphides.

The EMP used for this analysis has five different crystal spectrometers, each with 2 to 4 crystals that can be exchanged according to the elements that need to be analysed. Each crystal has a different d-spacing in its lattice. The LTAP crystal is used to analyse for Na, another for Si, Al and Mg. One PET crystal detects Ca, whereas another LPET crystal analyses K and Ti. A LLIF crystal analyses for Fe, Mn and Cr. Using crystals of different d-spacings simultaneously allows a more efficient use of the machine and less analysis time.

A BSE image is also used to give a quick visual scan of the specimen and supplement information obtained from the light microscope by giving more detail about mineral zoning, textures and mineral identification through grey-scale contrast. A quick scan of the specimen with the Energy Dispersive Spectrometer (EDS) helps to determine which elements should be used for an in-depth analysis. A mineral is analysed quickly with the EDS for mineral identification and to assess the need for analysis using WDS with the pre-selected, calibrated element standards and accompanying crystals. For most WDS readings, a current of 15 nA and a voltage of 15 kV was employed with 10 second integration times. For trace element analysis, such as Ni and Cu, the current was increased to 200 nA, the accelerating voltage remained at 15 kV and total time was increased to 8 minutes for each point. Different major element compositions were used for matrix corrections for the different analysed grains.

2.5 Stable isotopes

In preparation for stable isotope analysis, rock samples were cleaned and placed in an ultrasonic bath to remove all possible contaminating particles. The rocks were crushed, first with a sledge hammer, then with a vibrating steel ring crusher in preparation for mineral separation.

The sample was processed further using magnetic Frantz separators. The sample was separated depending on the overall magnetic content; first using magnetic free fall to remove the most magnetic minerals, such as magnetite and garnet. The remaining sample was separated using a Frantz magnetic separator table tilted at a 15°angle at progressively stronger amps from 0.4

A, 0.6 A, until the sample size was appropriate for high density liquid separation. The tilted magnetic table removed the less magnet minerals such as typical mafics, hornblende and biotite.

Methylene iodide (CH_2I_2) or DJM, with a density of 3.2-3.3 g/cm^3, was used as the heavy liquid in the density separation process. As scapolite was the mineral of interest, the samples were separated emphasising the importance of the lower density fractions.

The sample was placed inside a seperatory funnel containing DJM. It was shaken several times to ensure all grains were in the liquid and was set to allow slow falling minerals to sink. The heavy fraction was syphoned out of the liquid. Acetone was added to the DJM allowing progressively lighter fractions to separate from the sample. The lightest samples were observed under microscope to ensure scapolite was collected; and from the heaviest separates, the sulphides were collected.

These samples were sent to Harald Strauss of the Stable Isotope Laboratory at the Institut für Geologie und Mineralogie of Westfälische Universität in Münster, Germany for investigation. The mineral separates were mixed with V_2O_5 in tin cups. They were then combusted in an elemental analyser interfaced to a ThermoFinnigan Delta Plus mass spectrometer. The reported results are the difference between the samples given and the Vienna-CDT standard, in ‰ of $\delta^{34}S$.

Chapter 3

Field Relations

3.1 Main rock types

This section outlines the main rock types encountered within the study areas.

Anorthosite: The granulite anorthosite predominantly consists of a lilac and grey coloured plagioclase (Figure 3.1a). Common to the anorthosite are garnet-corona pyroxenes of both orthopyroxene (opx) and clinopyroxene (cpx). The coronas vary from spherical in shape to elongate eye-like structures. This original granulite plagioclase mineralogy is only present in small m^2 areas that have escaped later hydration and shearing. The granulites have also been statically retrogressed outward from small fractures that have introduced fluids, enabling the unstable granulite to hydrate to amphibolite conditions. This whitens the plagioclase in patterns following fractures, seen in Fig. 3.1a. Amphibolitisation is nearly complete along shear zones through which deformed rock has allowed fluids to pass.

The sheared amphibolite facies anorthosite also contains coronas, however, the garnet and plagioclase have been converted to amphibole; and the central pyroxene to chlorite and talc (Figure 3.4c). The amphibolitised plagioclase is a finer-grained, stark white colour (see Fig. 3.1b). Mukai et al. (2014) show the change in colour, from lilac-grey to white, in the plagioclase occurs along the fractures and is due to the breakdown of plagioclase to form an intergrowth of Na- and Ca-rich domains with clinozoisite needles.

Locally the anorthosite becomes more mafic and can be classified as gabbroic anorthosite or anorthositic gabbro according to mafic content percentage, as noted by Austrheim and Griffin (1985). These differences in composition, the alignment of lens-shaped coronas and some veins, create a granulite facies banding in the anorthosite complex.

There are numerous pyroxene-amphibole-scapolite (px-am-scp) veins within the anorthosite. These veins are from several centimetres to millimetres in width, both cross-cutting and following foliation in the rock (see Figs. 3.1b, 3.3b and 3.4b).

Jotunite: Another rock type seen in the study area is jotunite (Fig. 3.1c), which forms up to several metres-scale dykes, both following and crossing the main anorthosite foliation. It is plagioclase and orthopyroxene rich and is part of the charnockite suite of rocks, equivalent to an orthopyroxene-bearing monzodiorite. Here, it is an equigranular, sugar-textured orthopyroxene, plagioclase, ±garnet rock. It is rich in Fe-Ti oxides and frequently contains carbonate veining with quartz, Fe-Ti oxides, pyrite and acicular amphibole. Like the anorthosite, it has been locally amphibolitised to a largely amphibole-bearing rock.

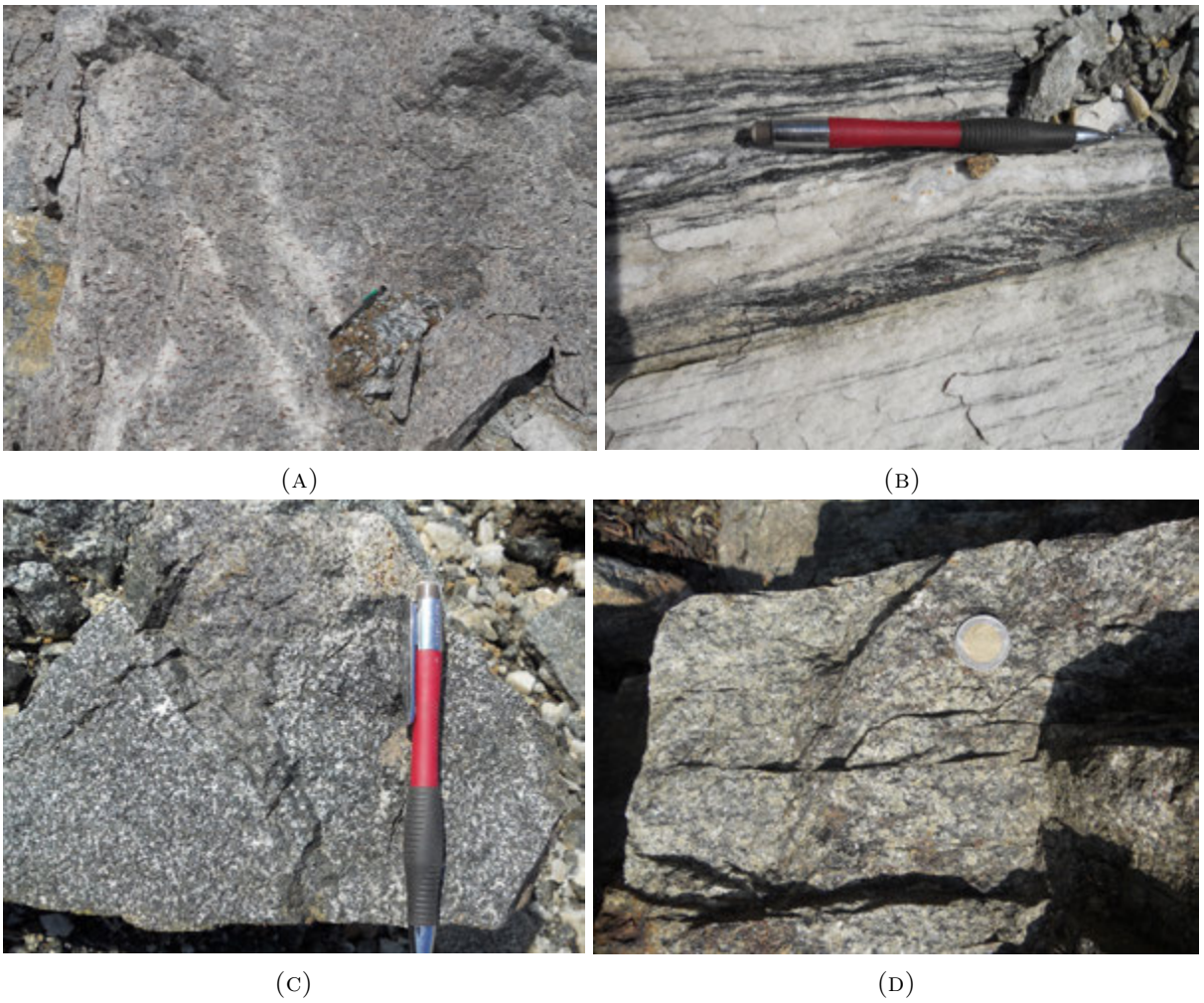

(A) (B)

(C) (D)

FIGURE 3.1: (A) Lilac-grey anorthosite with cm sized, highly elongate garnet coronas. Central white areas are hydrated white anorthosite following fractures. (B) Sheared white anorthosite with strong foliation, containing sulphide-bearing mafic bands. C) Hydrated jotunite vein cutting through Isdal anorthosite, also sample ISD13-04. D) Mangerite at the western contact of the anorthosite in the Hilland area, also sample HIL14-03.

Mangerite: This is a dark, opx, cpx, mesoperthite, apatite, and amphibole-rich rock (see Figure 3.1d), which can break down to form a biotite-rich rock. It contains a massive mesoperthitic, hyper-solvus feldspar, which may be the source of potassium observed in the granulites. The mangerite is found on the western side of Lindås and forms the western contact with the anorthosite in the Hilland area. This rock contains visible amounts of sulphides, both Fe, Cu and possibly Ni; and together with the Fe-Ti oxides, make up nearly 5 modal % of the rock. This sulphide phase could be remobilised under deformation or the presence of a fluid, to be either a source of metals or sulphides during mineralisation along faults.

Fe-Ti mafic rock: This is a plagioclase and pyroxene rich, equigranular, medium grained (1-2 mm), garnet bearing rock, containing a high percentage of Fe-Ti oxides, sulphides and apatite.

The rock is quite magnetic and is found on Holsnøy near to the Espetveit Mine site, as a contact rock with the faulted quartz breccia-rich anorthosite.

3.2 Structural Relationships

3.2.1 Isdal

Anorthosite is the predominant rock type at the Isdal study area, near the town of Isdalstø on Lindås (see Figure 3.2). The locations of all hand samples taken for this study are plotted on this figure. In addition to the anorthositic rocks, small dykes of jotunite are plotted, trending in a similar direction to the regional geology (Figure 1.1). This locality has excellent examples of coronitic granulite in contact with highly sheared anorthosite (Figure 3.3a). In under a centimetre of lateral distance, garnet coronas of the anorthosite are stretched into the shear zone, completely obliterating the original texture; and changing the mineralogy significantly to hydrated assemblages. These types of shear zones are common in the study area, varying in size and direction.

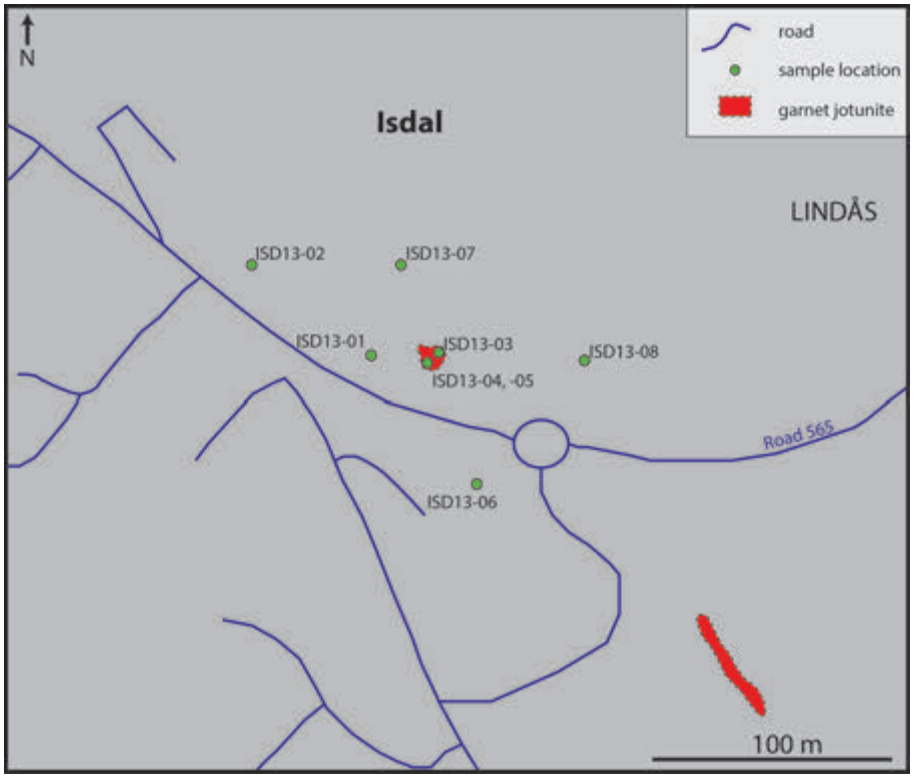

FIGURE 3.2: A location map of the Isdal area showing hand sample locations and related geological units. The grey colour and regional geology are as in Figure 1.1.

Also noted in the Isdal area are centimetre-size, dark grey veins containing scapolite, pyroxenes and sulphides. These veins cross the granulite to amphibolite facies boundaries. Samples ISD13-01A, ISD13-01B, ISD13-7A and ISD13-07B, were taken to identify the changes, if any, in mineralogy and texture as scapolite and sulphide minerals cross these metamorphic grade boundaries. These sulphide- and scapolite-bearing veins and coronas are continuous, and easily traced across the grade boundaries (see Figures 3.1b, 3.3b, 3.4a, and 3.4b). It becomes difficult to follow veins across the shears, as they become part of the intense foliation. The elongate linear features within the shear zones may have formed from these veins, stretched coronas or deformed mafic 'pods' of the original mineralogy (see Figure 3.4d).

(A) (B)

FIGURE 3.3: (A) The relationship of amphibole facies shearing (left) to the granulite garnet corona texture (right) of the anorthosite in the Isdal area. (B) Scapolite-pyroxene veins cut through a garnet granulite (top) and are pulled inside a shear zone (bottom). Note in both cases, plagioclase becomes white toward the shear zones and garnets are less frequent.

The scapolite veins splay in multiple directions, cross-cutting each other and the garnet-corona foliation. They are black to greenish in colour, depending on the degree of amphibolitisation, and are typically 1-2 cm wide. These veins occur with high frequency; for example, one area contains 1 cm wide veins, occurring less than 10 cm from each other, over a 20 metre section (Figure 3.4b).

Mafic 'pods' containing orthopyroxene and clinopyroxene are also observed with high sulphide content within the coronitic anorthosite gabbro (Fig. 3.4d). They are approximately 30 cm wide, containing up to 7 mm euhedral pyroxene grains, and are associated with Cu-Fe sulphides. Additionally, there are pseudotachylytes found locally in sheared walls of this mafic anorthosite.

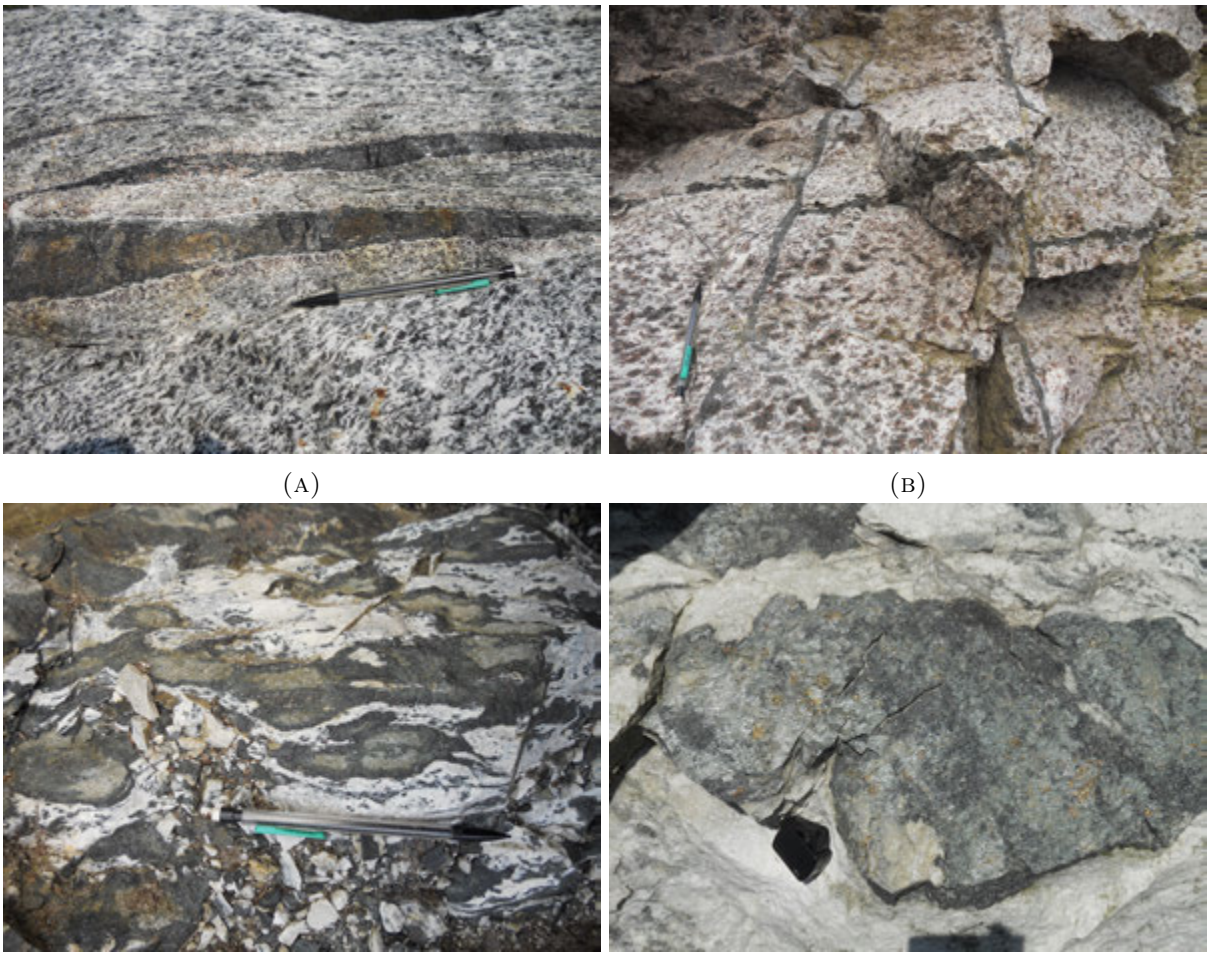

(A) (B)

(C) (D)

FIGURE 3.4: (A) Typical sheared, hydrated gabbroic anorthosite showing strong fabric defined by mafic bands and former corona(?) structures. Millimetre-sized garnets are concentrated around the mafic bands. Orange staining indicates presence of sulphides. (B) Representative coronitic garnet anorthosite with pyroxene-scapolite veining. Note there are several multi-directional veins in a 30 cm^2 area. (C) Hydrated corona features in white anorthosite. Note the garnet and pyroxene is completely gone, replaced with amphibole, chlorite and talc. (D) A mafic 'pod' in hydrated anorthosite containing Cu-sulphides.

Also associated with the veining and mafic pods is a 1.5-2 m wide jotunite dyke. It is difficult to determine if the veining is directly related to the main jotunite intrusions in the region. The jotunite has tension gashes filled with megacrysts of carbonate, quartz, acicular amphibole, oxides and sulphides. Samples ISD13-03, ISD13-04 and ISD13-05 were taken to assess the

mineralogy of this rock as a possible source of base metals in mineralisation, as well as for scapolite content and composition.

3.2.2 Hilland

Near the southeastern shore of Radøy, at the northern end of Hillandsvatnet, lies the old adit and tailings of the Hilland Mine (see Section 1.2.2). A location map of the Hilland area is given in Figure 3.5, showing locations of the samples collected, structural measurements and local geological units. A 10 m deep vertical mine shaft can still be found near old copper mine workings, marked as a black circle in Fig. 3.5. The Cu-mineralisation lies within anorthosite in close proximity to the regional fault, striking approximately 030°. The fault can be seen extending across Radfjorden, southwest to Holsnøy where the Espetveit Mine is located. It is part of a regional system of similarly oriented faults that may be associated with late regional extension (Fossen, 1998).

The waste rock pile of the former Hilland Mine sits approximately 10 m southwest of the main shaft. These are located in a depression, with topographic highs of anorthosite immediately to their northwest and east. Various sulphide-rich rocks were sampled from the slag pile, as the original ore body is no longer accessible. The waste rocks contain mostly quartz, with up to centimetre sized pyrite (py) grains, and chalcopyrite (cpy) with malachite staining (see page 23). Roses of acicular white amphibole are seen grown on fracture planes together with sulphides. Fractures show spaced quartz-filled brecciation.

3.2.2.1 Mine wallrocks

The wallrock immediately adjacent to the quartz breccia of the mineralised zone, is a hydrated garnet anorthosite. Garnets no longer appear in the localised shear zones closest to the fault. The anorthosite has been amphibolitised, although lenses of original granulite rocks remain within anastomosing, 20 cm to metre sized shears. The anorthosite of the wallrock is alternating between sheared and static hydration. Fractures in the static hydrated rock are associated with very white anorthosite.

The topographic highs north of the mine shaft are comprised of predominantly granulitic anorthosite. Across the tops of these highs, there are 1 to 30 cm wide garnet-bearing, pyroxene and scapolite rich mafic bands. Many of the mafic bands are running at similar strike

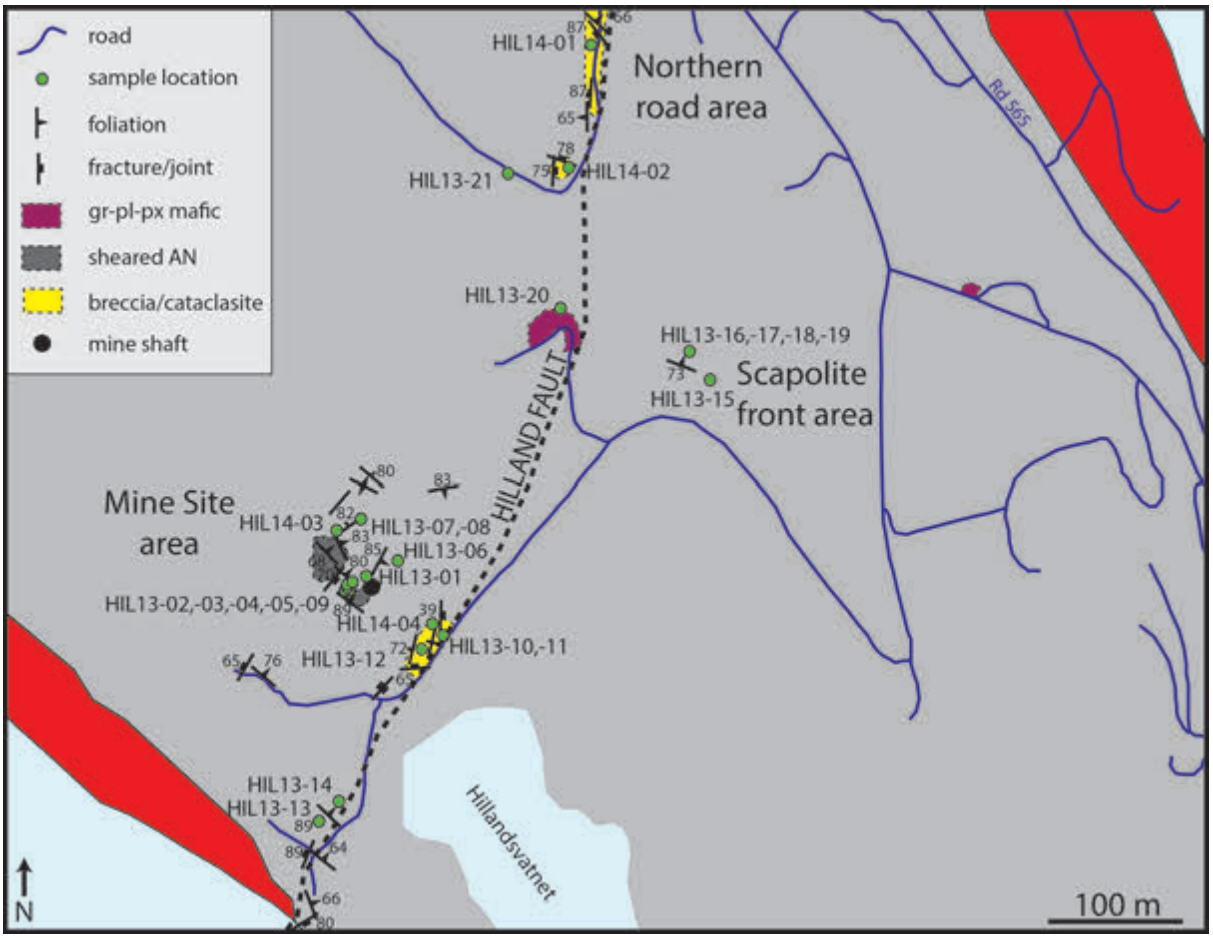

FIGURE 3.5: A location map of the Hilland area showing structural points, the main Hilland fault trace, hand sample locations and related geological units. The Hilland Mine location (black circle) is in a topographic low, assumed to be a fault splay, following the strike of the main fault. Red and grey colours and regional geology are as in Figure 1.1.

to the main Hilland Fault. Garnets in close proximity to the mafic bands are finer-grained when compared with the regular garnet-corona, granulitic anorthosite. Quartz veins are also prevalent here in 4-5 cm splays at a high angle to the main fault strike.

To the west of the shaft is more amphibolitic, hydrated anorthosite banding. Multiple, less than 1 m wide, hydrated shear zones are traced across the topographic high northwest of the mine shaft. They are approximately 10 m apart, of variable strike, and are separated by granulitic lenses. The different orientation of these shear zones is due to their anastomosing nature. This variably sheared area is indicated on Figure 3.5 in dark grey. Anorthosite foliation is vertical and similar to the fault direction.

Along the sharp rock wall in the Hilland Fault trace, fault breccia and veining, filled with 1 cm brown-stained carbonate and quartz, are found. The fragmentation and brecciation in the fault

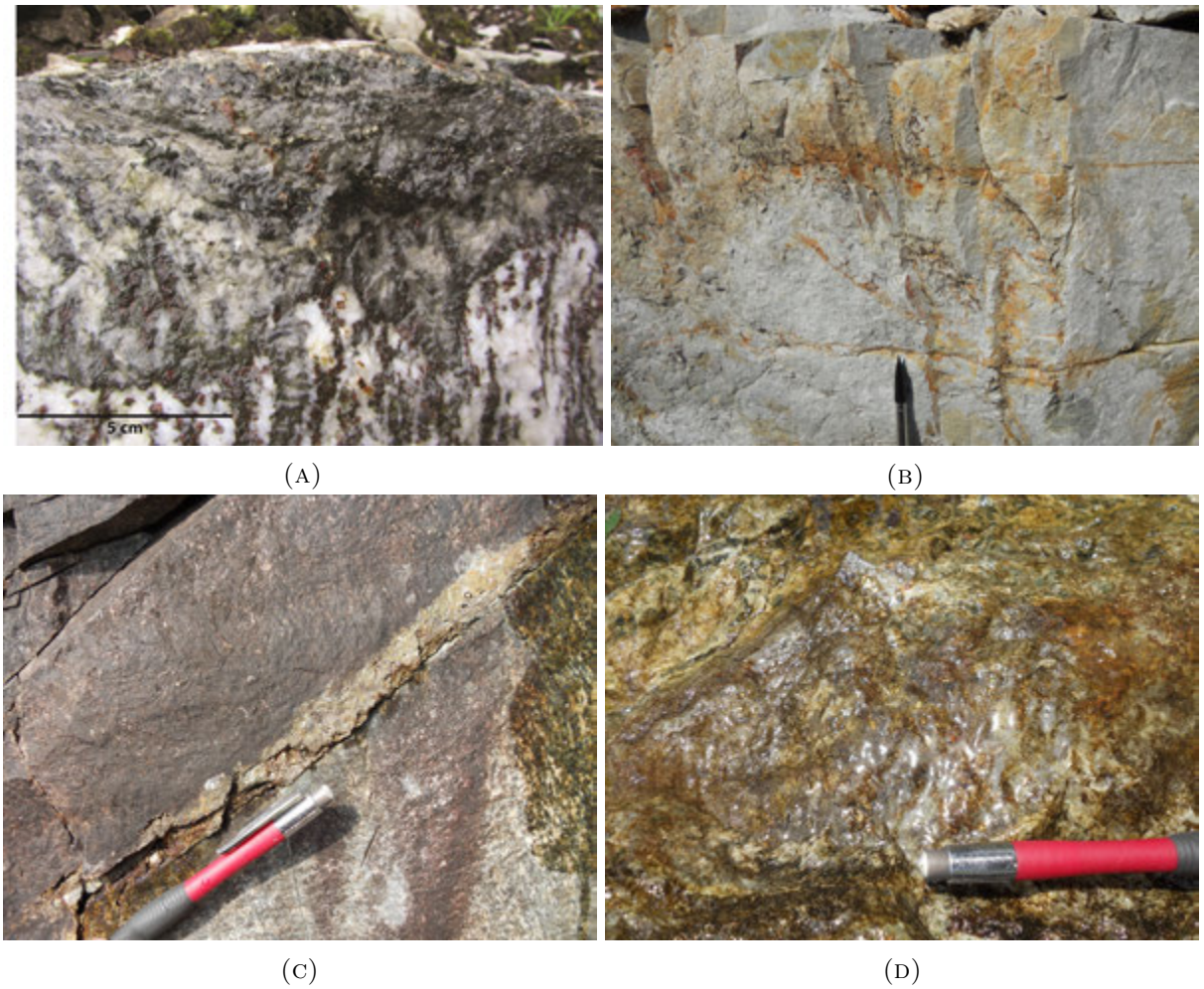

(A) (B)

(C) (D)

FIGURE 3.6: (A) Sample HIL13-15 scapolite 'front'. The top portion of the photo is scapolite with Fe and Cu sulphides (yellow flecks), the bottom portion is sheared garnet anorthosite. The two portions are separated by an abrupt and distinct front. (photo: H. Austrheim) (B) Breccia zone along the Hilland fault. The anorthosite is no longer foliated, and contains iron staining along fractures. (C) An example of Hilland fault zone mineralisation with Fe and Cu sulphides filling an approximate 1.5 cm wide zone along a fracture. (D) Cu sulphide mineralisation in quartz breccia associated with the Hilland mine fault.

zone follows the fault toward the ocean to the southwest. Sulphides, primarily pyrite and chalcopyrite, follow fractures, not the compositional layers (Figure 3.6c). Sulphides are associated with carbonate within these fractures. Also seen in the main fault zone is approximately 0.5 m wide breccia, associated with a nearly vertical sulphide deposition of py and cpy. The vertically plunging sulphide body may mimic the mined body at a smaller scale.

Towards the fjord, the foliation in the anorthosite thins, possibly because of stronger deformation. Garnets are present and are sheared in eclogite or amphibolite facies anorthosite. The rock at the west side of the island may have reached eclogite facies conditions and has since

been amphibolitised. Quartz-rich sulphide-bearing rocks are also found here, associated with the retrogressed eclogites.

Near the shore, where the trace of the fault meets the water, there is a lithology change to mangerite. This is a possible source of base metals found within the sulphides.

3.2.2.2 Scapolite 'front' rocks

Approximately 70 m southeast of the main fault is a lilac-purple, garnet-bearing 'original' anorthosite at granulite facies conditions. A light blue-grey coloured rock is found here intruding into the anorthosite. It is predominantly scapolite, formed through metasomatic processes, replacing plagioclase along a 'front'. The anorthosite in contact with this scapolite is a non-sheared, garnet bearing granulite. Sulphides, including py and cpy, occur in the scapolite as disseminated grains to 1.5 cm aggregates, within 3 cm of the front. No sulphides occur within the plagioclase. Two samples were taken, one where the front crosses a sheared anorthosite, HIL13-15 (Figure 3.6a), and the other where the front crosses a more pristine anorthosite, HIL13-18 (Figure 4.3a). The two samples are investigated further in the Petrography Section as the scapolite 'front' rocks.

In addition to the metasomatic 'front' rocks, there are two types of dark veins crossing the anorthosite in this area. One is a pyroxene-bearing, centimetre scale, dark grey vein. These veins cross-cut hydrated anorthosite foliation and contain cpy and py sulphide mineralisation. The second vein-type is a slightly lighter grey colour and also contains sulphides, primarily py, with minor cpy. These veins also follow foliation and cross shear boundaries, becoming greenish-grey and increasing in porosity in amphibolitised, white plagioclase zones. Both veins contain scapolite, and the lighter grey veins have a higher scapolite content.

3.2.2.3 Northern road

There are fault planes with gouge clay fill, up to 50 cm wide, in altered anorthosite breccia along the Hilland Fault trend, approximately 300 m north-northeast of the mine site. This is indicated in yellow on Figure 3.5. It is in contact with a 10 m wide, white-bleached, sheared anorthosite, with sulphides that have stained the rock reddish in colour. There is also an ultra(?)-cataclasite (Figure 3.6b) containing yellow, crystal-less lenses that are brecciated and intermixed with normal sheared, white anorthosite. The cataclastic plane is vertically dipping,

at 356°. The bleached white fault rock is continuous along the fault strike. It has a dissolved appearance in the feldspar, but amphibole and mica remain. The normal foliated anorthosite continues again approximately one metre away from the gouge.

Away from the fault, carbonate forms on fractures in the hydrated sections of the anorthosite. Fracture fill includes staurolite, calcite and muscovite; and chlorite and quartz grow on extensional fractures. Chalcopyrite is common within the mafic portions of the strained, hydrated anorthosite.

At the far western extent of the new road (Figure 2.1), a contact with the anorthosite is seen with a garnet-bearing, near-mesoperthitic feldspar mangerite-type rock. The contact between the mangerite and the anorthosite is gradual, with inter-fingering occurring over 20 m. The anorthosite at the contact is more mafic, approximating an anorthositic gabbro, and is nearly completely hydrated. Although variable, the mangerite follows the anorthosite foliation and banding, and steepens into shear zones. Mafic veins within the anorthosite contain up to 3 mm sulphide blebs.

3.2.3 Espetveit

Following the Hilland Fault direction from the Hilland Mine southeast onto Holsnøy, the former Cu-mine, Espetveit (Figure 3.7) is found near the waterfront. The main rock type is anorthosite, with mafic Fe-Ti rich rocks in close proximity to the Cu-mineralisation. This mineralisation is hosted within is a sulphide-rich, quartz-rich breccia, relating to, and following the fault. The wallrock farther away from the shore is a sheared anorthosite containing dehydrated garnet and boudinaged mafic bands, within which coarse-grained pyrite cubes are hosted. The wallrocks contain disseminated pyrite in light grey to pink feldspar. Closer to the eastern shore of Holsnøy, the pink feldspar is absent in the wallrock, and quartz is the main host to the sulphides.

The main fault structure can easily be followed a few hundred metres to the southwest along a large road cut. Fault breccia is observed over a 20 m crushed rock section, as a bleached white anorthosite, without typical foliation. No sulphides are observed farther than few tens of metres southwest of the main Espetveit shaft.

There are three adits still visible at surface in the Espetveit area (see Figure 3.7). Two are vertical and filled with water, and the third is horizontal and inaccessible. Tailings can still be

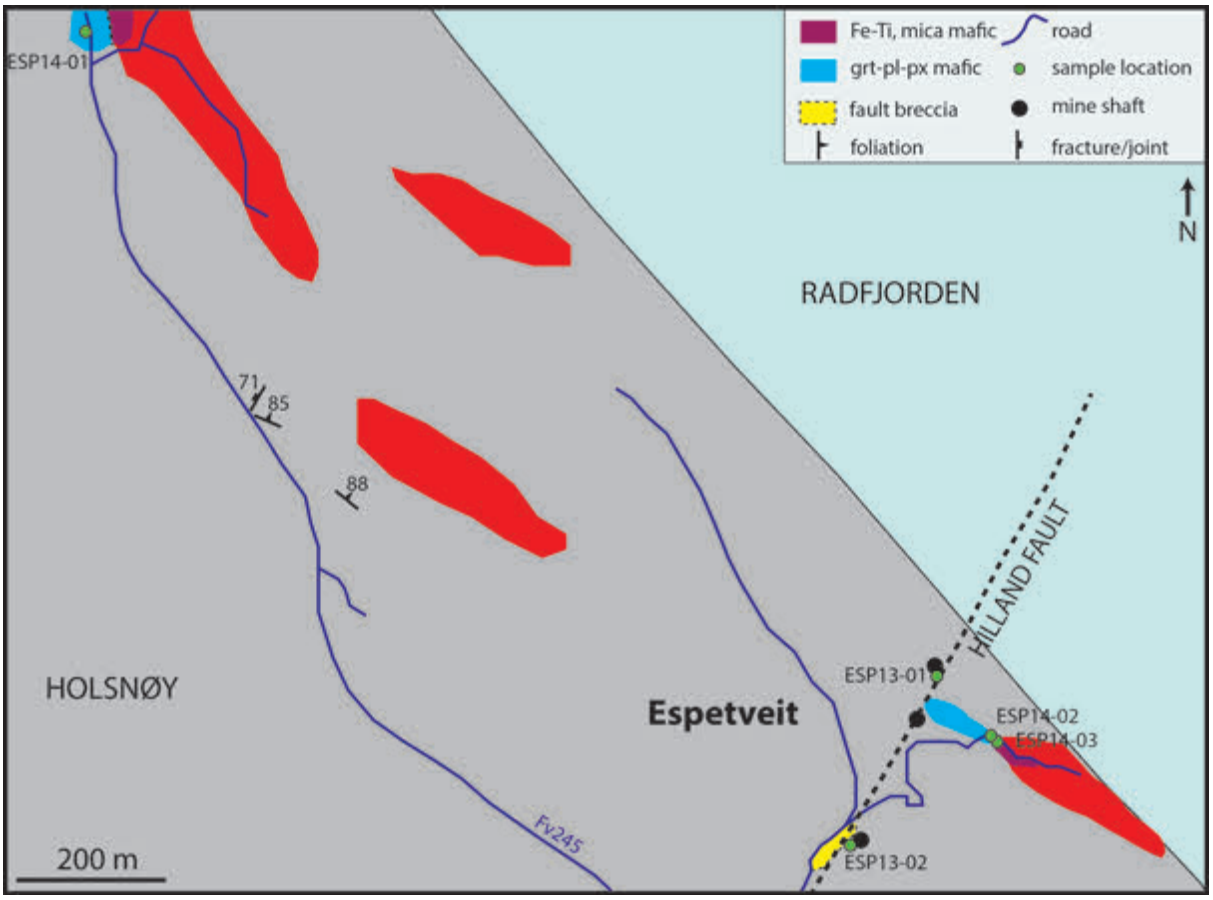

FIGURE 3.7: A location map of the Espetveit area showing structural points, the Hilland fault trace, hand sample locations and related geological units. Red and grey colours and regional geology are as in Figure 1.1.

found at the upper vertical shaft. Open cavity fill of quartz and a yellow epidote exists in the tailings.

Mafic rocks are found approximately 50 m east of the adit entrance. These are high in Fe-Ti oxides, garnet, plagioclase and pyroxene; and occur as a dyke, separating the anorthosite of the mine site area from the Fe-Ti oxide and coarse mica-rich rock to the east and south. These mafics may constitute a lens forming within the anorthosite. They also may be a source of the base metals found in the mine.

North of the mine site, the anorthosite becomes more mafic, occurring with garnet-bearing pyroxene rich pods containing variable amounts of sulphides. Plagioclase is white, highly sheared, with near vertical foliation. Certain localities appear eclogitised with variably sheared, hydrated anorthosite zones with mafic banding.

The northern contact with the anorthosite is shown in Figure 3.7. In this figure, the upper contact is outlined in blue, purple and red. The unit mapped in red is from the original regional mapping shown in Figure 1.1. The western, blue-mapped rock is massive, equigranular plagioclase and pyroxene rich, with epidote staining on planes.

The purple-mapped rock, to the east of this contact, is a rock type similar to what is seen in the eclogitised northern portion of Holsnøy. It is a Fe-Ti rich, white coloured, mafic rock containing garnet and coarse-grained mica. It is magnetite- and ilmenite-rich, and is similar in composition to the rock at the eastern contact of the Espetveit Mine site.

Chapter 4

Results and Analyses

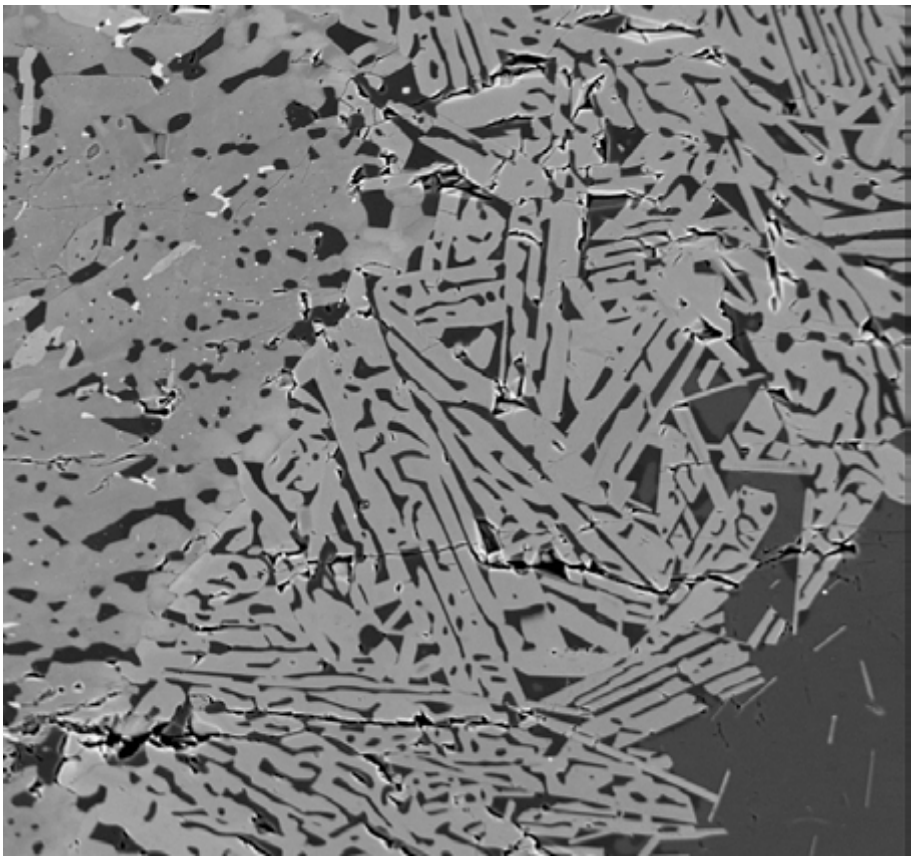

4.1 Petrography

Thirty new thin sections were created from the collected hand samples during the two field seasons. A list of thin sections made, their localities and general description are provided in Table A.1, of the Appendix. Additional thin sections, including ESP-5-13 from the Espetveit Mine area, and 44-91A and AK72-98II from Isdal were provided by Håkon Austrheim. The prefixes of the thin sections indicate the locality of origin, ie: ISD samples were collected at Isdal, HIL from Hilland and ESP from Espetveit.

The Petrography Section introduces first the granulitic anorthosite mineralogy, including the occurrence of scapolite. The scapolite has three main modes of formation within the rocks at granulite facies:
1) as small, intergranular, subhedral grains within the main coarser-grained plagioclase and garnet groundmass
2) within veins, generally with pyroxene, but also alone
3) as the primary rock forming mineral, in distinct and continuous contact with anorthosite in what looks like a metasomatic reaction front.

Scapolite compositional changes are described as they retrogress from granulite to amphibolite facies conditions. The scapolite of lower sulphate content is described in amphibolite faces mineralogy. The change in habit, mode and composition of scapolite, and any associated sulphides, are compared as scapolite grains break down under both static and shearing conditions.

4.1.1 Granulites and S-scapolite

As outlined in previous sections, the granulite facies rocks of the Lindås Nappe are extensively retrograded to amphibolite facies assemblages. Mukai et al. (2014) estimates only 10-15% of the granulite is preserved, and even in these areas, initial stages of hydration are found. The typical mineralogy of a granulite anorthosite consists predominantly of medium-grained andesine-labradorite plagioclase with garnet and pyroxenes, cpx and opx. In many cases, the plagioclase is anti-perthitic, containing small exsolutions of Kspr grains. Garnets vary from forming large mm- to cm-scale ovoid coronas around coarse-grained pyroxene clusters to single grains of pyroxene. At other localities, garnets are found as separate grains in the plagioclase matrix, with no association to pyroxene. Accessory minerals include S-scapolite and oxides of

intergrown ilmenite and hematite. The scapolite in the scp-px veins, described first in Section 3.2.1, can consist of 20-50 modal percent of the veins, or approximately 1% of the whole rock.

The anorthosite complex grades from pure anorthosite to gabbroic anorthosite. Scapolite is present in all parts of the anorthosite complex. It increases in amount from anorthosite to gabbro, where it may account for up to 5 modal %, occurring together with plagioclase, orthopyroxene, clinopyroxene and hornblende. Jotunites contain garnet, pyroxenes, Fe-Ti oxides, apatite and an anti-perthitic plagioclase. The jotunite contains high S-scapolite.

HIL13-19 was chosen as a representative sample of a relatively unaltered granulite, having the most 'original' looking mineralogy. The plagioclase is a lilac-grey labradorite, medium- to coarse-grained, with ovoid, cm-long garnet coronas of clinopyroxenes (see Figure 4.1). The scapolite in sample HIL13-19 ranges from 3.8-3.9 wt.% SO_3. This high sulphur content is consistent with scapolite found within granulites elsewhere in the world, where they are found to contain from 2.2 to 6.4 wt.% SO_3 (Deer et al., 2006; Hoefs et al., 1981).

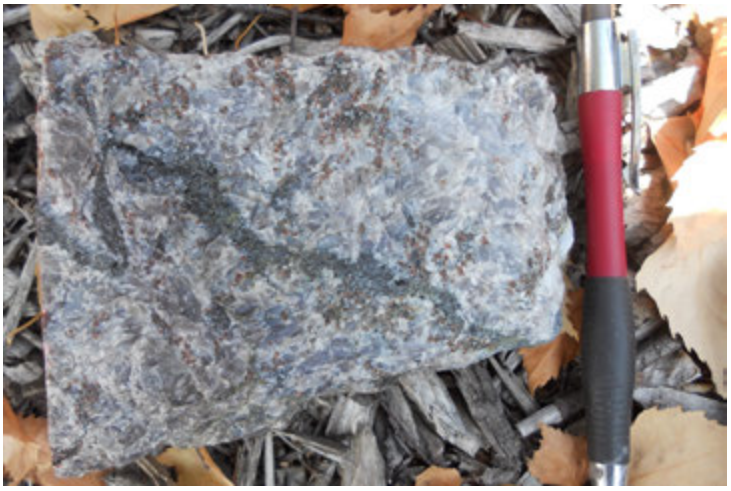

FIGURE 4.1: Hand sample HIL13-19, collected as the most original granulite rock in the field study area. It is a coarse-grained anorthosite with lilac-grey plagioclase, garnet coronas surrounding pyroxene, and is cut by a pyroxene-scapolite vein.

In the plane-polarised micrographs of thin section HIL13-19 (Figs. 4.2a and 4.2b), the dominance of the plagioclase, consisting of approximately 85-90% of the rock, is evident. As this sample has been partially retrograded, plagioclase contains multiple inclusions of thin epidote and clinozoisite needles. In typical more 'original' granulites, these are not present. Scapolite grains are comparatively smaller than plagioclase and garnets, at about 0.5 mm or less in width, and make up approximately 5% of the whole rock. Grain boundary angles of the scapolite are 120°. In plane-polarised light, the scapolite grain boundaries appear dark, which is, in part

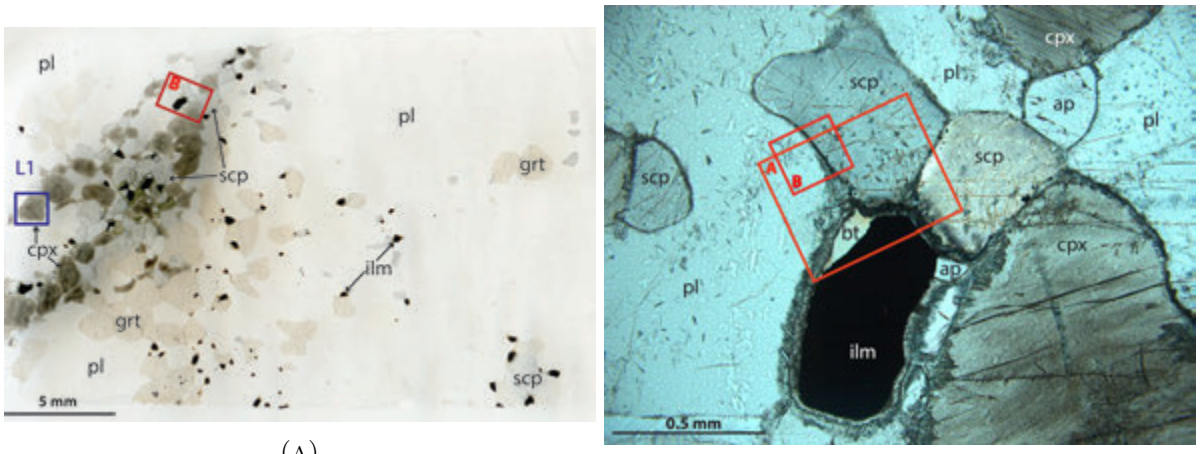

(A) (B)

FIGURE 4.2: (A) Thin section of HIL13-19, a granulite facies anorthosite. It is predominantly transparent plagioclase with a scp-px vein crossing down the upper-left side of the photo. Pink garnet coronas are present with brown-green cpx. Scapolite (grey) is also present within the pl. The opaques are oxides, ilmenite with hematite exsolution, and biotite reaction rims. The red box delimits the boundaries of (B). The blue box indicates the cpx grain surveyed as Line 1 (L1) for Ni and Cu concentrations (see Section 4.2.5.1). (B) A micrograph (ppl) of the relationship between scp, pl and ilm. Reaction rims exist around ilm, scp and cpx. Pl contains inclusions of epidote laths. Apatite is also present in the scp-px vein. The red boxes indicate the areas of study in Figures 4.5a and 4.5b.

caused by the presence of dense, fine-grained sulphides (see Fig. 4.5b). Other accessory minerals are opaques (intergrown ilmenite and hematite), biotite and apatite. Other examples of the more granulitic rocks within this study are the wallrocks of AK72-98II, ISD13-07A and the metasomatic scapolite 'front' rock, HIL13-18.

4.1.1.1 S-scapolite in metasomatic veins

In sample HIL13-18, S-scapolite is the primary rock-forming mineral which forms an abrupt and distinct 'front' with a granulite facies anorthosite (see Figs. 4.3a and 4.3b). Once the scapolite 'front' is crossed, the plagioclase of the anorthosite is completely converted to scapolite. The anorthosite is andesine, An_{45}, the typical composition of plagioclase in this area. The garnets do not form coronas in this rock, but individual crystals. The garnets, which are quite abundant (5-10 modal %) in the anorthosite, are absent within the scapolitised section (Figure 4.3b). Conversely, pyroxenes are not abundant within the anorthosite; however, are relatively abundant in the scapolite portion of the rock.

The scapolite of HIL13-18 is of silvialite composition. It has dark, equigranular, blue-grey crystals and Me contents between 65 and 66. The sulphur content is between 0.57 - 0.64 apfu in

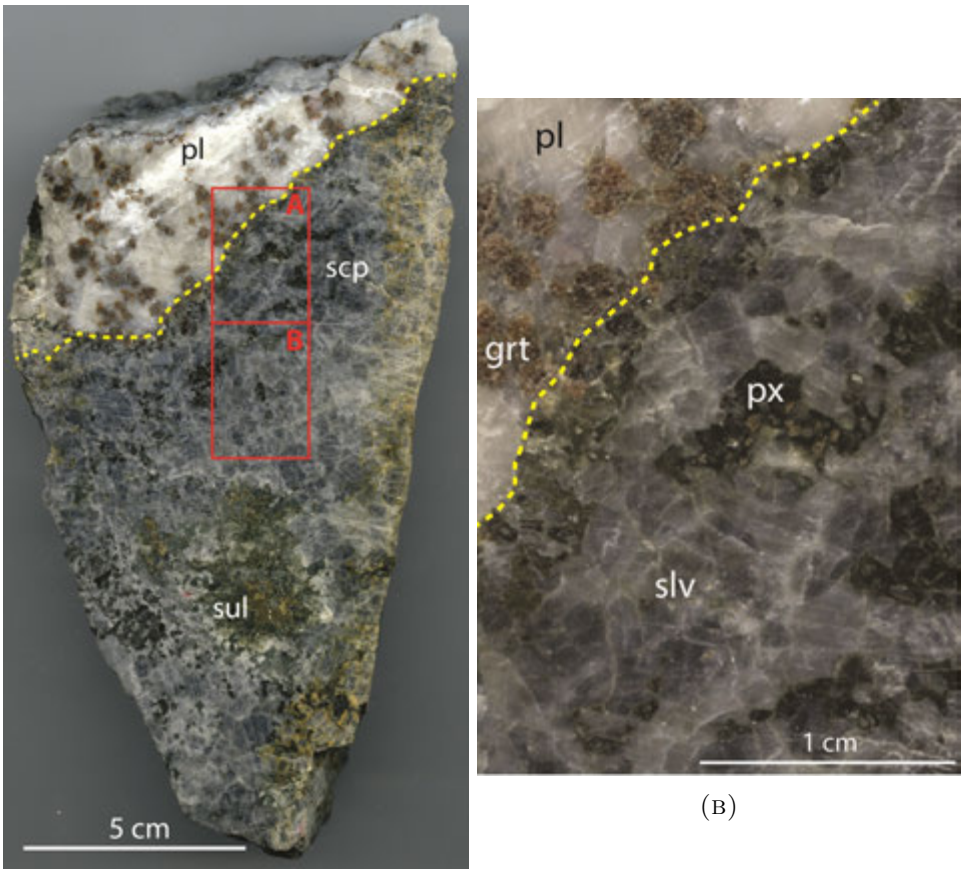

(A) (B)

FIGURE 4.3: (A) Hand sample HIL13-18 showing a sharp scp-anorthosite boundary, indicated with a dashed yellow line. The red boxes delimit the areas of the two thin sections prepared for study, HIL13-18A and-B. Box 'A' is the area shown in (B). (B) A section from HIL13-18 showing a close up of non-hydrated blue-grey silvialite crystals in contact with anorthosite. Compare with the meionite of (A). Also note the difference in the anorthosite between the sheared and non-sheared samples.

the anion site, from analysis done on thin section HIL13-18B. This corresponds to SO_3 contents between 4.89 and 5.44 wt.%. However, analyses closer to the contact with the anorthosite reveal the SO_3 content decreases, and CO_3 increases, nearly systematically to meionite compositions of 0.41 apfu S at the 'front'. An influx of carbon-bearing fluid along this front may represent the early stages of hydration.

As scapolite is replacing the anorthosite mineralogy, a reaction can be written:

$$pl + SO_2 + CO_2 \longrightarrow (S)scp \tag{4.1}$$

Also present within the scapolite is pyroxene, amphibole and epidote. Sulphides occur as large,

up to 1 cm sized blebs of pyrite and chalcopyrite that are closely associated with former pyroxenes. Pyroxenes exist close to the anorthosite, but become more hydrated away from the 'front'. They become pseudomorphs, completely replaced with amphibole, epidote and chlorite, with only the old shape and exsolution lamellae remaining. The pyroxenes near the anorthosite boundary are of similar content to the granulite rock, HIL13-19, with a higher TiO_2 content, averaging 1.68 wt.%. One of pyroxenes from HIL13-18A was selected for trace element Ni and Cu content evaluation (see Section 4.2.5.1).

The samples collected for this survey have many characteristics of the granulite facies anorthosite mineralogy; however, most were amphibolitised and many have an intermediate mineralogy of partially broken down granulite minerals. Many pyroxenes are retrograded to the point they have been completely transformed to amphibole and epidote. Plagioclase becomes finer-grained and of higher sodium content. Furthermore, ilmenite breaks down to rutile and titanite; and scapolite breaks down varyingly to epidote, amphiboles and sulphides. The following section describes the granulite to amphibolite transition in greater detail.

4.1.2 Granulite to amphibolite facies reactions

Amphibolite mineralogy of the anorthosites, in most of the samples of the study area, consists of predominantly andesine plagioclase, which contains increasing amounts of clinozoisite and epidote needle-inclusions with retrogression. In veins and more mafic bodies, mineralogy includes green-brown amphibole with fine-grained anhedral quartz association, biotite with minor amounts of chlorite, rutile ± titanite, a second type of garnet (grt2) and sulphides. General granulite to amphibolite reactions in the anorthosite that can be inferred based on observations include:

$$(Ca)pl + H_2O \longrightarrow (Na)pl + czo \tag{4.2}$$

$$pl + Kspr + grt1 + H_2O \longrightarrow bt + am + ep \tag{4.3}$$

$$cpx + H_2O \longrightarrow am + qtz \tag{4.4}$$

$$(S)scp + H_2O \longrightarrow ep + pl + sul + CO_2 \tag{4.5}$$

More specific reactions involving the breakdown of granulite to amphibolite facies mineralogy, specifically scapolite, opx and Fe-Ti oxides are presented in later sections with relevant samples.

Figures 4.4a and 4.4b show scapolite samples from the thin section 44-91-A. The first BSE image shows a scapolite grain in an anorthosite similar to the granulite of HIL13-19. It has a high sulphur content, 7.21 wt.% SO_3, the highest found in the survey area and within the literature regarding silvialite SO_3 compositions. A few rounded sulphide blebs are formed on the edges of the scapolite.

The second image (Figure 4.4b) shows an area of similar shape and size, without any scapolite present. It is postulated that this once was a scapolite grain that has been completely replaced by epidote, plagioclase, K-feldspar and sulphides; both pyrite and chalcopyrite. Also of note is the up to 15 μm sized, irregular shaped pore space, and the two fractures passing from the lower left corner to the top right. These may have played a role in, or resulted from the introduction of fluids, leading to the change in mineralogy. The similarities in shape, size and occurrence of the former mineral in this figure and the scapolite in Figure 4.4a, is evidence of scapolite degradation to sulphides during hydration. The sulphides seen around the edges of the first scapolite indicate the beginning of the breakdown of scapolite to sulphides, plus epidote and plagioclase. The area outlined in red in Figure 4.4b is the resultant mineralogy, after complete breakdown of a high sulphur-scapolite. Comparing the two images from thin section 44-91A, a reaction can be written describing the breakdown of scapolite:

$$(S)scp + Fe + H_2O \longrightarrow ep + pl + sul + CO_2 \tag{4.6}$$

Further examples of scapolite breakdown are provided below and in later sections.

Figure 4.4c shows a BSE image of retrograded mineralogy of zoned, euhedral laths of epidote, biotite with chlorite, Na-rich plagioclase and scapolite. Many tiny sulphide blebs are found predominantly within epidote, clearly enough that epidote can be distinguished from biotite, solely from the presence of sulphides in epidote, and absence in biotite. Irregular shaped scapolite grains are found within the epidote. This scapolite is a silvialite with 5.43 wt.% SO_3. It has become unstable and partially replaced by epidote and biotite. However, epidote, an oxidised mineral containing only ferric iron, is the only mineral here that incorporates the sulphur from scapolite as sulphide inclusions.

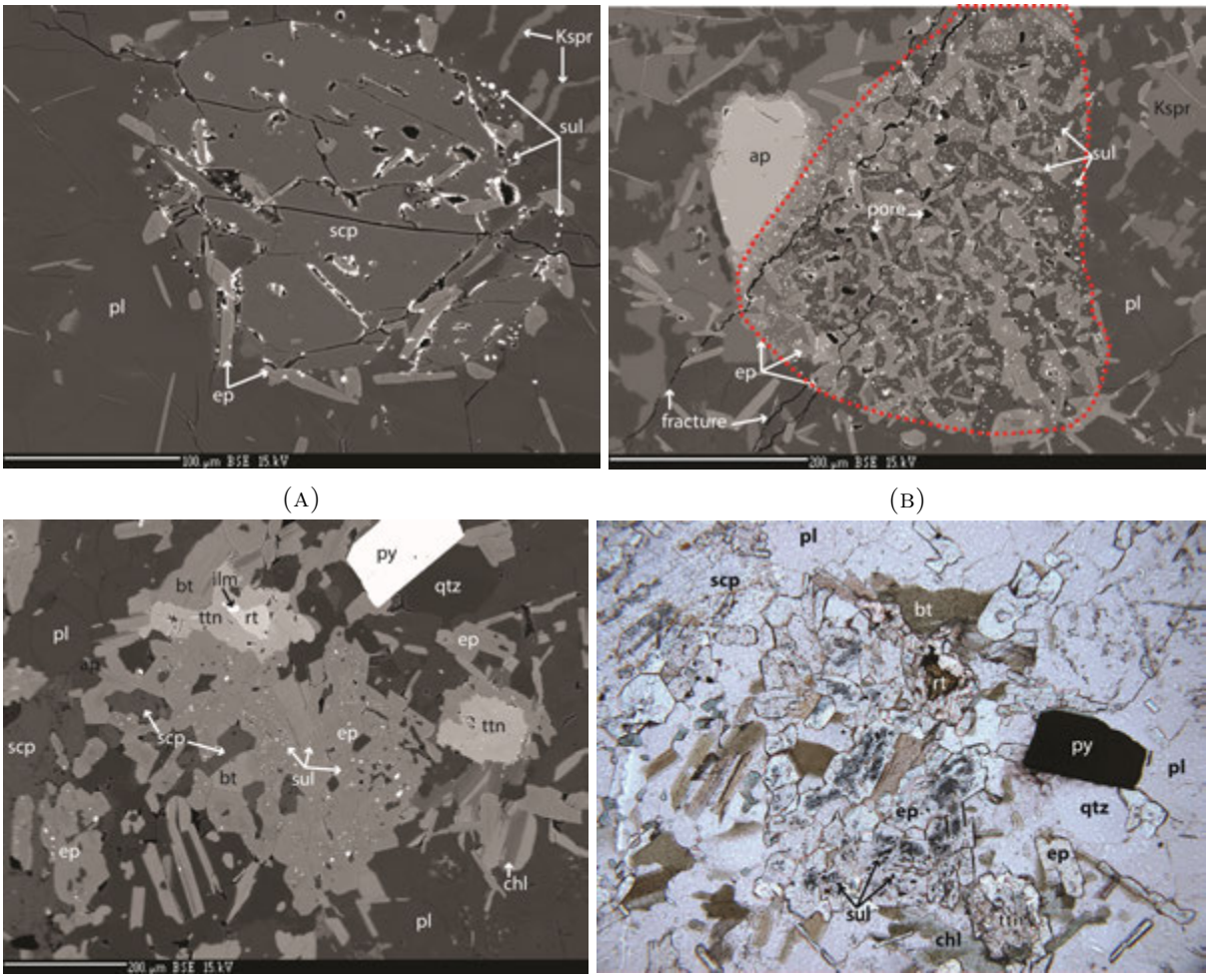

FIGURE 4.4: (A) A BSE image a scapolite grain in thin section 44-91A. Note its vague triangular shape and the sulphide blebs forming along its outer grain boundary. Other bright spots, following grain boundaries and fractures within the grain, are a result of tin particles applied for polishing. (B) A BSE image from 44-91A, showing a triangular shaped area delimited by the occurrence of sulphides and highlighted with a red dashed line. Within the area are also epidote, plagioclase and Kspr. Note the occurrence of pore space and fractures running from the bottom-left to top-right. (C) A BSE image of sample ESP-13-5, found near the Espetveit Mine site, showing epidote laths containing sulphides (py and cpy). High S-scapolite, biotite, titanite, rutile and ilmenite are also present. Note the sulphides only form within the epidote, not the biotite. (D) Ppl image of the area in (C). Note the dark, cloudy appearance as a result of sulphides within the epidote laths.

Figure 4.4d shows the same area as Figure 4.4c, but in plane-polarised light. Of note here is how the sulphide blebs form a dark, shadowy area within the epidote. This dark shadow is seen in many samples, along the edges and grain boundaries of scapolite. Also of note in these two figures is the presence of ilmenite, titanite and rutile. The ilmenite is predominant in the granulite mineralogy, but here is quite fine-grained and associated with rutile and titanite. This suggests it has lost its Fe content during the amphibolitisation process, but the Ti remains in place as rutile. This ilmenite-rutile breakdown association has been noted before by Austrheim et al. (2008), Morisset and Scoates (2008), and Engvik et al. (2011). This Fe released from ilmenite can be used to form sulphides with sulphur from S-scapolite.

4.1.3 Replacement of scapolite during static regression of granulites

In the granulite sample, HIL13-19, initial retrogression is evident along the edges of garnet, scapolite and the oxides. These reaction rims are forming without dramatic change in the shape or textures of surrounding minerals or overall rock appearance. This sample, and others presented below, form the bases for reactions that occur in static conditions. This is in contrast to reactions occurring during deformation, such as shearing, which are introduced in Section 4.1.4.

In HIL13-19, the edges of garnet and pyroxene have broken down to produce amphibole and epidote. Biotite, garnet2 (grt2) and epidote have formed around ilmenite (see Fig. 4.5a). The composition of grt2, formed as a reaction on the rim of the ilmenite grain, differs from those in the original anorthosite; with increased Fe and Ca contents, but lower Mg content. Also in this figure, a scapolite-plagioclase boundary is shown. Along the edges of the scapolite and within the epidote and garnet, many small sulphide blebs can be seen of varying sizes. Fe-rich sulphides form blebs up to 12 μm in size, though most are less than a micron, and cannot be discerned in the photo. Note the sulphides only form in epidote and garnet where they are next to the scapolite; none form on the plagioclase side of the photo. Consequently, the presence of scapolite is assumed to be necessary for the formation of sulphides.

Figure 4.5b shows the scapolite-plagioclase boundary in detail. Here, the plagioclase content is labradorite (An_{52}) and the scapolite is meionitic, with Me_{71} and SO_3 of 3.7 wt.%. The boundary is not sharp, but is a 25 μm sized zone containing epidote, a high density of very fine grained sulphide blebs and a mineral that may be high Ca-plagioclase, though it contains an unusually

high amount of potassium (1.62 wt.% K_2O). Of note is the highly porous nature of this mineral; the pores forming interconnected zones nearly orthogonal to the grain boundary.

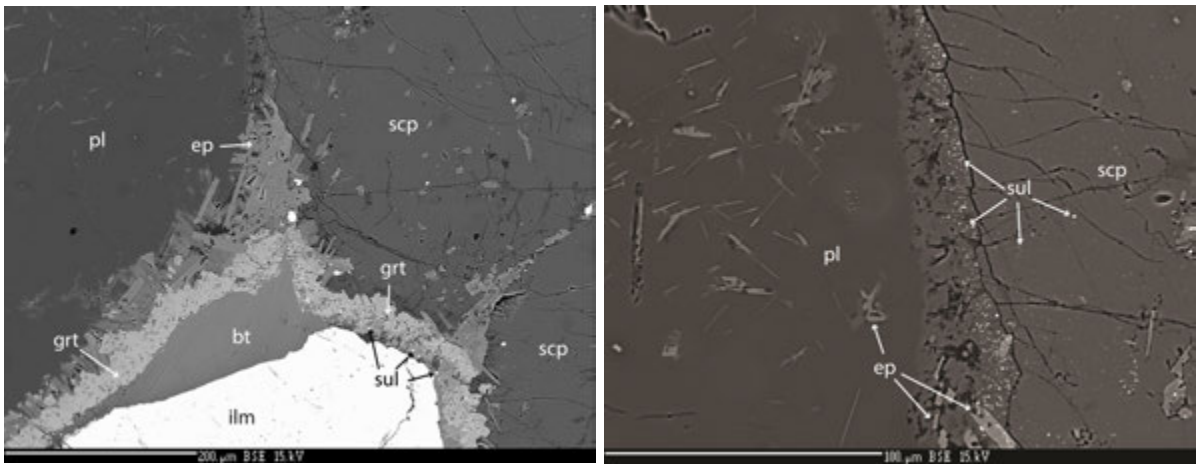

(A) (B)

FIGURE 4.5: (A) A BSE image of the reaction rim of ilm in the granulite rock, HIL13-19. Bt forms the inner boundary, followed by grt and ep. Within the grt and ep reaction rims, on the scp side of the ilm, are many sulphides, varying from less than one to up to 12 μm. Note their absence on the pl side. For location in thin section, see Figures 4.2a and 4.2b. (B) BSE image of the pl-scp boundary. Czo and ep laths are abundant within pl. Sulphides (sul) are abundant within the scp (<1 μm) and immediately outside the scp grain boundary (<5 μm). The mineral separating the pl and scp is a highly porous high-Ca plagioclase.

Another example of static retrogression within a locally sheared rock, HIL13-15 provides excellent examples of scapolite breakdown to sulphides. The scapolite of HIL13-15 (Figure 4.6b) is light grey, coarse-grained, with crystals up to 1 cm wide, and is of meionitic composition. The scapolite is between Me_{62-68}, with a S content between 0.17 and 0.46 apfu, corresponding to 1.48 to 4.01 wt.% SO_3. The Cl content is also low, less than 0.2 wt.% Cl, thus CO_3 is assumed to be the dominant anionic species. Multiple localised shears are seen crossing the meionite at a high angle to the anorthosite contact. Within the scapolite zone, amphibole, epidote and pyroxene are also identified.

A scapolite grain, in the scapolite front of HIL13-15, was studied with the EMP, producing a BSE image and element-mapped images of sulphur, calcium and iron (see Figs. 4.7a through 4.7d). The area studied is represented by Box 'A' in Figure 4.6b. This scapolite is outside the sheared zones, and is in bounded by large cpx and garnet grains. A reaction zone of amphibole and epidote has formed between the cpx and scp, as well as between the grt and scp. The grain boundary between scapolite and these minerals is irregular and ep laths are protruding into the scp crystal. The scapolite is meionitic, with Me_{68} and 3.92 wt.% SO_3.

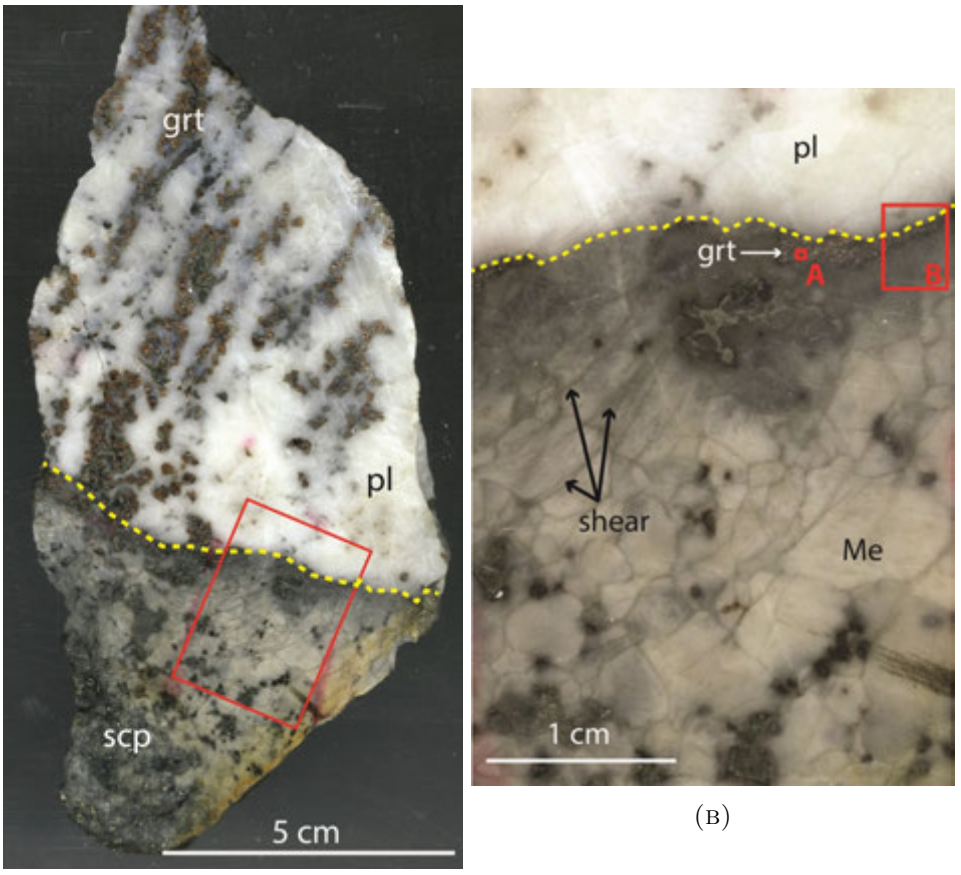

(A) (B)

FIGURE 4.6: (A) Hand sample of HIL13-15, indicating the scapolite-anorthosite boundary with a dashed yellow line. The red box delimits the area of (B). (B) Section of HIL13-15, indicating the meionite boundary with anorthosite (yellow dashes). Shears running to the bottom left at a 60°angle to the 'front', can also be seen. The dark minerals are pyroxenes with amphibole alteration. Box A is the area shown in Figures 4.7a, 4.7b, 4.7c, and 4.7d. Box B outlines the area of Figure 4.12a.

As seen on the BSE image (Fig. 4.7a), the area within the epidote zone, bordering the scp, has multiple inclusions of bright white blebs. When compared with the sulphur-mapped image (Fig. 4.7b), the white blebs correspond to high sulphur concentrations, which represent sulphides. The cluster of sulphur blebs form a smooth, continuous boundary, cutting through both am and ep growth. This well defined boundary may represent the original scapolite crystal, prior to being replaced by epidote, amphibole and sulphides.

Examples of reactions from the statically retrogressed portions of HIL13-15A are:

$$(S)scp + H_2O + Fe + Ca \longrightarrow ep + sul + Si + Na + CO_2 \tag{4.7}$$

$$(S)scp + H_2O + Fe + Mg \longrightarrow am4 + ep + sul + CO_2 \tag{4.8}$$

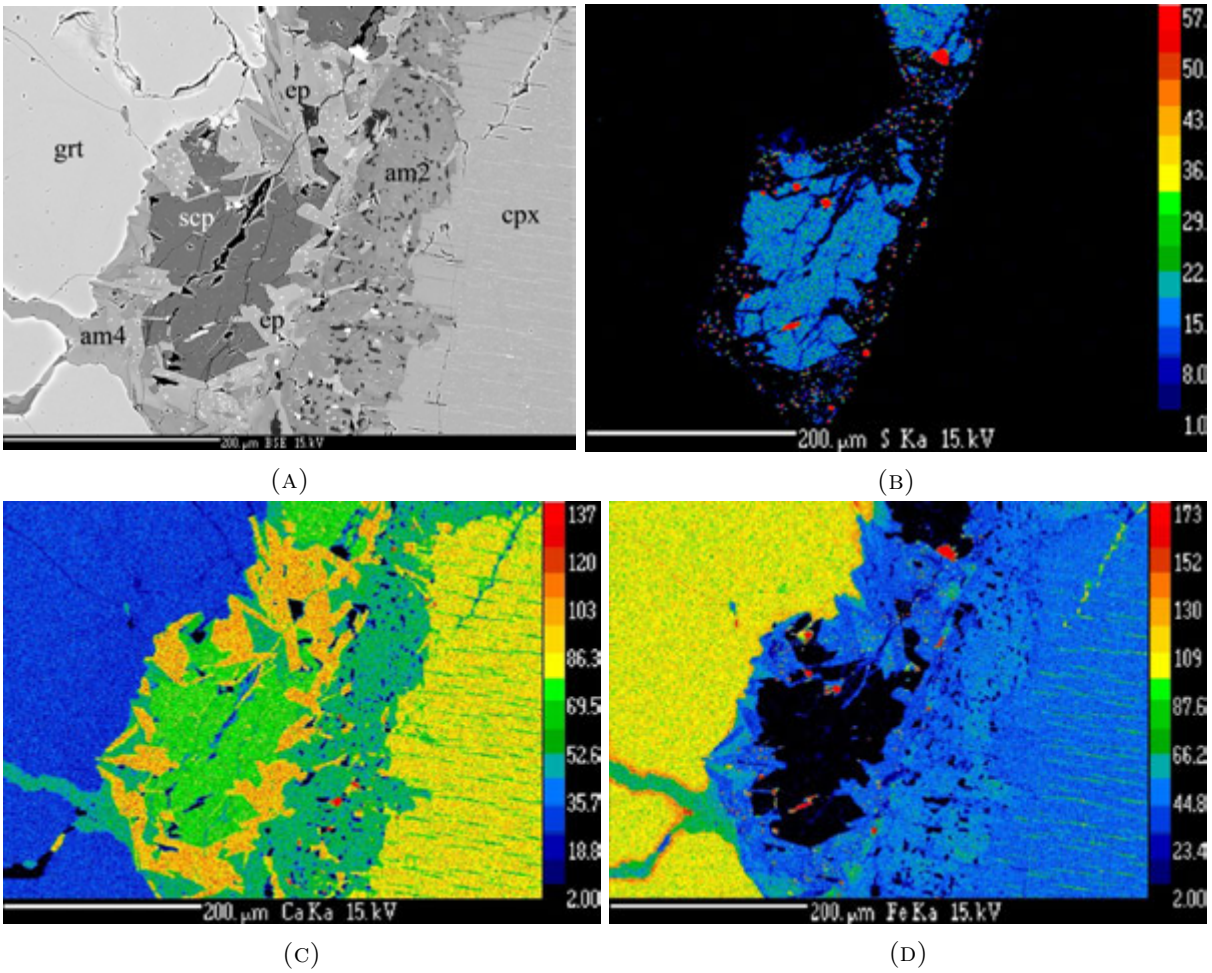

(A) (B)

(C) (D)

FIGURE 4.7: BSE and element mapped images of an area of HIL13-15A (A) A BSE image of a scp grain (centre) bounded by ep and amphibole rims. The grain on the left is garnet, to the right is clinopyroxene. Bright blebs within the central region of the photo are sulphides, primarily FeS_2. (B) Sulphur map of the same scp from (A) showing sulphide blebs as red dots and the scp grain as blue. Note the smooth, continuous boundary the sulphides form, that cut through the am and ep grains. (C) Element map of Ca, distinguishing the ep from the am alteration around the scp. (D) Mapped Fe, the red showing high Fe content, highlighting the Fe sulphides, also seen in (B). Amphiboles on the left and right side of the scp grain can be distinguished by differences in Fe content.

$$cpx + Fe + Mg + H_2O \longrightarrow am2 + qtz + Ca \tag{4.9}$$

$$grt + Ca + Na \longrightarrow am4 + Fe \tag{4.10}$$

Comparison of the S-mapped image and the Fe-mapped image (Fig. 4.7d) shows a correlation between Fe and S. Thus, most of the bright blebs in the BSE image are likely iron or Cu-Fe sulphides. Some of the white blebs correspond to Ca-highs (see Fig. 4.7c), and are likely apatite grains.

Differences in the amphibole compositions between those formed next to garnet and those formed next to cpx can be seen comparing the Fe- and Ca-mapped images. Amphiboles (am4) formed during the breakdown of garnet, have a lower Ca content, and a higher Fe content. The amphibole (am2) between the cpx and scp is also formed together with quartz; the small, dark blebs within the am2. Also seen from the Fe-mapped image, is a high Fe-garnet rim in contact with am4. The composition of the epidote is consistent regardless of bounding minerals.

The reaction forming amphibole from cpx releases Ca into the system, which can be used to form epidote. The breakdown of garnet to amphibole releases Fe, and can also form epidote. Note that the Fe from garnet is divalent, whereas the Fe in ep is trivalent, requiring oxidization. This may be accomplished through reducing the sulphate in scapolite from +6 to -2 in a redox reaction.

4.1.3.1 Petrography of scapolite-rich veins across the granulite-amphibolite transition

As veins are particularly enriched in scapolite and can be followed across both static and hydrated fronts, and where hydration is associated with deformation; three veins were chosen for detailed study. Here, a sampled pair, ISD13-07A and ISD13-07B, was collected from an anorthosite wall, where a scp-px vein is traced from granulite facies mineralogy to amphibolite, under static conditions. The 'A' sample is from the more granulitic part of the rock, where an area of lilac-grey anorthosite with visible garnet coronas is seen. The 'B' is from the amphibolite zone of bleached white anorthosite where the garnet coronas no longer exist, replaced by amphibole-chlorite lenses. The samples were taken approximately one metre apart. Figure 4.8 shows the vein along which the pair was taken.

In general, the macroscopic differences observed between the granulite and the amphibolite samples are: a reduction in garnet and pyroxene in the wallrock, and a reduction in the amount of sulphides, scapolite and pyroxene inside the vein as the rock becomes more hydrated. More amphibole and epidote are found in the 'B' sample.

Figure 4.9a shows ISD13-07A2 (the thin section of ISD13-07A) and Figure 4.9b shows ISD13-07B, the thin sections representing the granulite and amphibolite veins, respectively. The vein is to the left of the red dashed line in Fig. 4.9a and between the red lines in Fig. 4.9b.

FIGURE 4.8: A grey scp-px vein within coronitic anorthosite, runs from top to bottom of this photo. The red boxes indicate the locations of the 'A' and 'B' samples of ISD13-07. Note towards the bottom of the photo, the anorthosite becomes more white and the coronas no longer contain garnet. Also shown are other scp-px veins splaying at high angles to the main vertical vein, typical for this area.

Thin section ISD13-07A2 shows the anorthosite on the left side of the figure (see Fig. 4.9a). It is composed of medium to coarse grained opx and cpx with coronas of garnet, plagioclase and scapolite. Garnet and plagioclase make up the largest compositional percentage of the granulite, but are non-existent within the scp-px vein. There are no sulphides present outside the vein.

Clinopyroxene and S-scapolite make up the majority of the vein of ISD13-07A2, with amphibole and epidote forming reaction rims around pyroxenes. The scapolite has sulphur contents predominantly above 6.0 wt.% SO_3, the highest at 7.01 wt.%. Iron oxides, plagioclase, apatite are also present in the vein. Calcite, clinozoisite, alanite, and large amounts of apatite, and possibly zeolites are also found in close association with the sulphide veinlet (Figure 4.10a). There is a semi-continuous sulphide veinlet, rich with Cu, Fe and Ni sulphides, such as pyrite, pyrrhotite, chalcopyrite, pentlandite and violarite (Figure 4.24b). The large amount of sulphides in this vein, and associated high-S scapolite, suggests that any further breakdown of S-scapolite may only contribute to the total sulphides in a rock, and not be the primary source. Larger blebs and amalgamates of sulphides within the finer-grained bleb clouds are especially likely to be sourced from previously formed sulphides.

Figure 4.10b shows a partially reacted scapolite grain beside a low-Ca pyroxene (pigeonite).

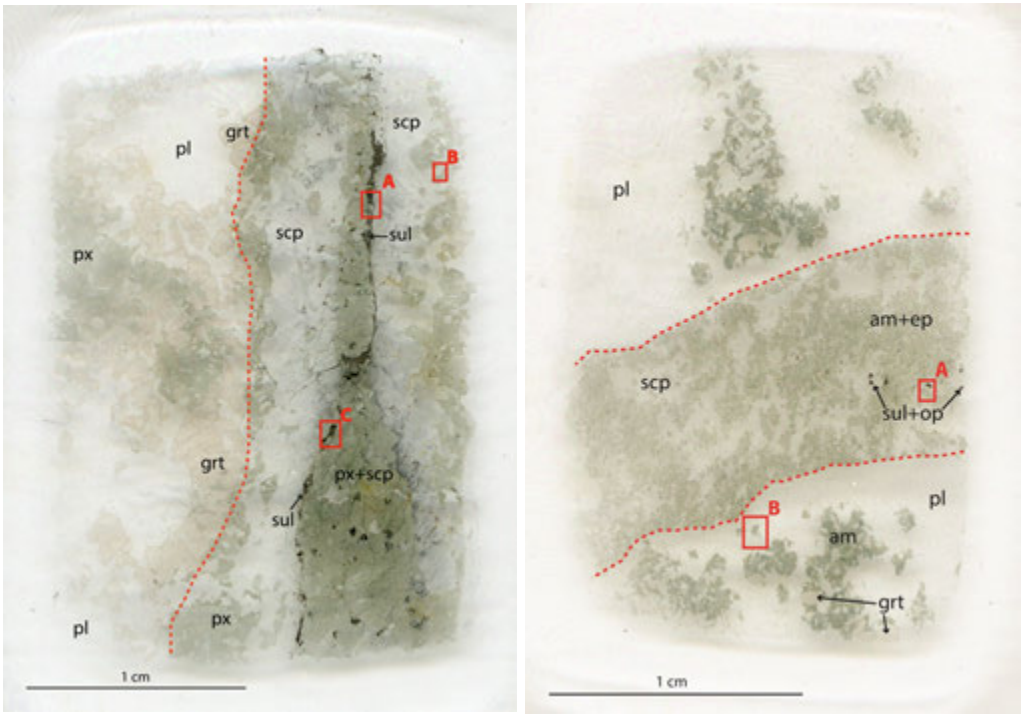

(A) (B)

FIGURE 4.9: (A) A photo of thin section ISD13-07A2, showing the vein to the right of the red dashed line, and the anorthosite to the left. Figures 4.10a, 4.10b and 4.24b are defined by the red boxes 'A', 'B' and 'C', respectively. Note the long sulphide veinlet running down the length of the vein on the pyroxene-scapolite border. (B) Thin section ISD13-07B, showing a vein between the red dashed lines. Figures 4.11a and 4.11b are defined by the red boxes 'A' and 'B', respectively. The anorthosite is hydrated, with pyroxenes completely amphibolitised. The vein is composed mainly of am, pl, ep and is highly porous.

Both grains show reactions rims: scapolite is reacted to epidote containing sulphide blebs, whereas pyroxene is reacted to amphibole. Also in contact with the scapolite grain are clinopyroxenes, which have reacted to form a low Si-amphibole plus quartz at the epidote-sulphide boundary. The proposed original scapolite boundary is marked in this figure with a dashed line, where the epidote-sulphide reaction rim borders the amphibole and pyroxenes. Proposed reactions are as follows:

$$pgt + H_2O + Ca \longrightarrow am + Fe \tag{4.11}$$

$$cpx + H_2O + Al \longrightarrow am + qtz + Ca \tag{4.12}$$

and Eq 4.7

$(S)scp + H_2O + Fe + Ca \longrightarrow ep + sul + Si + Na + CO_2$

Eq 4.7 is identical to the reaction seen in HIL13-15A.

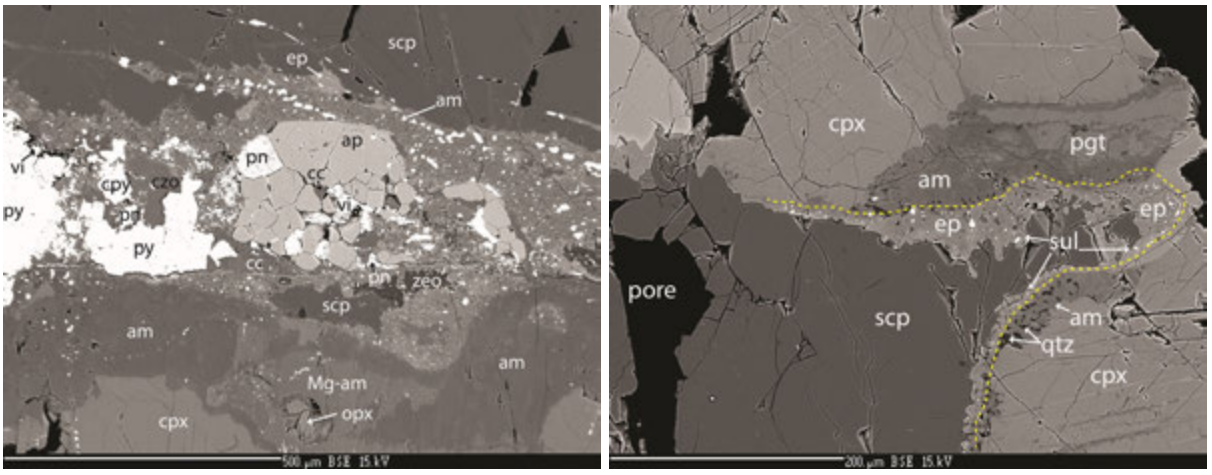

(A) (B)

FIGURE 4.10: BSE images of ISD13-07A2 (A) A sulphide rich vein containing apatite, calcite and amphibole. Note the opx in the centre-bottom reacting to low Ca-amphibole and high Ca-am. Ni-Fe and Cu-Fe-rich sulphides are present and are contained within the am and ep alteration. (B) Within the scp-px vein, a Ca-poor pyroxene, pigeonite, is altering to low Ca-amphibole and cpx. The yellow dashed line indicates the former scp grain boundary, according to location of sulphide blebs in the ep alteration rim. This is a good example of replacement, whereby sulphides form from scapolite.

Water is required for all of these reactions to proceed. The breakdown of pigeonite provides Fe needed to form sulphides from the scapolite. The breakdown of the clinopyroxene adds Ca to the system, which can be used to form amphibole and epidote. The breakdown of scapolite also adds Si to the system, which may partially account for the quartz blebs at the old scapolite border (dashed line) and the amphibole. Importantly, however, is the release of SO_4^{2-} from the scapolite, providing the S to form sulphides.

The wallrock of ISD13-07B is approximately 85% andesine plagioclase. There is a 1 mm zone between the vein and regular anorthosite which is composed almost entirely of fine-grained recrystallised plagioclase. Its composition is slightly richer in Na, increasing from Ab_{64} to Ab_{68}. Minor anhedral meionite (Ca and CO_3-rich) scapolite and epidote are also found within the pl.

Amphibole is blue-green to yellow-green pleochroic crystals that occur with tabular, slightly preferentially aligned epidote, to make up approximately 10-15% of the wallrock. One partial pyroxene can be seen, but most are altered to amphibole, epidote and minor biotite, with chlorite alteration.

Garnet abundance in the wallrock is reduced, compared with ISD13-07A2, to about 1% of the anorthosite, and has a globular appearance. Also present in small quantities, is white mica and fine-grained apatite.

Within the vein, amphibole increases in occurrence to approximately 65%, and its composition has increased Mg and Si contents. Amphibole occurs together with fine-grained, rounded to ovoid quartz in a symplectite texture.

Singular sulphides are present within the vein, up to 0.5 mm in size. They invariably are encompassed by reaction rims of iron oxide and are eaten in appearance (Figure 4.11a).

Porosity is increased, as can be seen from Figure 4.11a. Scapolite, amphibole, epidote, quartz and chlorite all exist together as anhedral, unaligned masses with 5-10% porosity. It is possible some of the porosity was created during the thin section making process, but due to its extent, it is likely most was created through natural processes. Moreover, the porous nature of the vein can be seen with the naked eye in the hand sample, and porosity over the entire vein may be less than 5%. The pores are variable, irregular in size (few microns to millimetre size) and shape, and occur consistently throughout the vein. Also noted, is an increase in porosity in the wallrock, which appears to be, at least in part, associated with scapolite (see Fig. 4.11b). Given the significant differences between the mineral assemblages in ISD13-07A2 and -7B, the porosity may be caused by the loss of many minerals, including pyroxene and garnet outside the vein; and sulphides, apatite, scapolite and pyroxene inside the vein. The creation of porosity is important in that it allows fluids to infiltrated the rock, bringing in new chemical species and providing space for new minerals to form (Engvik et al., 2008). Also of note, is the oxidised rims around the sulphides, which may help to explain why the rock is sulphide deficient. The rock may have been subjected to oxidising conditions after sulphide deposition, leading to their breakdown and subsequent removal.

Scapolite compositions, both inside and outside the vein, are meionitic, though SO_3 content is slightly higher in the vein, averaging 2.76% (from two samples) in the wallrock, to 3.25% (six samples) inside the vein of sample ISD13-07B. However, there is an overall decrease in the amount of sulphur in the scapolites compared to the granulite sample, ISD13-07A2. The sulphur content is nearly halved, from an average of 5.92 to 3.02 wt.% SO_3.

The amphiboles in the wallrock of ISD13-07B are high Al and low in silica, as well as decreased in CaO content, and increased in FeO. An amphibole of near-tremolite composition was also detected within the vein, weathering to chlorite (see Fig. 4.11a). Inside the vein, amphibole is associated with quartz, and appears to be partially zoned in close proximity to the pore space.

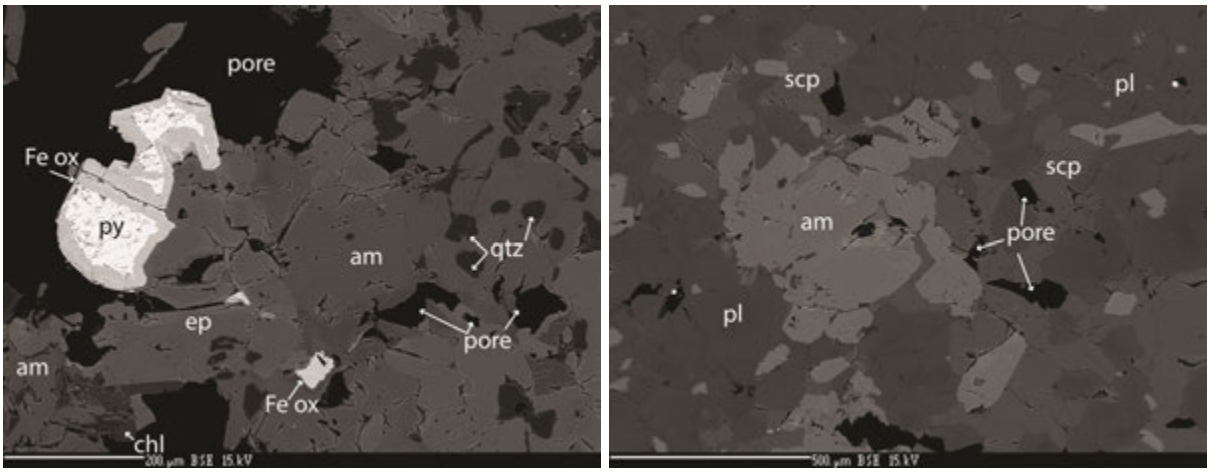

(A) (B)

FIGURE 4.11: BSE images of ISD13-07B (A) Inside of the vein, showing the large amount, including variable size and shape, of porosity, and the oxidisation rims around the sulphides. Typical mineralogy is am, qtz, and ep. (B) The wallrock, showing porosity in and around scapolite, as well as the anhedral and irregular appearance of both the scapolite and the pores.

4.1.4 Shear localisation in scapolite-rich veins

Within the scapolite zone of HIL13-15, many shears can be seen cutting through the rock, both macroscopically and microscopically. Box 'B' in Fig. 4.6b marks the area of Figure 4.12a, which shows multiple 100 μm shears passing through meionitic scapolite. The yellow line in the figure marks the scapolite 'front' boundary between the anorthosite (left) and the scapolite zone (right). Compared to the scapolite, the plagioclase is relatively unaffected by the shearing, as the shears have limited penetration across the 'front' and into the plagioclase. They pass left-right through the photo, and show the scapolite within the shears has undergone subgrain rotation, and recrystallised as finer-grained, preferentially oriented grain aggregates. The red box of Fig. 4.12a delimits the area of Figs. 4.12b through 4.12d.

The scapolite in this zone averages 3.55 wt.% SO_3 (seven grain average). From the cross-polarised image, the area of the shear zone was determined by using the extent of the finer-grained, recrystallised scapolite as the outer boundaries. This is drawn on Fig. 4.12b as red dashed lines to delimit the shear zone. This figure is a plane-polarised image showing predominantly meionite, with clinozoisite and epidote inclusions. The epidote laths are fewer, yet larger, within the shear zone and are accompanied by opaque blebs. The same area is shown as a BSE image in Fig. 4.12c, where the opaques appear as white blebs of predominantly iron sulphide. It is clear that the sulphides are concentrated and enlarged within the shear zone along with large, preferentially oriented ep grains.

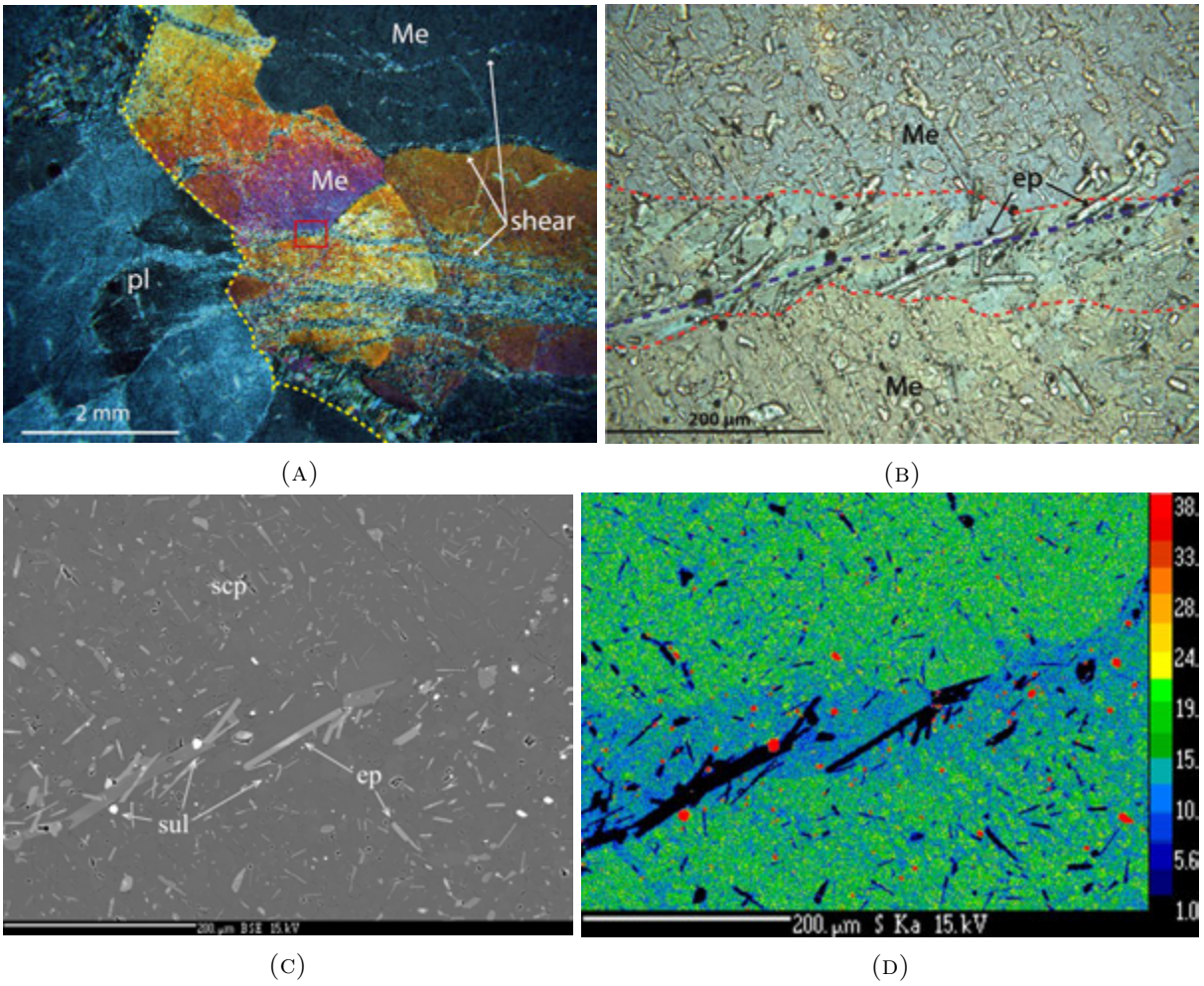

FIGURE 4.12: (A) A xpl micrograph of the scp-anorthosite boundary, indicated with a yellow dashed line, of HIL13-15. Multiple shears can be seen within the scp, but have limited penetration into the pl. The red box delimits the area shown in (B), (C), and (D). (B) Close up of (A), indicating with red dashed lines the shear zone boundaries. The blue dashed line indicates the scp grain boundary. Compare with the low-S zone of (D). (C) A BSE image of the shear zone showing higher concentrations of sulphides and epidote laths along the grain boundary and within the shear zone. Bright dots are sulphide blebs. (D) The same shear zone, seen through mapping the S content of the scp grains. The central blue zone indicates lower S content. Red dots represent primarily Fe sulphides concentrated within the shear zone, together with epidote (black).

In Figure 4.12d, the same area is shown as a sulphur-mapped image. Red blebs, representing high sulphur areas, correlate to the sulphides of prior images. A linear, low-sulphur zone crossing the image from left to right is coincident with the area marked as the shear zone and grain boundary in Fig. 4.12b. The shear zone scapolite has a lower S content than the surrounding rock. Within the shear, values of SO_3 average 3.03 wt.%, whereas outside the shear, it averages 3.70%. A possible reaction for the mineral assemblages shown here is:

$$(S)scp + Fe + CO_2 + H_2O \longrightarrow (C)scp + ep + sul \tag{4.13}$$

A water- and carbon dioxide-bearing fluid is needed for this reaction to occur, together with a metal (Fe) source. Redox reactions between the oxidised epidote may accommodate the reduction of sulphur needed to form sulphides. Required fluids can be introduced along the shear pathways.

A shear zone is observed in thin section AK72-98II. Figure 4.13a shows a granulite facies garnet-rich anorthosite in contact with a pyroxene-rich vein, outlined with a red dashed line, in thin section AK72-98II. Within the vein, a shear zone is apparent, crossing the photo from right to bottom-left. The area in which the greatest deformation occurs, is marked with yellow dashed lines. Within this zone, mineral aggregates appear elongated, and the opaques, ilmenite and hematite, are less abundant than within the non-sheared part of the vein. Cpx, opx, opaques, plagioclase, scapolite and apatite are also common within the vein; however, opx is limited to within the shear zone and no opx grains were identified outside the sheared section. The opaques include oxides of ilmenite and hematite, as well as sulphides: pyrite, pyrrhotite, cubanite, chalcopyrite and pentlandite. Figure 4.13b is a ppl image of the shear zone, showing an increase in deformation towards the bottom of the photo. The S and C structures indicating the direction of movement are marked with a yellow arrow. Grain boundaries appear fuzzy, forming a dark shadow over most of the area.

Figures 4.13c and 4.13d show the same opx grain, marked with a red box in Figure 4.13b, as a BSE and ppl image, respectively. Evident in the BSE image are several amphibole reaction rims forming away from the opx grain boundary. The lighter grey amphibole, marked am1, is a very low Ca-amphibole, approximating anthophyllite-cummingtonite composition. Outwards from the opx and am1 grains, is a darker grey amphibole, labelled am2. This amphibole contains more Ca, and less Fe than am1, approximating tremolite-actinolite composition. The third amphibole, marked am3, is bounded by am2 and multiple, fine-grained, rounded quartz blebs, and lies within an ovoid zone of scapolite, sulphides and plagioclase. It is included with sulphide blebs and differs compositionally from am2 in that it has less Si and Mg, more Al and Fe. A portion of the Fe is trivalent. It is likely the quartz formed as a result of the alteration of am2 to am3, as am3 decreases in SiO_2 content, from 51 to 42 wt.%.

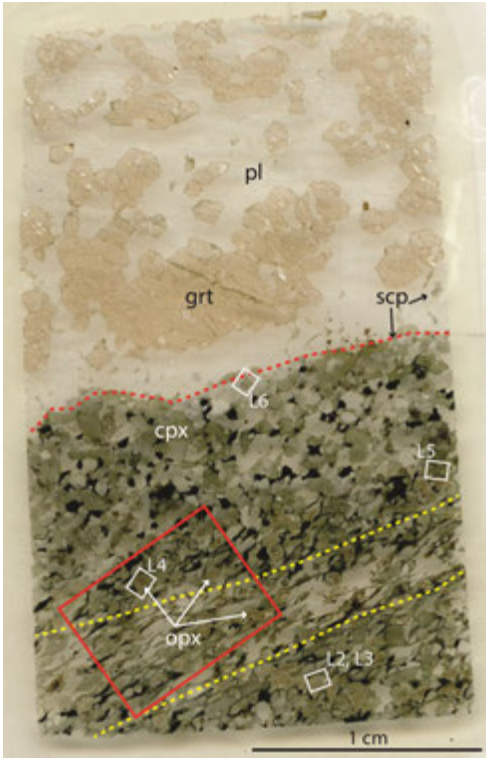

(A)

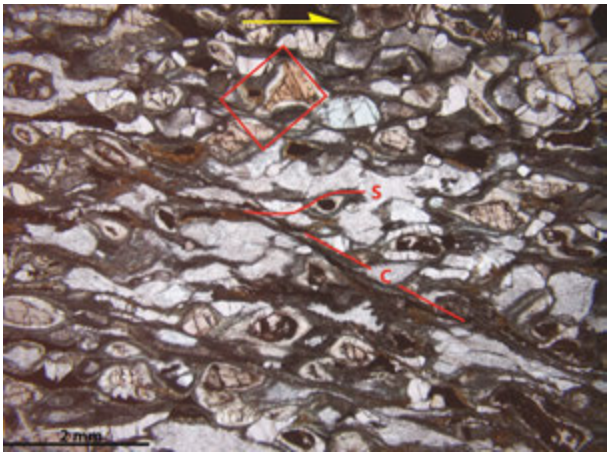

(B)

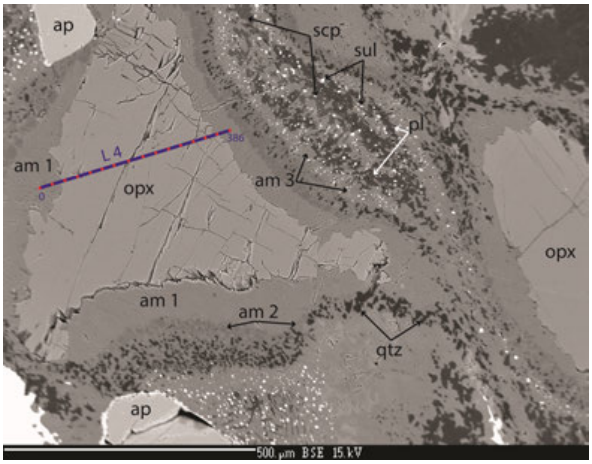

(C)

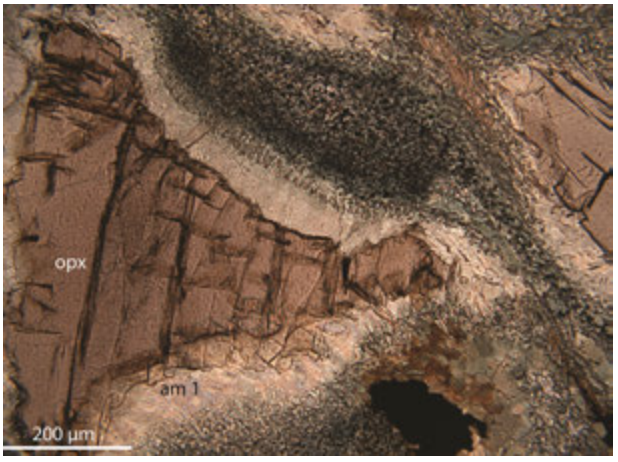

(D)

FIGURE 4.13: (A) Thin section of AK72-98II showing the boundary between garnet anorthosite (top) and a mafic vein. The yellow dashed lines indicate the central part of the shear passing through the vein. The red box marks the boundary of (B). The white boxes highlight the pyroxenes analysed for Ni and Cu concentrations as Lines 2 through 6 (see Section 4.2.5.1). (B) A close up ppl micrograph of the shear zone in the mafic vein. The S-C structures and direction of movement are indicated. Note most of the grain boundaries have a cloudy, unsharp appearance. The red box delimits the area of (C). (C) A BSE image of opx reaction rims next to a degraded and sheared, former scapolite grain. Note the three different amphiboles between the opx and the scapolite-sulphide grain. Also shown is the sulphide 'tail' of the grain being pulled into the sheared foliation towards the bottom right part of the image. The blue line with red dots indicates trace element analysis locations of Line 4, see Section 4.2.5.1. Also see Discussion Section 5.3 for mineral area analysis of this image. (D) A ppl photo of the area in (C). Note the transparent, fibrous appearance of the low Ca-amphibole (am1) bordering the opx, as well as the dark, cloudy appearance of the former scp vein.

The ovoid grains contain scapolite, amphibole (am3), plagioclase and pyrite blebs. The scapolite in the blebs is very high in sulphur content, containing between 5.41 and 6.34 wt.% SO_3. The scapolite is anhedral, irregular in shape, and porous in nature. Here, scapolite is found together with plagioclase, which is sodic, between An_{22} and An_{36}. An argument can be made that the scapolite broke down to form the plagioclase, sulphides and amphibole within this ovoid grain. See the discussion for more details. This same series of amphibole reaction rims around opx, and mineralogical changes of scapolite and sulphides, occurs throughout this sample, inside the mafic vein (see also Figure 4.27b).

The ovoid grains are deformed such that part of the amphibole and sulphide blebs are pulled into the shear fabric. This indicates the sulphides have a certain degree of ability to move from their source. Notable is the sulphide blebs themselves are not elongate, but they are separately stretched in a linear fashion, keeping their original roundish shape.

Reactions involving the orthopyroxene and scapolite breakdown to sulphides and amphiboles include:

$$opx + H_2O + Si \longrightarrow am1 \ + Fe + Mg) \tag{4.14}$$

$$am1 + Ca + Al \longrightarrow am2 + Si + Fe + Mg \tag{4.15}$$

$$(S)scp + am2 + qtz + Fe \longrightarrow pl + am3 + sul + CO_2 \tag{4.16}$$

The change from am2 to am3 loses nearly 9 wt.% SiO_2. Three wt.% silica is need to create am1 from opx, but is lost again making am2. The majority of SiO_2 is lost between the am2 and am3, accounting for the qtz blebs forming at the am2-am3 boundary. Within this system, silica is also needed in forming pl from scp, a nearly 10 wt.% increase. Breakdown of scp provides sufficient element species to account for pl and am3 formation, if Fe is acquired from elsewhere. The breakdown of scapolite provides the CaO needed to form the pl, am3 and am2.

FeO is lost through the opx to am1, and the am1 to am2 breakdown reactions. Plagioclase and scapolite do not have much Fe in their structure, am3 is the only mineral increasing its FeO content after breakdown from the opx. The remaining Fe can be taken by the sulphides.

4.1.4.1 Shearing along a scapolite-rich vein, HIL13-16 and HIL13-17 comparison

The next two subsections describe in detail pairs of samples along veins taken across shear zones, in order to analyse compositional and textural changes in scapolite and sulphides. The sampled pairs are HIL13-16 and HIL13-17, and ISD13-01A and ISD13-01B. HIL13-16 and ISD13-01A correspond to the less sheared part of the rocks. HIL13-17 and ISD13-01B are taken from inside or close to a shear zone. The Isdal samples were taken from the same vein, whereas the Hilland samples were collected from two different veins found in the same area.

The wallrock of HIL13-16 (see Fig. 4.14a) is a garnet-bearing granulite anorthosite in the beginning stages of static retrogression. Plagioclase is approximately 85% of the wallrock. Up to 50 μm long clinozoisite laths occur as inclusions within pl grains, evidencing the anorthosite retrogression. Larger, rounded garnet grains, up to 3 mm wide, consist of 5% of the total rock composition. They also have been slightly amphibolitised, as they have thin reaction rims of amphibole and epidote.

Also in the wallrock, S-scapolite is present as light grey, 0.5 mm sub-rounded grains, making up approximately 5% of the anorthosite. Tiny 1-5 μm wide iron sulphide blebs encompass scapolite (scp) grains in association with epidote (ep) and white mica laths (see Fig. 4.15a). These form the static reaction rim around scapolites in most of the section. Opaque minerals (op), including ilmenite and hematite, invariably have biotite reaction rims.

Within the vein of HIL13-16, bounded by red dashed lines in Fig. 4.14a, is primarily amphibole and quartz simplectite, and epidote, totalling approximately 65% of the rock. Compared to the wallrock, the vein is nearly completely hydrated to amphibole, though the vein is not reacted due to shearing, as seen in HIL13-17.

There is reacted, unstable feldspar (15%) and scapolite (5%) also occurring within the vein. The scp within the vein is much more broken down than in the wallrock. Figure 4.15b shows the extent of epidotisation of outer scapolite grains, leaving only the central scp grain intact. Where the epidote is formed, extensive amounts of sulphide blebs can be seen, both on the sub-μm scale and up to 70 μm wide. Sulphides are primarily Fe rich. Note how the epidote, sulphides, remaining scapolite and calcite form a pentagon shape, suggesting a former grain boundary.

Comparing the vein and the wallrock, scapolite shows only a slight difference in SO_3 composition, varying from 5.28 to 5.88 wt.%. All readings for scp in HIL13-16 indicate a silvialite composition.

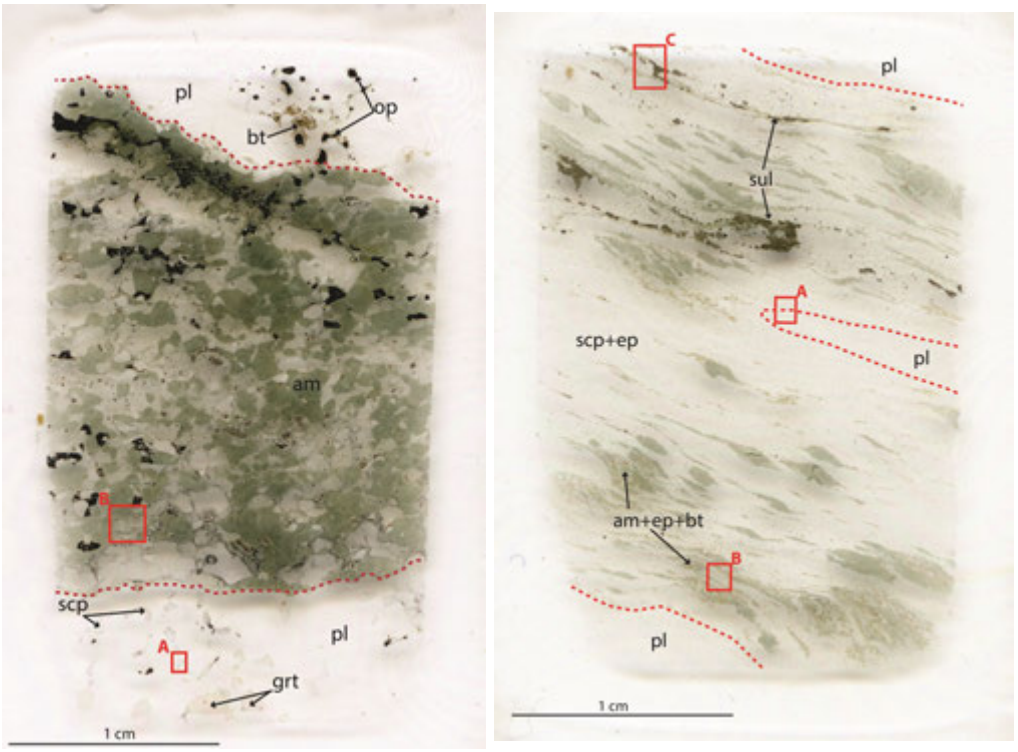

(A) (B)

FIGURE 4.14: (A) Thin section of HIL13-16 showing granulite facies anorthosite and amphibole rich vein between the red dashed lines. The red box labelled 'A' delimits the area of Fig. 4.15a, 'B' delimits Fig. 4.15b. (B) Thin section of HIL13-17 vein. The wallrock is plagioclase-rich anorthosite labelled pl. The red box labelled 'A' delimits the area of Fig. 4.16a, 'B' delimits Fig. 4.16b and 'C' is Fig. 4.24d. Note the strong foliation and the 'eye' formation of the amphibole-mica rich areas. The sulphides are also entrained into the foliation as amalgamated strings.

Of note; however, within the vein, calcite is a replacement mineral after scapolite, suggesting a fluid with a high CO_2 content was present.

Also seen within the vein are ilmenite grains that are associated with titanite and rutile, all encircled by μm-sized zircon grains. Apatite is also abundant, presumably hydroxylapatite, due a very low Cl content, which constitutes between 5 and 10% of the vein.

HIL13-17 represents a sheared anorthosite containing a vein composed primarily of recrystallised scapolite. The mineral assemblages of scp, ep, am, and bt are all recrystallised, showing a strong fabric of grain shaped preferred orientation, and directional alignment of platy minerals. Plagioclase appears only in the wallrock, though displays the same directional fabric. The wallrock in Figure 4.14b, marked with red dashes and labelled pl, are primarily plagioclase with epidote and clinozoisite laths. The pl is occasionally reverse zoned, with Na-rich pl on the inside (An_{22}) and Ca on the outside (An_{40}). Epidote is also zoned, with Fe-rich ep on the outside (7.35

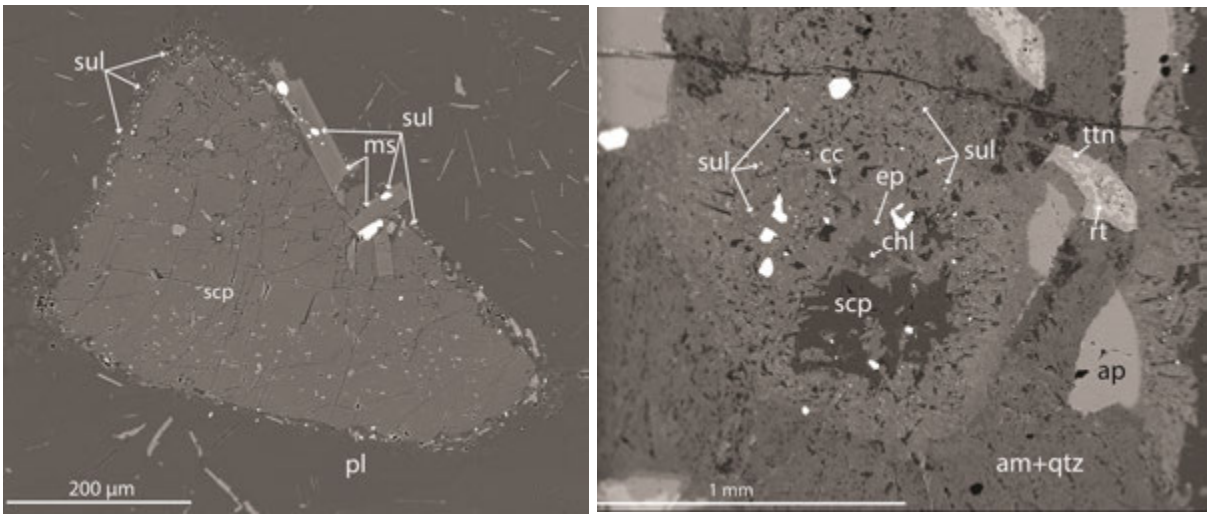

(A) (B)

FIGURE 4.15: BSE images of HIL13-16. (A) A scapolite grain encompassed by sulphide blebs, in plagioclase of granulitic anorthosite. (B) A grain from within the vein showing a scp core encompassed by epidote and amphibole, with abundant sulphide-bleb inclusions.

wt.% FeO), losing Fe toward the outside of the crystal to 5.60%. Figure 4.16a shows the mineral zoning, the contact between the scp vein and the sheared anorthosite and directional fabric of the mineral assemblages. Iron content within epidote changes from HIL13-16 to HIL13-17. All iron within epidote is considered Fe^{3+} and decreases from an average of 9.45 to 7.19 wt.% from the granulite to the amphibolite facies rock; however, the occurrence and size of epidote increase in the amphibolite (see Table A.5 of the Appendix).

In Figure 4.16b, the bright blebs within the scapolite are Fe and Cu sulphides, whereas the small bright blebs within the am and qtz aggregates are Fe-Ti oxides and rutile.

The scapolite is meionitic, though one grain of silvialite was detected (see Table A.2 of the Appendix). Some scapolites have an intergranular 'film' of Na-rich plagioclase following their grain boundaries. Also seen are zeolites, such as analcime (after albite) and calcite, and biotite changing to chlorite along laths. These hydrated minerals suggest lower grade PT conditions may have be reached during or after shearing at amphibolite conditions.

Within the scp-ep vein, two modes of sulphides exist. First, linear aggregates of Fe, Cu and Ni sulphides (pyrite, chalcopyrite and millerite) are formed within the main foliation. Trace amounts of Ni and Co were detected in the pyrite. Second, outside the sulphide linear features, sulphide blebs are ubiquitous within the scapolite groundmass. Sulphides are especially

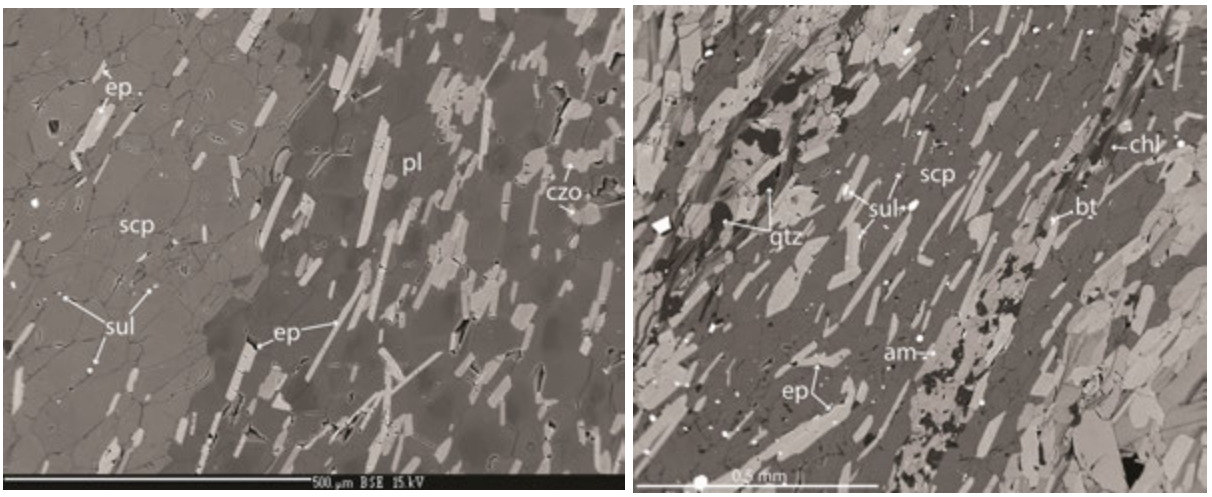

(A) (B)

FIGURE 4.16: BSE images of HIL13-17. (A) The boundary between the scp vein (left) and the plagioclase of the anorthosite in HIL13-17 can be seen. Note the strongly oriented minerals and the zoning of the plagioclase and epidote. Also note the sulphides distributed throughout the scp. (B) This image is from a high-amphibole and biotite area, also showing the strong foliation of mineral aggregates. The number and size of sulphide blebs are increased in the scapolite.

abundant close to the biotite-amphibole zones, and also contain traces of Cu and Zn in the pyrite.

Most samples in the study area have undergone varying degrees of amphibolite overprints and deformation. Another vein is examined from an amphibolite rock that is progressively more sheared.

4.1.4.2 Shearing along a scapolite-rich vein, ISD13-01A and ISD13-01B comparison

ISD13-01A and -B were taken from a new road cut at the Isdal location, approximately one metre from each other, along the same dark scp-px vein within anorthosite (see Figure 4.17). The 'A' sample was taken from an area of lilac-grey anorthosite with visible garnet coronas. Near to sample ISD13-01B, the vein can be seen being pulled into the foliation of a shear zone toward the left side of Fig. 4.17.

Thin section ISD13-01A (Fig. 4.18a) is within the more original, less sheared anorthosite. Plagioclase makes up approximately 80% of the wallrock. It has partially undergone dynamic recrystallisation through bulging along the grain boundaries, producing a fine-grained rock. Though most of the thin section is only partially recrystallised, the bottom left corner has

FIGURE 4.17: Locations of ISD13-01A and ISD13-01B in relation to their common vein. Note the 'A' sample is in an area with darker lilac-grey plagioclase and garnet coronas. The 'B' sample is within the zone of bleached white pl and near to a shear zone that disturbs and 'sucks in' the foliation of the main rock, as indicated by the arrow.

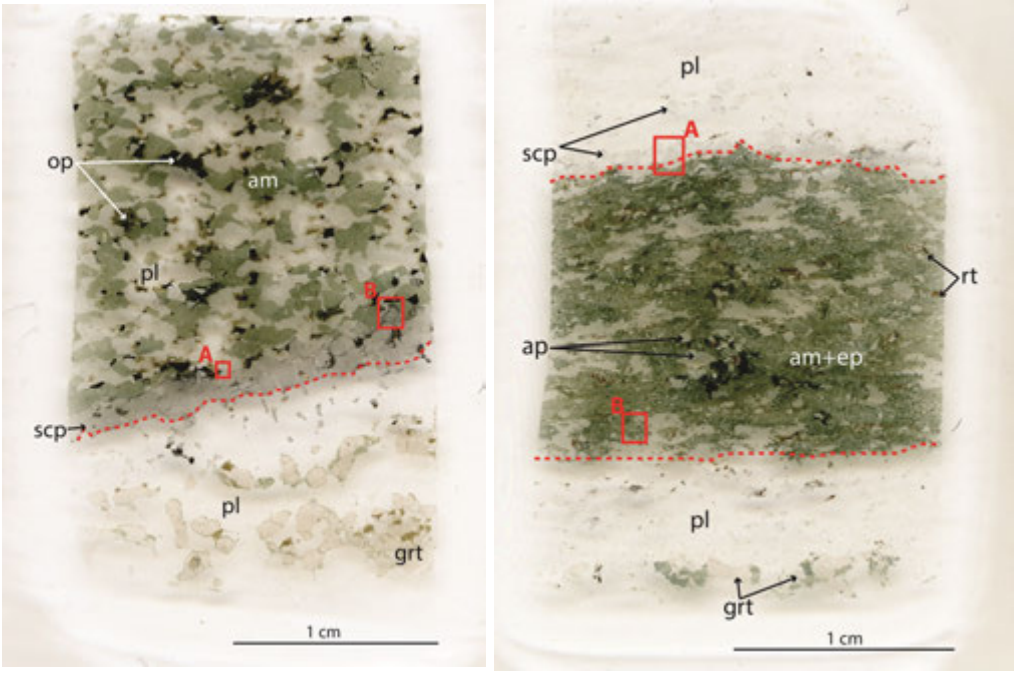

(A) (B)

FIGURE 4.18: (A) Thin section of ISD13-01A, with vein above the red dashed line, and granulitic anorthosite below. Note the grey scapolite following the base of the amphibole-rich vein. Also abundant are Fe-Ti oxides (intergrown ilmenite and hematite). (B) Thin section of ISD13-01B with vein delimited by dashed red lines. The vein is apatite and rutile rich, and the anorthosite is contains less grt. Scp is still present, primarily along the upper vein contact.

undergone complete recrystallisation to very fine-grained, unidirectional plagioclase crystals, likely through bulging and subgrain rotation. This indicates the section is in close proximity to a shear zone, confirming field observations.

Garnet grains are abundant in the wallrock, consisting of 10% of the anorthosite in the thin section. They are rounded and cracked, average 2 mm in size, and have biotite, epidote and amphibole reaction rims. Also present are small aggregates of rutile completely encompassed by biotite.

Scapolite exists as small, inter-plagioclase, subhedral, sub-triangular shaped crystals within the wallrock, similar to the granulite sample, HIL13-19. It exhibits a low-order orange birefringence and is meionitic in composition.

Scapolite is also present on the boundary between the vein and the wallrock anorthosite. It can be seen on Figure 4.18a as the grey band stretching across the thin section above the red line. These scapolite grains are three times larger (up to 1.5 mm) than those found in the anorthosite and have a first-order blue birefringence. Sulphur concentrations in scapolite are variable, however, with grains outside the vein having an average of 1.9 wt.% SO_3. Both low sulphur content and silvialite sulphur contents (2.44 and 5.53 wt.% SO_3) were found within and at the edges of the vein.

Tiny blebs of sulphides are extensive along the scapolite grain boundary at the edge of the vein, and are nearly exclusively found within this scapolite zone. The main sulphide present is pyrite, with smaller amounts of pyrrhotite, both of which are nearly always associated with this scapolite band (see Figs. 4.19a and 4.19b).

Plagioclase is of andesine composition, both in the wallrock and in the vein. However, the pl is slightly less Ca-rich within the vein, with compositions ranging between An_{35} and An_{40}. In all cases, the pl is included with multiple fine-grained clinozoisite (czo) and epidote laths.

Inside the vein of ISD13-01A, plagioclase and amphibole are present in large and relatively equal quantities. The amphibole is rimmed by laths of epidote intergrown with quartz, radiating from the am grain boundary, forming a distinct texture (Fig. 4.19a). Epidote at the sulphide and scapolite front contains over 1.5 wt.% more iron than ep found in the centre of the vein, decreasing from an average of 8.58 to 7.27 wt% FeO. This ep also contains many sulphide blebs, whereas those within the central vein, do not.

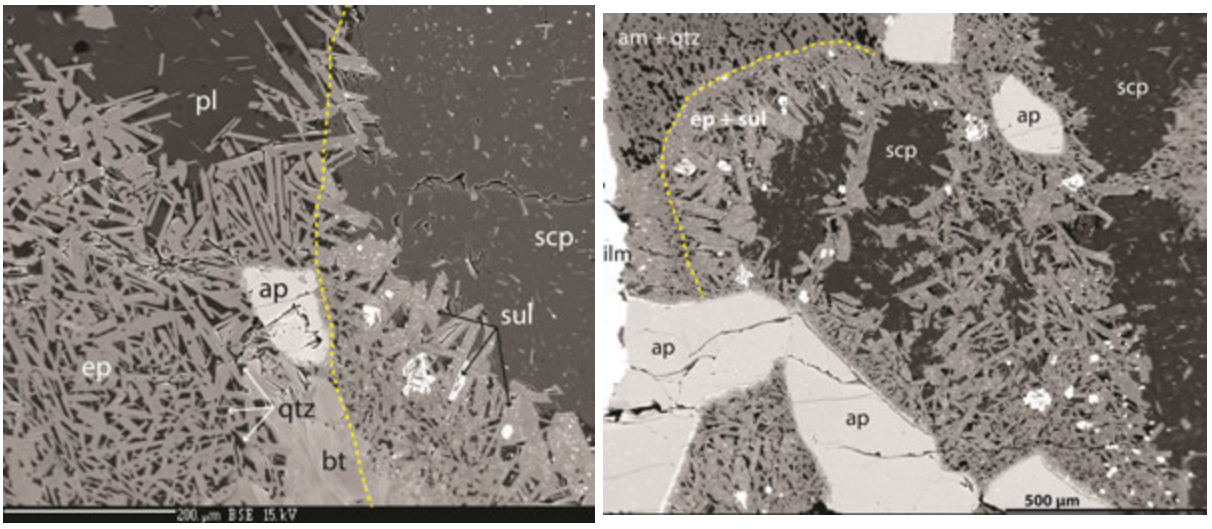

(A) (B)

FIGURE 4.19: BSE images of ISD13-01A (A) At the pl-scp boundary, the presence of sulphide blebs in ep is confined to within close proximity of scapolite. The dashed line delimits the extent of the sulphide blebs and may represent the former scp boundary. Also note the distinct texture between the ep with qtz, and ep with the sulphides, forming long geometric lath intergrowths. (B) The edge of a former scapolite grain, delimited with epidote and sulphides, exhibits a distinct boundary, highlighted with a dashed line. Outside this line, sulphides and epidote are absent, replace by amphibole and quartz. Note also the ep and sulphide intergrowths.

The amphibole in the vein of ISD13-01A contains old pyroxene exsolution lamellae, indicating it is a pseudomorph after pyroxene, that has since been completely replaced. Rutile and opaques, typically Fe and Fe-Ti oxides, are closely associated with each other. These aggregates have biotite rims and consist of approximately 5% of the vein. Apatite is abundant, forming rounded, clear grains that consist of 1-2% of the vein (Fig. 4.19b). Minor scapolite is also present.

Thin section ISD13-01B is shown in Figure 4.18b. Overall mineral assemblage textures indicate this section has undergone dynamic recrystallisation through shearing. Plagioclase is the dominant mineral in the wallrock, making up over 90% of the anorthosite. It has undergone considerable recrystallisation and is predominantly fine-grained with a directional foliation. Relict, coarser-grained plagioclase grains do exist; however, they form only about 20% of the total plagioclase. The abundance of recrystallised plagioclase increases away from the vein to nearly 100% at the edge of the thin section.

Garnet is present, though less abundant in ISD13-01B. It is rounded and elongated parallel to the foliation. Chemical analyses show the composition of the garnet is consistent over the granulite and amphibolite samples, retaining its typical granulite signature of equal parts almandine and

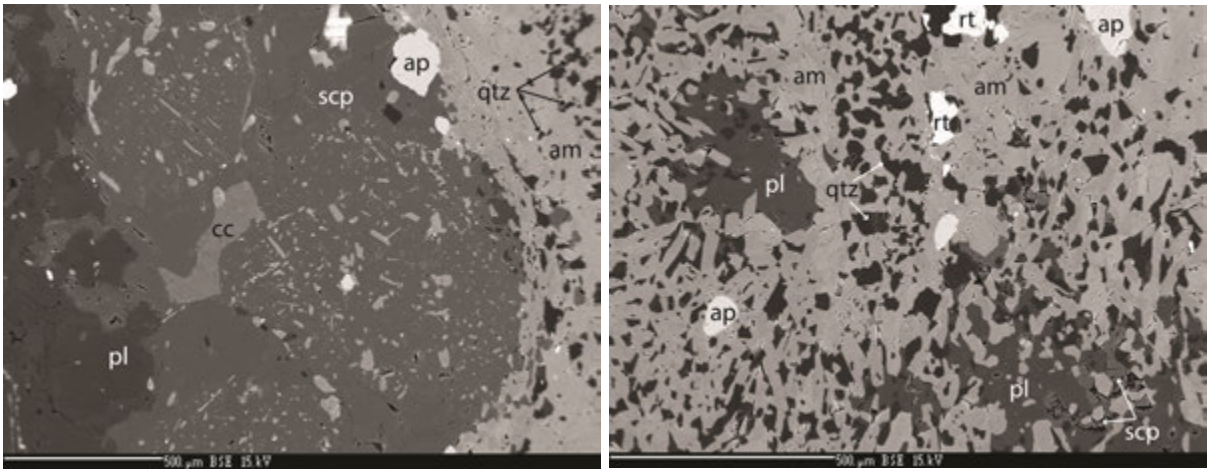

(A) (B)

FIGURE 4.20: BSE images of ISD13-01B (A) At the pl-scp boundary, calcite, abundant inclusions of epidote and clinozoisite within scapolite are present, and there is a distinct absence of sulphides. (B) Within the vein, there is a fabric of directional am-qtz aggregates. Also shown are the pl and scp, both anhedral; scapolite looks particularly 'eaten' and porous. Apatite and rutile are common. Note that sulphides are mostly absent from this thin section.

pyrope. Amphibole and biotite form around the garnet in rims. Clinozoisite and epidote are abundant as inclusions within the plagioclase.

In comparison to ISD13-01A, the distinct grey band of scapolite along the edge of the vein is gone; however, scapolite does exist within the anorthosite close to the vein boundary (Fig. 4.20a). It is anhedral, amoeba-like in shape, and has an orange to blue-purple birefringence. Chemical analyses show a low sulphide content of scapolite inside and outside the vein, averaging 1.32 wt.% over three grains. There is one high S-scapolite detected within the dispersed scapolite band at the edge of the vein, which has silvialite compositions at 5.27 wt.% SO_3. This may represent a relict of granulite facies scapolite. Sulphides are no longer associated with the scapolite. They are few in number and size, and are typically associated with oxides. However, calcite is present within the scapolite, and as thin veinlets cross-cutting the main vein, indicating a CO_2-rich fluid affected the rock, possibly associated with the breakdown of S-scapolite.

Amphibole is the predominant mineral of ISD13-01B, constituting over 50% of the vein. All minerals, including plagioclase and epidote, are recrystallised to a finer-grained fabric parallel to the vein boundary (Fig 4.20b). There are only a few sulphide grains, appearing together with oxides. In contrast to ISD13-01A, sulphides are not associated with scapolite and do not have the multi-bleb habit that appear within amphibole and epidote grains.

Ilmenite and hematite abundance is significantly reduced compared to ISD13-01A, coincidently, rutile occurrence within the vein has increased. Rutile appears as elongated mineral aggregates with a direction parallel to the overall rock fabric. Reactions involving the breakdown of ilmenite to titanite and rutile include:

$$FeTiO_3 + SiO_2 + Ca \longrightarrow CaTiSiO_5 \tag{4.17}$$

$$FeTiO_3 \longrightarrow Fe + TiO_2 + 0.5O_2 \tag{4.18}$$

Also increasing in presence significantly is apatite. The crystals are large, rounded and clear, appearing porphyroblastic and up to 3 mm in size. Apatite makes up approximately 5% of the vein.

4.1.5 Anorthosite-associated rocks

Mafic rocks in the study areas include 'pods' and veins within the anorthosites (Fig. 3.4d), dykes of altered jotunite (Fig. 3.1c) within the anorthosite and mangerite (Fig. 3.1d), and Fe-Ti rich contact rocks with the anorthosite. The mafic rocks have been investigated, not only as potential scapolite and sulphur sources, but also as the possible source of metals for sulphides. Due to zones of intense shearing and overall amphibolitisation of the bedrock, most samples are too altered to provide detailed information about their original mineralogy and composition. This includes the jotunite dyke sample, ISD13-04, and most of the wall rocks around the Espetveit Mine. The mafic 'pod' sample, ISD13-06, and the mangerite contact to the west of the Hilland study area, HIL14-03, contain sufficient original mineralogy to evaluate the metal source potential of pyroxenes. Additionally the mafic, sheared vein sample from Isdal, AK72-98II, was also evaluated and described in Section 4.1.4.

Scapolite from the jotunite (ISD13-04), mafic 'pod' (ISD13-06) and mafic vein (AK72-98II) samples were analysed for their scapolite contents with the EMP. Figures 4.21a and 4.21b are thin section images of ISD13-04 and ISD13-06, respectively. All mafic samples contain silvialite, with some of the highest SO_3 contents detected and reported in literature. The jotunite averaged 5.98 wt.% SO_3, from three measurements. ISD13-06 and AK72-98II averaged 6.02 wt.% and 5.97 wt.%, respectively, from four samples each. All samples exhibit breakdown of scapolite to sulphide blebs in epidote and amphibole.

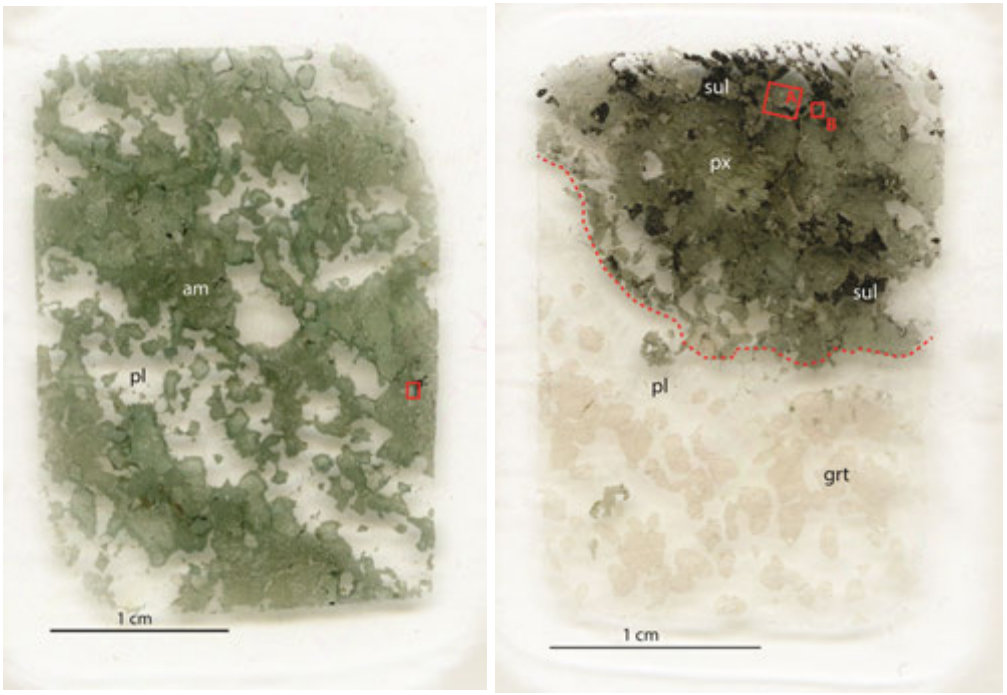

(A) (B)

FIGURE 4.21: (A) Thin section of ISD13-04, amphibolitised jotunite, showing epidote, amphibole (green) from pyroxene, and plagioclase (clear) as the main rock forming minerals. The red box demarks the area of Figure 4.22. (B) Thin section of ISD13-06 showing the distinct mafic 'pod' zone above the red dashed line, and the anorthosite below. Much of the darker minerals in the mafic zone are sulphides, whereas the green is pyroxene with some amphibole alteration. The red Box 'A' demarks the area of Figure 4.23a and Box 'B' is Figure 4.23b.

ISD13-04 (see Figure 4.22) contains 30% andesine to oligoclase (An_{27-30}) plagioclase. Scapolite consists of approximately 5% of the rock. The remaining is primarily amphibole from pyroxene, with epidote, biotite, opaques and rutile. Plagioclase contains epidote and clinozoisite inclusions. Symplectite rims of epidote and quartz are observed between amphibole and plagioclase grain boundaries. Both baryte and calcite are observed, associated with sulphide-amphibole rims around scapolite.

In ISD13-04, there are clear amphibole-sulphide rims surrounding the scapolite (Figure 4.22). Sulphides are primarily iron sulphide and form in 'clouds' within the am, from sub-μm to approximately 15μm sized grains. Amphibole outside these zones appears as a symplectite with quartz. Also associated with this, is a breakdown of ilmenite and hematite to rutile. Zircons are forming chains, encompassing the ilmenite grain, presumably marking the boundary of the original ilmenite grain (see Austrheim et al. (2008)). Examples of zircon rimmed rutile, titanite and ilmenite associations were also observed in many other hand samples including the scapolite front rock HIL13-18 (see page 85), and within the vein of the granulite rock, HIL13-16.

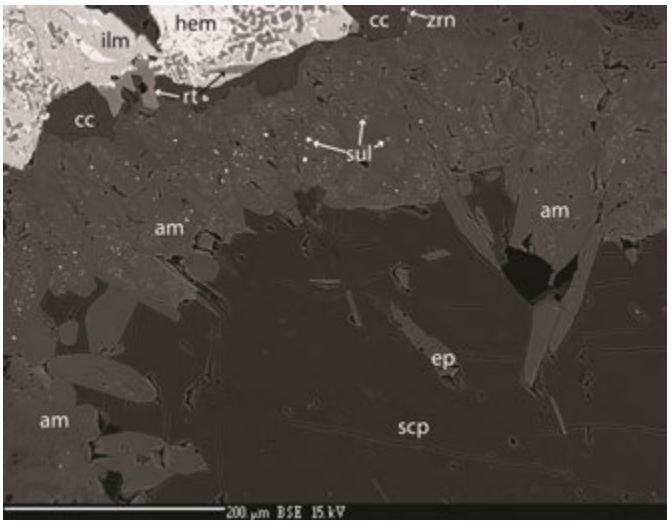

FIGURE 4.22: BSE image of ISD13-04, scapolite with an amphibole and sulphide 'cloud' outer rim. Also shown is the relationship between the breakdown of ilmenite and hematite, forming rutile. The former grain boundary is outlined by a thin 'necklace' of zircons.

In thin section ISD13-06, the mafic pod of the anorthosite is remarkable for the amount of sulphides it contains (see Figures 4.23a and 4.23b). EMP analyses determined it also contains a number of different types of sulphides including: pyrite, pyrrhotite, chalcopyrite and pentlandite. The sulphides are large, amalgamated masses, following linear features within fractured scapolite and pyroxene grains, and as bleb 'clouds' inside amphibole, around scapolite (see Figure 4.23b). Pyroxenes and sulphides are enveloped by amphibole, garnet and sulphide reaction rims.

Outside the mafic pod, the anorthosite has garnet of granulitic composition ($Pyr_{42}Alm_{41}$), the plagioclase is an anti-perthitic andesine (An_{31}) and the scapolite is silvialite (Me_{66-68}, $S_{0.69-0.72}$).

One of the primary differences between ISD13-04 and ISD13-06 is the amount of hydration they have undergone. ISD13-04 is predominantly amphibolitised, whereas ISD13-06 still contains pyroxenes and granulite facies mineralogy. In addition, the amount of sulphides within ISD13-06 is much greater. This may suggest that hydration of these rocks also mobilises, in part, the sulphides as well. This may be an important mechanism to remove and concentrate sulphides and/or metals for deposition elsewhere.

The mafic zones of the survey areas are of interest because they contain scapolite of among the highest SO_3 contents, making them a prime source of sulphur. Additionally, they contain sulphides of different metals, including Cu, Ni and Fe, in quantities greater than that of the

anorthosites and their veins. Further assessment as to whether the mafic areas of these rocks can be a metal source for mineralised zones was completed, see Section 4.2.5.1.

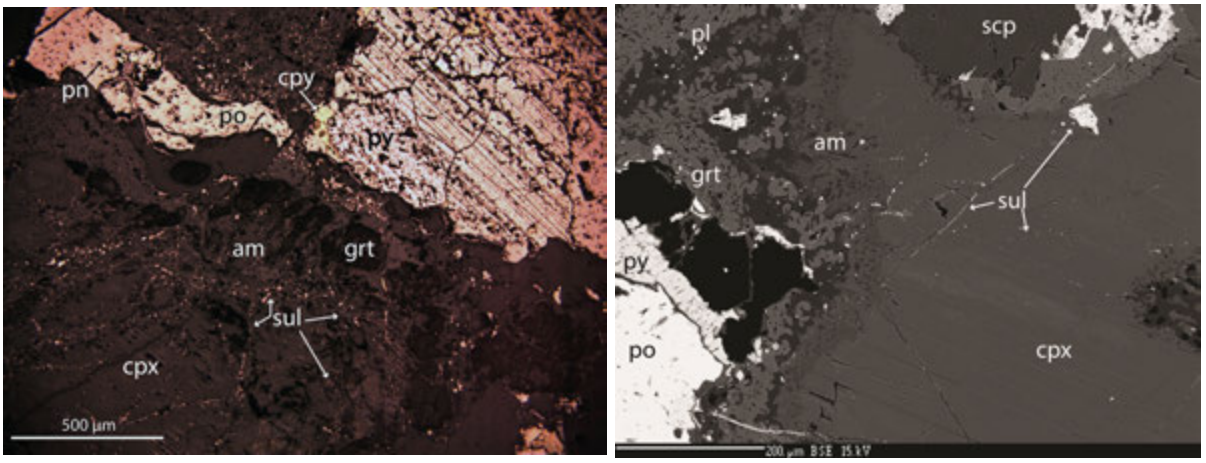

(A) (B)

FIGURE 4.23: (A) Reflected light image showing the extent of sulphidisation of the mafic section in ISD13-06. Note the four sulphide types (py, po, pn and cpy) and the extent to which the px and am have been invaded by sulphide blebs, forming linear aggregates. (B) A BSE image of ISD13-06 showing in detail the alteration of cpx to amphibole, garnet and plagioclase. Also note the fracture infill of sulphides, and their increased abundance in the altered am and grt zone.

4.1.6 Sulphides

Sulphides can be found in nearly all samples of the survey areas. In Figures 4.24a, 4.24b, 4.24c and 4.24d, examples of sulphide occurrences are shown. Figure 4.24a shows a typical example of the sulphides found at the Hilland Mine site, from the waste rock pile. The waste rock is from the fault-associated quartz veins, containing primarily quartz and few epidote gangue minerals, with pyrite and chalcopyrite. Pore space is large and interconnected. The ore minerals are anhedral, irregular shaped chalcopyrite grains, though pyrite is the most abundant sulphide found in the sample. Pyrite varies from irregular to euhedral grain shape, from cm-sized cubes to μm blebs. As reported by Sandvik (1977), the only economic metal extracted was Cu. Other metal sulphides were not detected in this sample, though may be present to a small degree as fine-grained crystals. The cpy and py appear to be separated into general, small zones, as indicated in Fig. 4.24a, where the cpy exists above the dashed line, and pyrite is below. This may be indication as to how fluid moved through the rock.

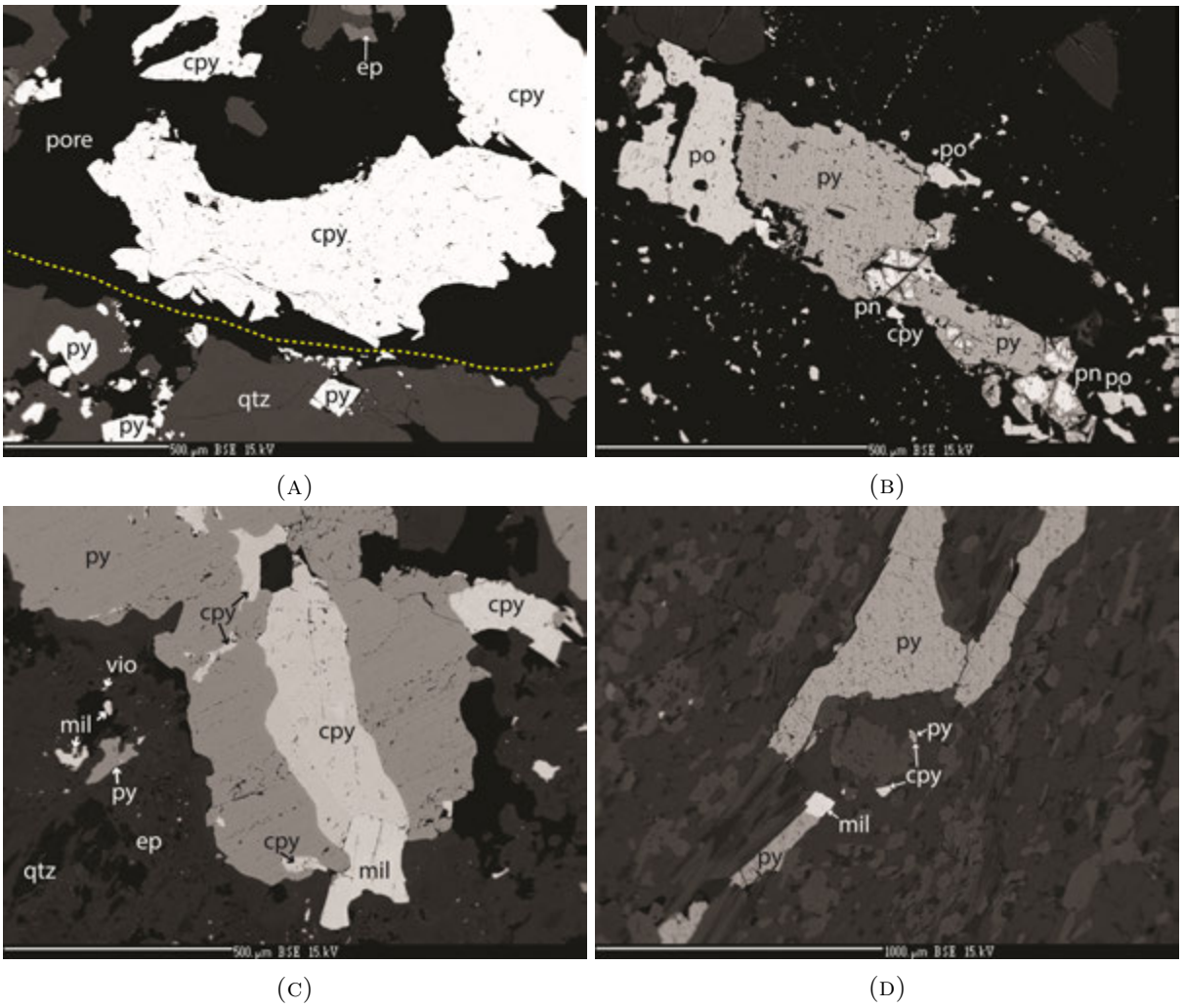

(A) (B)

(C) (D)

FIGURE 4.24: BSE images of sulphides within the study areas. (A) HIL13-03, a sample from the Hilland Mine waste rock pile. The sulphides are mainly pyrite below the dashed line, and cpy, above the line. Note the high amount of pore space. (B) The semi-continuous sulphide veinlet in ISD13-07A2. Pentlandite (pn) and violarite (vio) are the main Ni-bearing minerals. Also present are chalcopyrite, pyrite and pyrrhotite. (C) Pyrite with intergrown millerite (mil), and cpy in HIL13-18B. Sulphides such as mil, vio and py, also form blebs in the epidote, which are a possibly former scp grains. (D) Py and mil form elongated grains in the main fabric direction of HIL13-17. Also present is cpy.

ISD13-07A2 is an example of sulphides found in a granulite facies rock. Figure 4.24b shows a portion of the sulphide veinlet within the main pyroxene-scapolite vein of the sample. Iron sulphide occurrence includes both pyrrhotite and pyrite. At least two different types of Ni-sulphides exist in the forms of pentlandite (pn), and violarite. Pentlandite appears to be breaking down to an iron oxide, seen as rims around the pn crystals in the figure. In addition to the main sulphide vein, there are other sulphides forming blebs within the surrounding epidote and amphibole. These blebs contain similar metals, and form radiating lineations that follow the cleavage of former pyroxene crystals. This is also shown in Figure 4.10a. The sulphides make up 1-5% of

the vein, and are associated with the bordering silvialite and pyroxene, which are the major constituents of the main vein.

HIL13-18B, seen in Figure 4.24c, is an example of sulphides within the non-sheared scapolite front, composed mainly of silvialite. Sulphide compositions are similar to those in ISD13-07A2, with millerite (mil), violarite (vio), chalcopyrite and pyrite all present. Grain shapes are irregular and non-directional. Sulphides are associated with former pyroxenes that are now amphibole, epidote and calcite. The distinct pyroxene exsolution lamellae can still be seen; however, no detectable pyroxene chemistry remains. The sulphide blebs are numerous in this example, and can be seen in the figure around the epidote (ep) label.

HIL13-17 shows the sulphides found in a sheared amphibolite sample (see Fig. 4.24d). As with the other samples, there are two main types of sulphides: the main, larger assemblages, which in this sample, have a directional habit that is coincident with the fabric of the rock. The second kind of sulphides are the blebs, which are rounded to euhedral, showing no preferred orientation. These are dominantly iron sulphides and occur within the scapolite-rich areas in the vein. Additional figures showing the sulphides of HIL13-17 are Figs. 4.16a, 4.16b and on page 101.

4.2 Mineral Chemistry

Tables of the results of EMP analyses for each given mineral appear in the Appendix. For each analysis, a chemical formula was calculated using a Microsoft Excel spreadsheet and site assignments were made for each cation given stoichiometric constraints. All oxide weight percent analyses were recalculated to mole amounts based on number of atoms in the oxide formula, divided by the respective atomic weights for both oxygens and cations. Cations and oxygens were then normalised to a determined number associated with the formula of the mineral calculated. The following explains what specific parameters were used for each of the mineral groups calculated.

Scapolite was calculated based on the general formula $W_4Z_{12}O_{24}A$, where Z (or T, tetrahedral site) is Si, Al and Fe^{3+}; W is Ca, Na, K plus minimal Mg and Mn. The A site is occupied by S, Cl and C. Carbon is calculated, not measured, based on the simple formula C = 100 - (S+Cl). This assumes only these three anions occupy this site, though possible minor amounts

of F and OH may also be present. Meionite and marialite contents are calculated using Me = Ca/(Ca+Na) and Ma = Na/(Ca+Na).

For plagioclase, the cations are calculated to 5, and oxygen to 8 atoms. Iron is considered divalent. Plagioclase is fit to the generalised formula: $A_1T_2Si_2O_8$, where T is either Si or Al; and A is Na, Ca or K. End members of albite, anorthite and orthoclase are calculated based on Ab = Na/(Na+Ca+K), An = Ca/(Na+Ca+K) and Or = K/(Na+Ca+K).

Epidote is calculated to a general formula of $A_2B_1Al_2(TO_4)(Si_2O_7)O(OH)$, where T is remaining Si or Al; B is remaining Al, Ti, Mn, Mg, and Fe^{3+}; and A is predominantly Ca ± K, Na or remaining Mg. Epidote is normalised to 12.5 oxygens per formula and all the iron is converted to Fe^{3+}.

Garnet is calculated to 8 cations and 12 oxygens, accounting for charge balance with conversion to ferric iron where necessary. The generic formula used for garnet is $M2_3M1_2T_3O_{12}$, where T consists of Si and Al; M1 is Ti, Al, Cr and Fe^{3+}; and M2 is the remaining Fe^{3+}, Fe^{2+}, Mn, Mg and Ca. The end members were found using the ratio of Fe/(Fe+Mg+Ca+Mn) for almandine, Mg/(Fe+Mg+Ca+Mn) for pyrope, (Al/(Al+Ti+Cr+Fe^{3+})) * (Ca/(Fe+Mg+Ca+Mn)) for grossular, Mn/(Fe+Mg+Ca+Mn) for spessartine and (Fe^{3+}/(Al+Ti+Cr+Fe^{3+})) * (Ca/(Fe+Mg+Ca+Mn)) for andradite.

For pyroxene, the cations are calculated to 5 cations and 8 oxygens, accounting for charge balance with conversion to ferric iron. The general formula for pyroxene is $M1_1M2_1T_2O_6$, where T is filled by Si and Al; M2 is filled with remaining Al, Ti, Cr, Fe^{3+}, Fe^{2+}, Mg and M1 with remaining Fe^{2+} and Mg (ratios between these were kept the same for both M1 and M2 sites), Mn, Ca and Na. End member calculations are: wollastonite, Ca/(Ca+Mg+Fe), enstatite, Mg/(Ca+Mg+Fe) and ferrosilite, Fe/(Ca+Mg+Fe).

Amphiboles are calculated using the general formula $A_{0-1}B_2C_5T_8O_{22}(OH)_2$. The T site is occupied by Si and Al; the C site by Ti, Fe^{3+}, Cr, Mg, Fe^{2+}, ±Mn. The B site is filled by the remaining Fe^{2+} and Mn, with Ca and Na; and A is filled with any remaining Na and K. The formulas are calculated based on, originally, 23 oxygens and all ferrous iron. The amount of ferric iron in the amphibole is calculated by finding a normalisation factor based on minimum and maximum ferric iron estimates. Minimum ferric estimates are based on either: Si = 8, sum of all cations = 16, all iron is ferrous, or the sum of cations excluding Na and K is 16. The maximum ferric iron estimates are based on calculating either: the sum of all cations excluding

K = 15, the sum of cations excluding Ca, Na and K = 13, all iron is ferrous, or the sum of Si+Al = 8. The normalisation factor, calculated between the lowest ferric and the highest ferrous estimates, is used.

The micas, muscovite, biotite and chlorite, are all calculated using the generalised formulas $A_1M_2T_4O_{10}(OH)_2$, $A_1M_3T_4O_{10}(OH)_2$ and $M_5AlT_4O_{10}(OH)_8$, respectively, using similar techniques and order of filling the tetrahedral and octahedral sites as with the minerals above.

4.2.1 Scapolite

Tables A.2 and A.3, of the Appendix, show the composition of the scapolites analysed with the EMP in weight percent oxides for the Hilland and Isdal areas, respectively. Sixty-eight scapolite analyses were taken, all presented in Appendix A. The stoichiometry was determined using similar techniques as Evans et al. (1969); Teertstra et al. (1999); Teertstra and Sherriff (1997) and Teertstra and Sherriff (1996), normalising the Si + Al to 12. However, this left the sum of the M sites to be over 4 for many samples. Consequently, all iron is considered to also take up space in the T site as Fe^{3+} such that (Si + Al + Fe^{3+}) = 12. This technique assumes all tetrahedral (T) sites are completely filled exclusively by Si, Al and Fe^{3+}. For samples in this survey, this may also not be completely suitable as the M sites still fill to over four atoms; thus other elements may occupy space in the tetrahedral sites.

Figure 4.25a shows a plot of the meionite percent of all samples analysed plotted against the sulphur atoms per formula unit (apfu). The definition of Me used here is Ca/(Ca+Na). All samples from all localities, save one, are of over 50% Me. Most fall within the range of 60-70% Me, which is mizzonitic, according to the classification of Evans et al. (1969). Only one sample from Espetveit is marialite, although the same thin section also contains a scapolite with high sulphur content, possibly formed from different fluid generations at different metamorphic grade.

Figure 4.25a indicates three groups of Ca scapolites exist, based on their S content: those with a sulphur number above 0.55 (over 4.8 oxide weight % SO_3), between 0.27 and 0.47 apfu, and very low sulphur meionites of between 0.12 and 0.18 S apfu. Those above 0.5 are considered high-sulphur scapolites or silvialite. Those below 0.5 are assumed to be CO_3-rich meionites, as all samples in the area are Cl deficient (see Figure 4.25b).

Figure 4.25a also highlights the wide range of sulphur compositions available to a scapolite of Ca compositions between 60-70% Me. There is no correlation between S content and Ca content

within this data set. Even those samples with the highest and lowest S contents, 0.86 and 0.12 apfu, are formed with a similar Ca content, Me 64-66%. Sulphur is not a good indicator of Ca content, and vice versa. This may be due to the distinct lack of Na rich scapolite within the dataset, which limits the possibility for coupled substitution of Na-Cl with Ca-SO_4. The third species found within the anion site of scapolite, but not measured directly is carbon, as CO_3^{2-}. Carbon content is estimated as C = 100-(S+Cl). Therefore, without an increase in Cl content, it is the C content that changes in direct response to changes in S. To keep charge balance, CO_3^{2-}, or other similarly charged ionic compounds, are taken into the scapolite structure. Therefore, CO_3^{2-} and SO_4^{2-} are interchangeable over a Ca content of Me_{60-70} within this dataset. This matched decrease and increase in carbon and sulphur species is also noted by Moecher et al. (1992) in scapolites of an anorthosite in the Grenville Province of eastern Canada. They also remarked on a decrease in sulphur content toward the margin of the anorthosite complex, which indicates an influx of carbon rich fluid its the margins. This may be seen here, at a smaller scale, with regard to the scapolite front rock of HIL13-18, which increases in CO_2 content toward the anorthosite boundary.

The scapolites found in granulite facies rocks, such as in thin sections HIL13-16, HIL13-19, ISD13-01A, ISD13-07A2 and 44-91A are all Ca rich, with Me contents between 62 and 73%. The sulphur contents of the anion site are, by definition silvialite, as they are all above 0.5 apfu, with the exception of HIL13-19 and ISD13-01A. Other examples of silvialites are found in mafic portions of the rocks ISD13-04, ISD13-06 and AK72-98II; and the scapolite 'front' rock, HIL13-18, away from the plagioclase-scapolite boundary. Sheared rocks and those considered to have formed at amphibolite facies conditions generally have lower sulphur contents, under 4.0 wt.% SO_3, or 0.45 apfu.

A comparison of the Na and Cl contents; however, shows a slight positive correlation (Figure 4.25b) in cases where the Cl content is over 0.5 wt.%. An increase in Na content is followed with an increase in Cl content. Chlorine may be the sole univalent anion to substitute in the marialite structure, although F and OH are also known to exist within the A site, and may account for the imperfect correlation between Na and Cl. Those with both the highest Na and Cl weight percentages correspond to the amphibolitised samples, with the exception of HIL13-07B, represented by squares in the figure. Significant, however, is that only one of the samples has over 0.82 wt.% Cl, making this a very poor Cl pool of scapolite samples. Also of note is the lowest Na_2O wt.% samples are from the most well preserved granulite facies rock, HIL13-19.

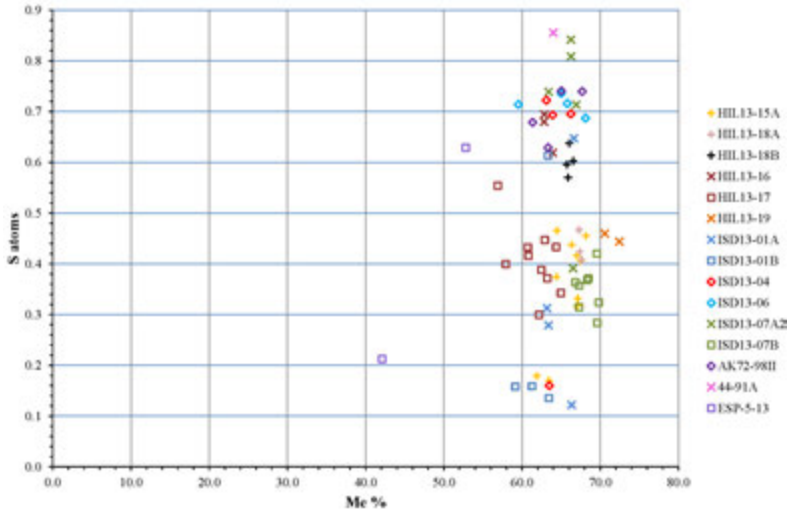

(A)

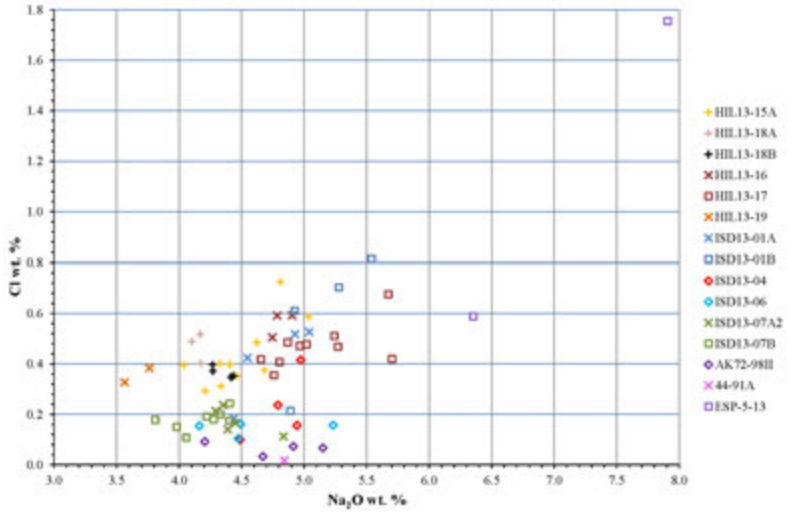

(B)

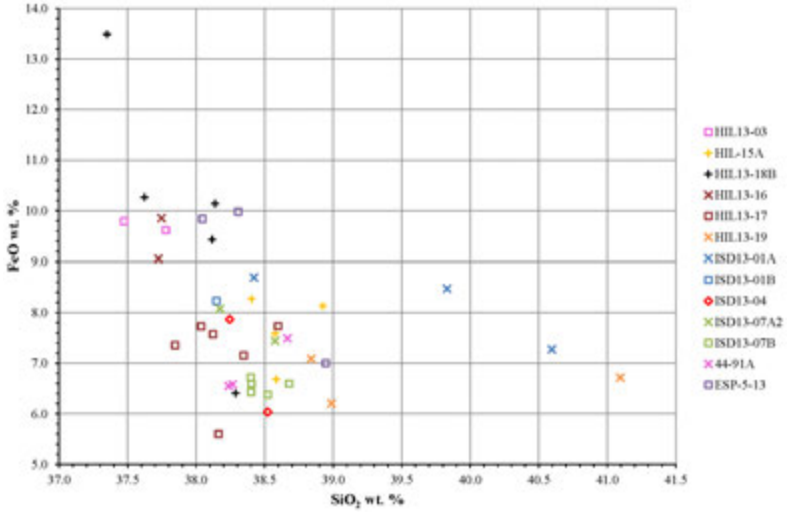

(C)

FIGURE 4.25: (A) Scapolite Me% versus sulphur atoms per formula unit. The main scapolite 'front' rocks are represented with '+', the granulites 'X', the amphibolites '□' and the mafics '◇'. Granulite and amphibolite pairs from the same vein are represented by an 'X' and '□' of the same colour, respectively. (B) Scapolite Na_2O versus Cl wt.%. (C) EMP analyses of epidotes plotted as FeO weight percent versus SiO_2 wt.%. The iron in epidote is trivalent.

In summary, granulite facies anorthosites contain high, yet variable SO_3 contents. Pyroxene-bearing veins, jotunite and scapolite rich veins and metasomatic zones at granulite facies conditions, generally contain silvialite, or scapolite with the highest contents of sulphur. Amphibolite facies rocks have the lowest sulphur concentrations, are classified as meionites, and contain CO_3^{2-} as their primary volatile species. Na-bearing marialites, with Cl in the anion site, are not present in this area.

4.2.2 Epidote

The composition of epidote was analysed for changes in iron content. The Fe content within the structure of epidote is trivalent, and this may be important for the formation of sulphides from scapolite through redox reactions. Epidote frequently occurs with both scapolite and sulphides, oxidised and reduced minerals. In total, 37 epidotes were analysed and the results are presented in Table A.5, of the Appendix, and in Figure 4.25c. Of note, are the elevated levels of Fe in the silvialite 'front' rock, HIL13-18, and the silvialite bearing vein of HIL13-16. Other elevated Fe^{3+} concentrations are found at both mine sites: from the Hilland Mine slag pile, HIL13-03, and from the Espetveit Mine area, ESP-5-13. Note that Figure 4.25c is plotting FeO wt.%, but all Fe was converted to Fe_2O_3 for mineral stoichiometry calculations in the Appendix.

4.2.3 Feldspar

Thirty-one plagioclase grains were analysed, the results of which are shown in Table A.4, and plotted in Figure 4.26a. The most original granulite lilac anorthosite, HIL13-19, contains the highest anorthite percentage, An_{45}; labradorite. This is similar to the granulite plagioclase, An_{50}, reported by Mukai et al. (2014) in the Isdal area. The An composition is defined as (Ca/Ca+Na+K). An anomalous reading that contains over Or_{11} at bytownite composition plagioclase, An_{77}, exists at the boundary between normal labradorite plagioclase and scapolite, seen in Figure 4.5b. The anomalous amount of potassium may be the result of the reaction between the plagioclase, which contains exsolutions Kspr, and the scapolite; or it may not be a plagioclase, structurally.

In the case that plagioclase and scapolite are formed side by side, the scapolite contains the higher Ca content; ie, the Me% of scp is higher than the An number of plagioclase. Comparing Figures 4.25a and 4.26a shows that the Me content of scapolite is consistently high at Me_{60-70},

whereas the plagioclase contents varies through a range of oligoclase to labradorite compositions, An_{22} to An_{58}.

The most Na rich plagioclase is found in the mafic samples ISD13-04 and -06, but also with the hydrated and sheared anorthositic samples of HIL13-15, -17 and ISD13-07B. These all have an An content of less than 35%. The mafic samples have the most sodic plagioclase and contain scapolite with the highest S content; however, the sheared and amphibolitised anorthosites, which also contain sodic plagioclase, have the lowest sulphur-scapolite concentrations. This demonstrates no correlation between An number of plagioclase and S content of scapolite.

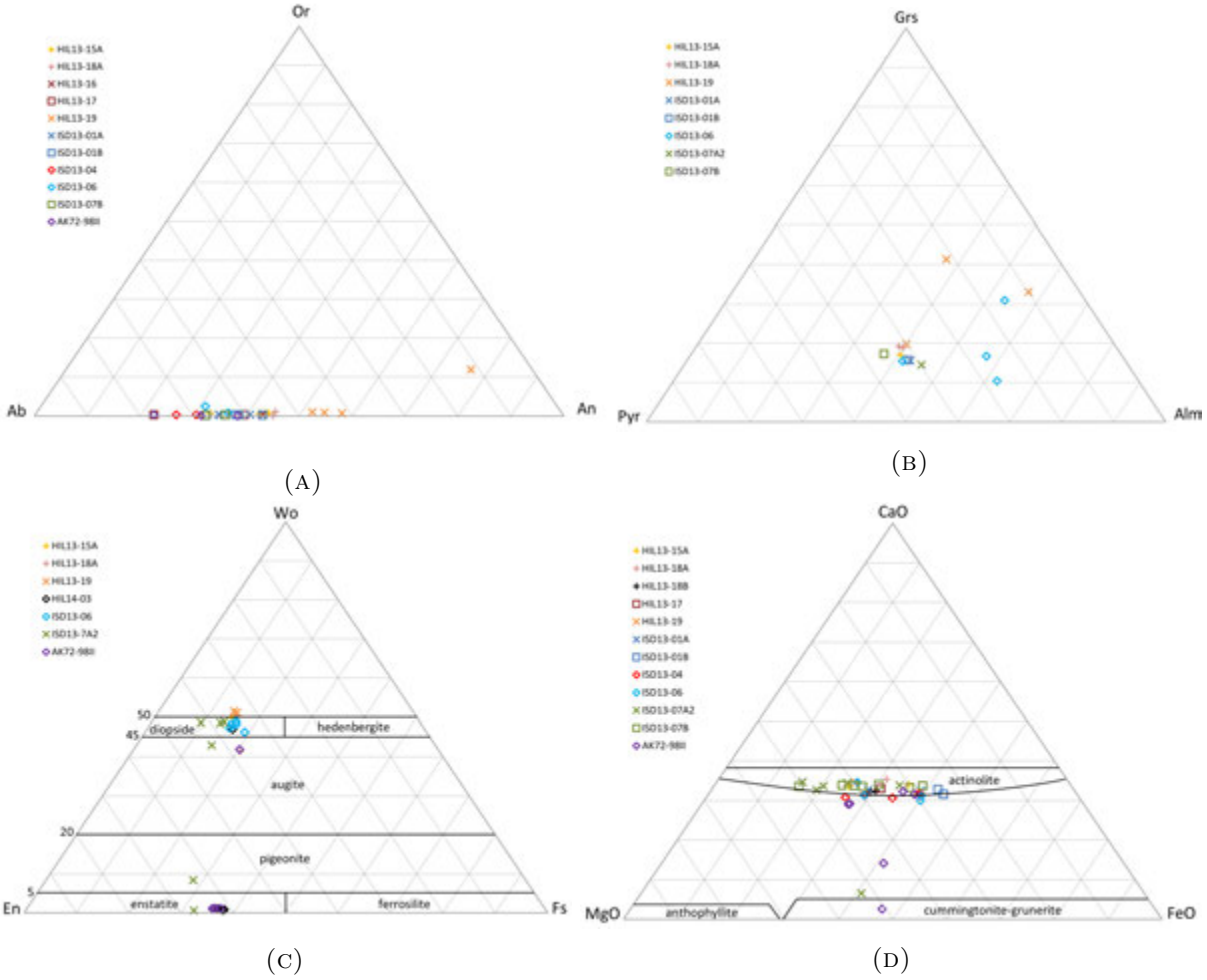

FIGURE 4.26: (A) Ternary plot of the end members An, Ab and Or of analysed plagioclase. See Figure 4.25a for an explanation of the legend, relevant to all ternary plots. (B) Ternary plot of the end-members almandine (Alm), pyrope (Pyr) and grossular (Grs) for analysed garnets. (C) Ternary plot of end-members wollastonite (Wo), enstatite (En) and ferrosilite (Fs) of analysed pyroxenes, normalised to 100. Fields typical of end-member minerals are presented for simple reference, but may not represent real stoichiometry of the analysed samples, as they are of more complex mineralogy. (D) Ternary plot of analysed amphiboles with CaO, MgO and FeO end-members normalised to 100. See text for explanation.

4.2.4 Garnet

Results of the garnet analyses are shown in Table A.6 of the Appendix, and plotted in Figure 4.26b. In total, 14 samples were analysed. In the figure, a cluster of garnets with similar Mg:Fe:Ca ratios exist, with a nearly 50:50 ratio between Mg and Fe (pyrope-almandine). A typical composition is $Alm_{39}Pyr_{40}Grs_{18}$, which is similar to the garnet coronas at Isdal, $Alm_{31}Pyr_{51.2}Grs_{17.3}$, reported by Mukai et al. (2014); and the granulite facies garnet, $Alm_{29}Pyr_{51}Grs_{18}$, reported by Kühn (2002). These garnets represent the original granulite facies compositions and have preserved their chemical compositions, despite changing conditions that have altered other minerals in the rock. Garnet compositions have remained the same over a variety of metamorphic grades and rock compositions. Supporting this, most garnets in this study have the same composition as those in the granulite facies sample, HIL13-19, despite their observed range of amphibolite retrogression.

The outliers in the data are found in HIL13-19 and ISD13-06 as new growths and reaction rims around unstable clinopyroxenes (see Figs. 4.5a and 4.23b). All of the newly formed garnets have considerably less Mg content, higher Fe content and in the case of the granulitic anorthosite, HIL13-19, are also more grossular (Ca) in content.

4.2.5 Pyroxene

The results of pyroxene analyses are shown in Table A.7 of Appendix A, and as a ternary diagram in Figure 4.26c. In total, 26 pyroxenes were analysed. The figure shows that most of the pyroxenes are cpx and lie within the diopside field of the ternary diagram, containing mostly Mg and Ca in their M1 sites. However, since the Ca, Fe and Mg contents were normalised to 100 in the diagram, Na, Ti and other elements were not included. Given the more complex mineralogy of the samples analysed, the mineral field in the ternary plots are for reference only. Alumina content is high in the clinopyroxenes of the anorthosites, ranging from 5.29 to 11.49 wt.% Al_2O_3. HIL13-15, -18 and -19 all have between 1.6 and 1.76 wt.% TiO_2 in their structures. These same samples, plus ISD13-06, have between 1.04 and 2.17 wt.% Na_2O contents. These are low concentrations, but enough to move the content of the minerals away from the pure Mg, Fe and Ca end-members presented in the diagram of Figure 4.26c.

The pyroxenes best represented in the ternary diagram for composition, are the orthopyroxenes of AK72-98II, HIL14-03 and ISD13-07A2. They contain relatively low Ca and Al, and plot

within the enstatite field. One sample from ISD13-07A2 also falls in the pigeonite field and can be seen in Figure 4.10b.

Note that no pyroxenes were identified or analysed in the hydrated, amphibolitised rocks. Pseudomorphs of pyroxenes were found in some samples such as HIL13-15 and -18, but they have been completely replaced by amphibole, chlorite, epidote, sulphides and calcite.

4.2.5.1 Trace elements

Eight pyroxenes were selected for trace element study of Ni and Cu concentrations across each crystal face. This was done to test for possible metal sources for the sulphides that formed from scapolite. The mangerite rock, HIL14-03; most original granulite, HIL13-19; scapolite 'front' rock, HIL13-18A; and sheared mafic vein, AK72-98II, were chosen for study. Each grain was surveyed along a line at points a consistent distance apart. In order to test how the concentrations varied laterally across an opx crystal face, a line was selected crossing the entirety of the crystal; and in one case, extends into the amphibole rim outside the grain. A complete list of all pyroxenes analysed, their Ni and Cu contents, and respective standard deviations (STD), are presented in Table A.8 of the Appendix.

Profiles across Lines 4, 2 and 3 of two orthopyroxenes, and a low-Ca amphibole reaction rim from sample AK72-98II are presented in Figures 4.27a, 4.27c and 4.27d, respectively. Figure 4.27b shows the locations of Lines 2 and 3; the location of Line 4 is shown on Figure 4.13c.

The profile across Line 4 shows loss of Ni at the edges of the opx crystal, into the surrounding amphibole (Figure 4.27a). The main grain has an average of 820 ppm, which decreases at the edges of the line to 700 ppm and 560 ppm in the surrounding amphibole, creating a convex shape in the figure. All Ni measurements had a detection limit of approximately 58 ppm. The main loss of Ni occurs in the amphibole, while the main opx grain has a generally consistent Ni concentration throughout. Cu concentrations of this and all pyroxenes in AK72-98II are negligible.

The profile across the opx of Line 2 shows a relatively consistent Ni concentration of approximately 850 ppm. The short profile of Line 3, across the low Ca-amphibole rim, shows a decrease in Ni concentration away from the opx grain and toward the high Ca-amphibole (am2). The amphibole (am1) that replaces the opx, has a significantly lower Ni concentration, which continues to decrease away from the opx boundary. Line 3 is shown next to Line 2 (Figures 4.27d

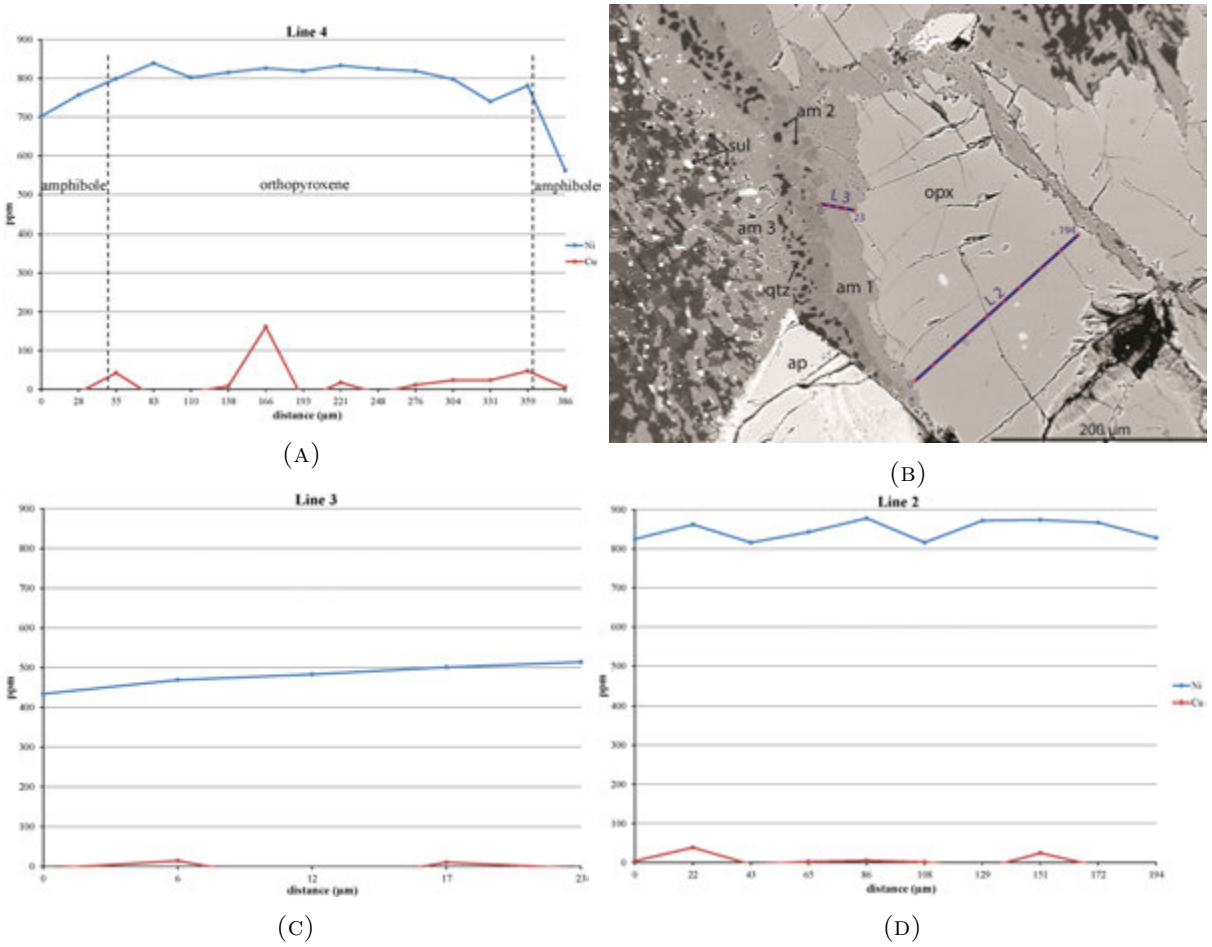

FIGURE 4.27: (A) Profile across an opx grain in AK72-98II, labelled Line 4 (L4) in Figure 4.13c. The line traversed the opx grain and amphibole rims on either side. A convex shaped Ni concentration profile can be seen as the Ni content decreases into am1, on either side of the opx grain. Points lying in the amphibole rim are indicated, and are of decreased Ni content, 100-200 ppm less than the adjacent opx grain. (B) An opx crystal with concentric amphibole reaction rims of am1, am2 and am3. This is similar to the opx reactions described in Figure 4.13c. Blue lines with red dots indicate the position of analysed points on the trace element survey lines. Numbers indicate distance of start and end of lines, given in microns. Line 2 (L2) was completed across the opx, Line 3 (L3) is across the low Ca-amphibole reaction rim (am1). See Fig. 4.13a for location in thin section. (C) Profile of Ni and Cu concentrations along the amphibole labelled L3 in (B). Note concentrations of Ni increase toward the opx grain. This profile has been scaled proportionally with that in (D) in order to directly compare their Ni concentration changes in ppm. (D) Profile of Ni (blue) and Cu (red) concentrations in ppm, along an opx grain labelled L2 in (B).

and 4.27c, respectively) at the same scale, to easily compare Ni concentration changes. If the entire area occupied by the low Ca-amphibole was originally opx, this represents a significant loss of Ni in the rock, from 850 to 430 ppm, and introduction of metals into the surrounding system. See the Discussion Section 5.3, for more details.

Line profiles across clinopyroxenes were completed for HIL13-19, that also show very low concentrations of Cu; however, Ni concentrations average approximately 360 ppm. The cpx crystals of AK72-98II average 530 ppm Ni across Lines 5 and 6, without significant loss of Ni at the crystal edges.

The clinopyroxene of HIL13-18A also has statistically insignificant concentrations of Cu, and averaged 140 ppm Ni across the grain (Figure 4.28a). This pyroxene is found near the scp-pl boundary in the scapolite of sample HIL13-18A. Farther away from the front, the pyroxenes are completely broken down, so any Ni and Cu within their structure would have been released, and used possibly as metals in any precipitating sulphides. The general lack of Cu in most of the surveyed pyroxene grains reveals the source of significant Cu mineralisation to be elsewhere.

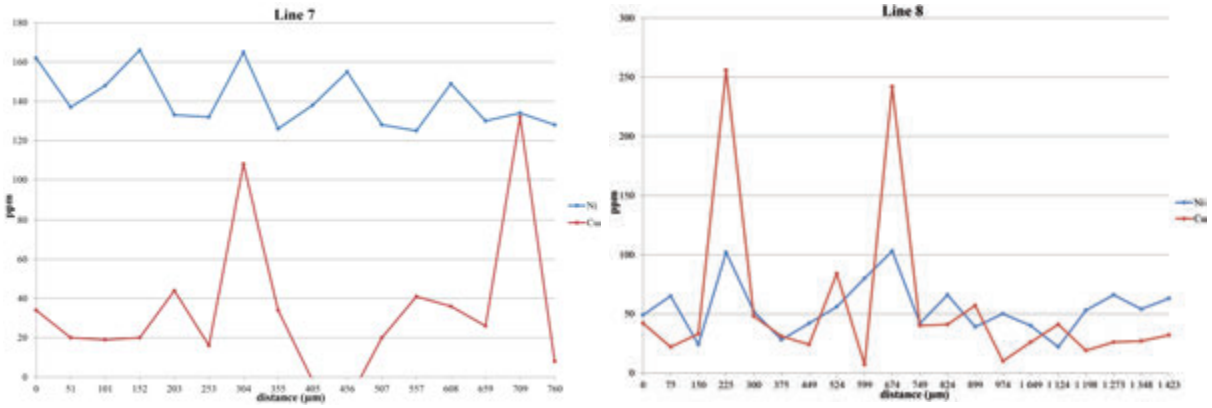

(A) (B)

FIGURE 4.28: (A) Profile across a cpx grain in the scapolite front rock HIL13-18A. The average Ni content is 140 ppm, whereas the Cu content is variable, with mostly insignificant concentrations across the line. (B) A traverse across an opx crystal in mangerite, HIL14-03 shows low level average concentrations of both Ni and Cu.

Another opx analysed in the mangerite, HIL14-03, contains almost no Ni or Cu within detection limits (Figure 4.28b). As it is unusual for a mafic opx-pl rich mangerite to contain so few metals in the silicate phases, these metals may have partitioned preferentially into an immiscible sulphide phase during crystallisation. Nickel and Cu have strong affinity for a sulphide melt over the silicates which, depending of MgO content, can be between 100 and 200 times larger for Ni, and 250 times larger for Cu (Naldrett, 1989). Barnes and Francis (1995) found the partition

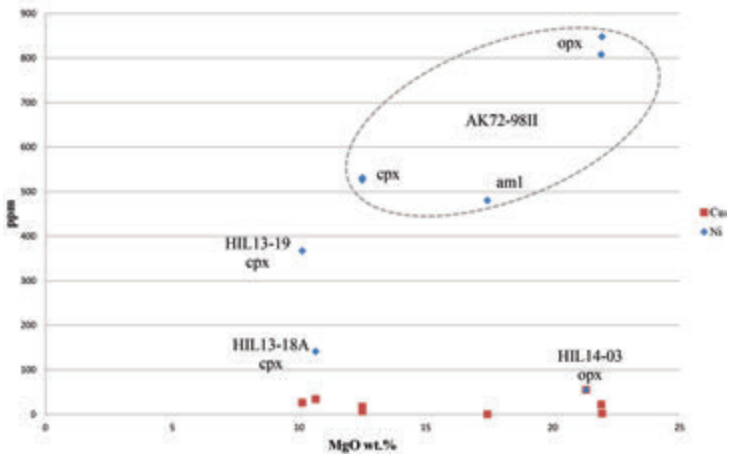

FIGURE 4.29: MgO wt.% versus concentrations of Ni and Cu in ppm. There is not a strong correlation between MgO and Ni concentrations in pyroxenes. Note especially the low Ni in HIL14-03 compared with AK72-II, despite similar MgO concentrations.

coefficient for Ni and Cu in a gabbro-norite is 511 and 2000, respectively. Weak correlations between Ni and MgO exist comparing the high 21 wt.% MgO of the opx in AK72-98II, to cpx in the same and other thin sections. Figure 4.29 demonstrates that the opx in HIL13-04 has very low concentrations of Ni despite similar amounts of MgO. Thus HIL14-03 stands out as discrepancy in this data set.

4.2.6 Amphibole

A total of 40 amphibole grains were analysed with the EMP, and the results are presented in Table A.9 of the Appendix. A ternary plot of the data shows the ratios of CaO:MgO:FeO in the samples (Figure 4.26d). The positions of actinolite, anthophyllite and cummingtonite-grunerite are also shown on this plot, but do not accurately represent the stoichiometric formulas of these amphiboles. The amphiboles in the survey areas contain significant quantities of Al_2O_3 and Na_2O. The mineral fields within the plot should, therefore, be used for reference only. The amphiboles of ISD13-07, both -A and -B, are the most Mg-rich in the sample population, whereas the ISD13-01 samples are the most Fe rich. Compared to the pyroxenes, the amphiboles have a higher Fe:Mg ratio, in general.

Evident from Figure 4.26d, three samples are, or approximating, low to no Ca amphiboles of near actinolite-cummingtonite composition. All three of these (from samples AK72-98II and ISD13-07A2) are identified texturally as reaction rims around unstable orthopyroxene grains (see Figs. 4.10b and 4.13c). In the case of AK72-98II, at least three different types of amphiboles are

identified forming concentric rings around opx grains, in contact with broken down scapolite. The am in contact with the opx is the low Ca, low Al type (am1 in Fig. 4.13c), outwards from am1 is am2, containing larger quantities of Ca, and occurring together with quartz. The third amphibole (am3) is of high-Al, low-Si and high-Ca. Presumably the silica lost in the formation of am3 led to the precipitation of quartz, which is always present between am2 and am3 in the reaction rims.

4.2.7 Sulphides

In the Appendix, lists of the analysed compositions of pyrites (Table A.11) and all other sulphides (Table A.12) are presented. Nickel concentrations in the pyrites are elevated, with HIL13-07A containing nearly 1 wt.% Ni, and another sample having 0.65 wt.% Co. The vein in HIL13-07A contains a diverse selection of minerals, including pyrite, chalcopyrite, pyrrhotite, pentlandite and violarite.

4.3 Stable isotopes

A limited number of scapolite and sulphide samples were prepared and sent to a stable isotope laboratory in the Institut für Geologie und Mineralogie of Westfälische Universität, Münster, Germany for analysis. Table 4.1 shows the results of the analyses of these samples. Two samples, KRA03-04 and HOS12-13, were collected by H. Austrheim from Krakeneset and Hosanger, both areas of high-sulphur scapolite. HOS12-13 was collected near Hosanger on Osterøy island, east of the study area in the Bergen Arcs, at the Hosanger Nickel Mine.

The sulphide (predominantly pyrite) samples of the Hilland Mine waste rock sample, HIL13-03, show slightly negative values irrespective of size, from -0.5 to -0.7 ‰ δ^{34}S. These slightly negative values differ from the pyrite samples collected away from the mine, both in the Hilland and Isdal areas.

The sulphide samples in the Hilland area were collected from within the silvialite zone of HIL13-18, and a retrogressed eclogite near the Hilland Fault. Sulphides from the Isdal area are from both the granulite and amphibole areas along the vein of samples ISD13-07A and -07B. The S-isotope values for all of these samples are similar, varying from +0.3 to +2.1‰ δ^{34}S. The

TABLE 4.1: A list of samples analysed for sulphur isotopes, in ‰, with errors when reported. Samples KRA03-04 and HOS12-13 were provided by H. Austrheim for comparison.

Sample	Mineral	Size (µm)	δ^{34}S (‰)	error
HIL13-03	sulphide	pre-crush	-0.7	0.03
HIL13-03	sulphide	>250	-0.5	0.05
HIL13-03	sulphide	63-250	-0.6	0.1
HIL13-13	sulphide	<63	0.3	
HIL13-13	sulphide	<63	1.1	
HIL13-18	sulphide	<63	0.6	
HIL13-18	sulphide	<63	0.9	
HIL13-18	scapolite	<63	4.7	0.1
ISD13-7A	pyrite	<63	1.9	
ISD13-7A	pyrite	<63	2.1	
ISD13-7B	pyrite	<63	0.2	
ISD13-7B	pyrite	<63	0.7	
ISD13-7B	pyrite	<63	1.0	
ISD13-7B	pyrite	<63	1.9	
KRA03-04	scapolite		4.3	0.03
HOS12-13	scapolite		3.5	0.17

similarity in values of these samples may represent a kind of homogenisation or similar fluid source.

No samples of scapolite were found within the Hilland Mine slag, and only one sample of scapolite was analysed for stable sulphur isotopes for this project. The silvialite scapolite sample from HIL13-18 is +4.7‰ δ^{34}S. This is slightly higher than those found at Krakeneset and in the Ni mine, approximately 20 kilometres to the southeast of the Hilland Mine area, which are +4.3 and +3.5‰ δ^{34}S, respectively. The differences in these values suggests that the source of sulphur in the mine site rocks and the sulphide rocks may be different.

Chapter 5

Discussion

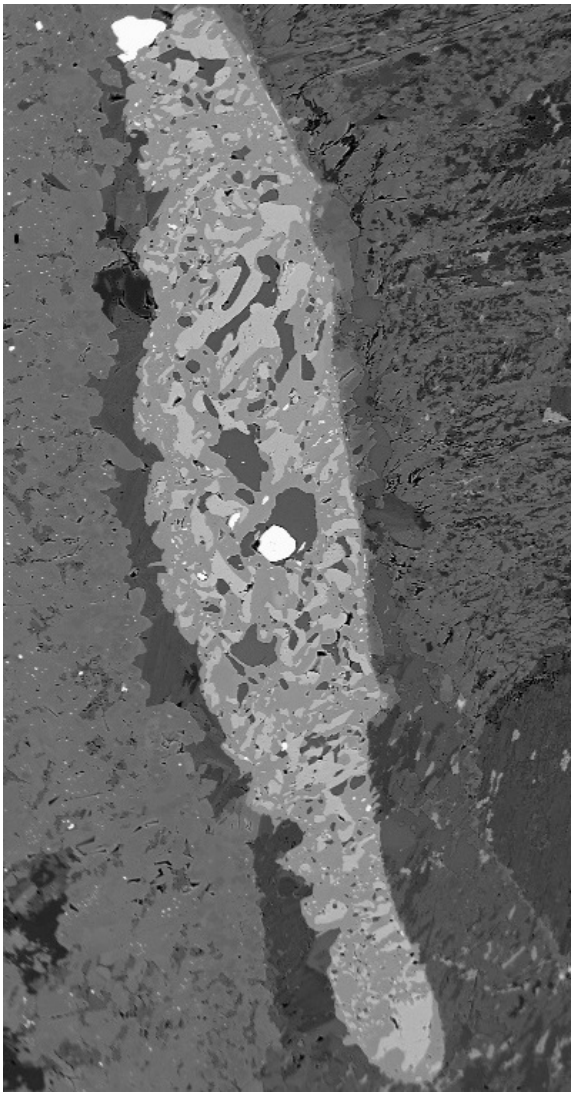

5.1 Compositional changes in scapolite

High S-scapolite, or silvialite, is found in granulite facies anorthosites and jotunites in the Lindås Nappe. Within the anorthosites, scapolite occurs in two forms: as intergranular crystals in the plagioclase-rich groundmass, and within pyroxene-bearing veins or larger zones of metasomatic scapolite.

The intergranular crystals are part of the original granulite mineralogy, and contain high SO_3 values, between 3-4 wt.%. Scapolite within the veins and metasomatic 'fronts' cut the granulite fabric of garnet coronas and banding. They formed after the original granulite mineralogy, but still at granulite conditions. This is evidenced by the anhydrous anorthosite mineralogy associated with the veins, as well as by their high-S scapolite compositions. This is because silvialite is only stable at granulite conditions. These veins, together with the scapolite of the jotunites, contain the highest sulphur contents in the study area, between 4.8 and 7.2 wt.% SO_3. The difference in the S contents in vein/metasomatic scapolites suggests a different fluid may have formed them, in comparison to the scapolites of the original granulite mineralogy.

A third kind of scapolite is found within the study areas: meionite, a CO_3 rich scapolite formed at amphibolite conditions. Sulphur bearing scapolite becomes unstable at conditions below, for example, 900°C at 1.5 GPa, which releases sulphur. The SO_3 within the structure is replaced, nearly one-for-one, with CO_3. These meionites contain SO_3 contents between 1.0 and 3.2 wt.%. They occur in veins of amphibolite mineral assemblages, that may or may not have been sheared. The veins and wallrock amphibolites also are hydrated and sheared to variable degrees. Generally, the more sheared the rock is, the more porous the veins, and the more carbon rich the scapolite. This may be the result of increased fluid flow, allowing for more enhanced mineral reactions, and introduction and removal of more ion species.

There are two main types of reactions involving scapolite:

1 - Formation of scapolite through replacement: This occurs in contact with plagioclase, whereby the entirety of the original anorthosite mineralogy is replaced by scapolite along a distinct metasomatic front. This occurs at large and small scales, either along the cm-scale scp-px veins, formed at granulite conditions, or along larger scapolite 'fronts' in which most of the rock is replaced with sulphur-rich scapolite.

Replacement reactions creating scapolite include:

Eq. 4.1:

$pl + SO_2 + CO_2 \longrightarrow (S)scp$

This reaction occurs within the granulite anorthosites, where high-sulphur fluids infiltrate and replace plagioclase and granulite mineralogy, metasomatically. A reaction of meionite replacing silvialite is:

Eq. 4.13:

$(S)scp + Fe + CO_2 + H_2O \longrightarrow (C)scp + ep + sul$

This reaction happens either at lower grade conditions, and/or with fluids exhibiting high carbon dioxide fugacity. This reaction converts S-scp to C-scp.

2 - Breakdown of scapolite through replacement and recrystallisation: This occurs where the scapolite is broken down, either completely, or partially, to a new composition. The scapolite is either replaced with sulphide bleb-bearing epidote or amphibole.

Some of these reactions include:

Eq. 4.5

$(S)scp + H_2O \longrightarrow ep + pl + sul + CO_2$

Eq. 4.6

$(S)scp + Fe + H_2O \longrightarrow ep + pl + sul$

Eq. 4.7

$(S)scp + H_2O + Fe + Ca \longrightarrow ep + sul + Si + Na + CO_2$

Eq. 4.8

$(S)scp + H_2O + Fe + Mg \longrightarrow am4 + ep + sul + CO_2$

Eq. 4.16

$(S)scp + am2 + qtz \longrightarrow pl + am3 + sul + CO_2$

Carbon dioxide released in these reactions may form calcite, given the availability of Ca and the stability of calcite at the given conditions. Several occurrences of calcite were found within the samples. This may also be reflective of high fugacity of CO_2, also needed to form meionitic scapolite at amphibolite conditions.

Marialite, Na and Cl rich scapolite, is absent in this area. Cl-sources may have been absent, or conditions unfavourable in forming Na or Cl rich scapolites. The resulted in the formation of primarily CO_3 and SO_4-rich meionites and silvialites. This differs from the high Cl-amphiboles

and scapolite identified in eclogite facies anorthosites on Holsnøy by Kühn (2002). Comparatively, the scapolites, amphiboles and apatites are Cl deficient on Radøy and Isdal. This may be important given evidence the eclogites on Holsnøy and the amphibolites on Radøy formed contemporaneously, and represent only a pressure gradient (Roffeis et al., 2012). This suggests a separate and distinct fluid, or fluids, rich in CO_2, H_2O and SO_2 formed the anorthosites on Radøy, in close proximity to the Cl-rich fluids of the eclogites on Holsnøy.

5.1.1 Reactions involving related minerals

Granulite to amphibolite facies reactions also affect other minerals within the assemblages. These reactions play a role in the formation and replacement of scapolite and subsequent sulphidisation.

Plagioclase becomes more Ab-rich as it is amphibolitised. Ca is introduced to the system, Na is removed. Without addition of Na, the volume of rock decreases accordingly. Ca is released to form Ca-scapolite, with a more andesitic, from originally labradorite, plagioclase.

Eq. 4.2:

(Ca)pl + H_2 O $\longrightarrow$ (Na)pl + czo

Garnet breaks down from its granulite composition, releasing Fe into the system, as per Eq. 4.10:

grt + Ca + Na + H_2O $\longrightarrow$ am4 + Fe

Epidote may be a key mineral in the formation of sulphides from scapolite. It stores all Fe as ferric iron and occurs with scapolite where the sulphide blebs are observed. Within the lower grade, sheared veins, such as HIL13-17, meionitic scapolite and numerous sulphide blebs occur with zoned epidote. The iron content increases toward the outside of the grains. The growth of epidote with higher Fe contents may have been conducive to the formation of sulphide minerals in electron exchange reactions.

There are few examples of pristine pyroxenes, as many have been completely replaced by amphibole and epidote. Reactions demonstrating the hydration of pyroxene to amphibole are:

Eq. 4.9

$cpx + H_2O + Fe + Mg \longrightarrow am2 + qtz + Ca$

Eq. 4.11

$pgt + H_2O + Ca \longrightarrow am + Fe$

Eq. 4.12

$cpx + H_2O + Al \longrightarrow am + qtz + Ca$

Amphibole contains sulphide blebs from the breakdown of scapolite. Charge balance of these amphiboles show that there is ferric iron within the their structure (see Table A.9). This increased oxidative state also accounts for needed electrons in redox reactions, reducing sulphate to sulphide.

5.2 Source of sulphides in mineralised zones

There are multiple examples of sulphides occurring together with S-scapolites. Sulphides form clouds of μm-sized rounded blebs, forming halos around edges of scapolite grains. Scapolite grains that are mainly intact, have a few sulphide blebs at their edges, together with epidote. As the breakdown of scapolite progresses, the size of the sulphide reaction halos and the number of blebs increase. Many of these clouds form straight lines through irregular-shaped bounding minerals, also suggesting the sulphides delineate the original grain boundary of the scapolite from which they formed. Given the textural associations of sulphides with scapolites in many samples, there is no doubt there is a connection between the formation of sulphides and the breakdown of scapolite.

Copper- and nickel-bearing sulphides exist within granulite facies rocks, prior to the breakdown of silvialite. Mafic veins in the anorthosites, jotunite dykes and the bordering mangerite all contain sulphide phases within their structure at granulite conditions. This indicates there were reduced sulphur and metals in the granulite system before any sulphur from S-scapolite was released during amphibolite retrogression. Any sulphides found at amphibolite facies conditions may include sulphur from both generations of sulphides. Mobilisation of these sulphides may focus and concentrate them into bodies of economic interest, suggesting that scapolite-derived sulphides can contribute to these mineralisations.

Stable sulphur isotope analyses were performed to assess how scapolite may have contributed to the formation of sulphides. Reactions involving the breakdown of scapolite were also analysed for mass and charge balance. These are described in the next two subsections.

5.2.1 Stable isotope analysis

Small isotopic differences exist between pyrite at the Hilland Mine and those within sulphides in the granulite S-scapolite. Both sulphide samples exhibit δ^{34}S values close to 0‰. The sulphides at Hilland Mine vary between -0.5 to -0.7 ‰, whereas the sulphides found in the scapolite rocks vary +0.3 to +2.1‰. This suggests they both may have mantle derived formation fluids, with the scapolite rocks containing a bit more of a crustal component. This may suggest similar, though different fluids created the mineralisation. They may be from different sources, or the Hilland Mine sulphides may be a mix of a more negative fluid and the fluid that formed the scapolite sulphides.

The fractionation factor between two species, A and B, of sulphur bearing minerals is defined as:

$$\Delta^{34}S = \delta^{34}S_A - \delta^{34}S_B \tag{5.1}$$

The fractionation factor of sulphur isotopes can be related to temperature of formation by the equation:

$$\Delta^{34}S = \frac{A * 10^6}{T^2} \tag{5.2}$$

where A is a constant equal to the slope of straight lines through the origin and T is in Kelvin (Faure and Mensing (2005) and references therein).

The difference in isotopic factors of pyrite and scapolite in this sample is approximately 4‰. If the scapolite and the sulphides within sample HIL13-18 are in equilibrium, they formed at over 900°C, according to data presented by Ohmoto (1972) and Rye and Ohmoto (1974) (see Figure 5.1). This is within the temperatures of granulite facies formation and within the stability field of silvialite. However, their datasets were obtained using different SO_4^{2-} species, and S-scapolite was not used in their calculations. Moreover, another assumption made is the scapolite and sulphide within this sample were in equilibrium. Given the complexity and number of sulphur species involved within this system, the lack of isotope data from this area and the relative lack of geochemical data involving the sulphate in S-scapolite, any results based on these data are inconclusive.

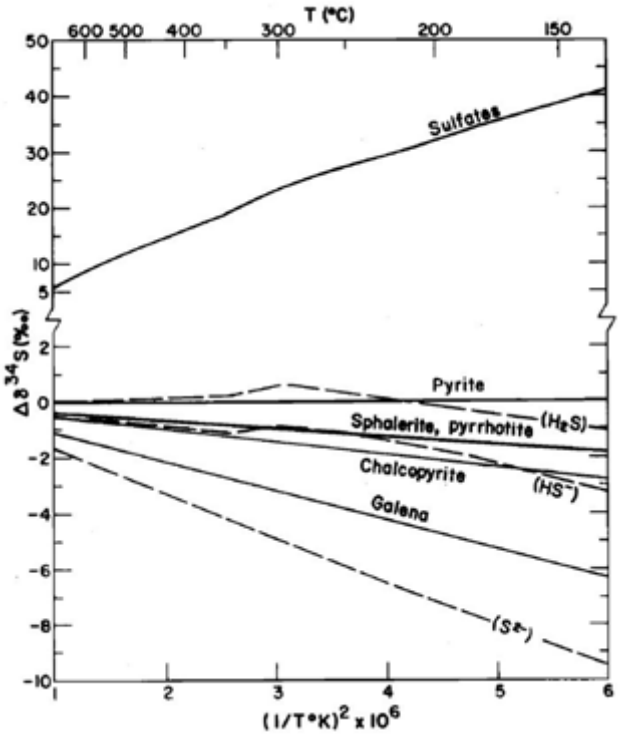

FIGURE 5.1: Sulphur isotope fractionation between sulphur-bearing minerals and species. From Ohmoto (1972).

5.2.2 Analysis of sulphur content and redox potential

Scapolite forming together with sulphides is ubiquitous in the study area. This is somewhat paradoxical as scapolite contains oxidised sulphate species, and sulphides are reduced. A mechanism for reduction of sulphur to form sulphide blebs is introduced. One suggestion is there is a redox reaction, whereby electrons are exchanged from an oxidising mineral, minerals or compound, to compensate for the reduction of sulphur. Both epidote and amphibole contain ferric iron and; therefore, represent oxidised minerals. One or both of these minerals are always present after scapolite has broken down to sulphide blebs. Evaluation of reactions involving both of these minerals is performed to assess if they form with sufficient quantity to be able to reduce the amount of sulphides present. It is clear epidote and amphibole are key to the formation of sulphides, as the presence of sulphide inclusions are limited to, and confined within, epidote and amphibole grain boundaries, after the breakdown of scapolite.

5.2.2.1 Static conditions

During the breakdown of scapolite under static conditions, sulphur amalgamates into blebs of typically 1-5 μm size and precipitates within the boundaries of former scapolite crystals. The result allows easy identification of former scapolite boundaries from the geometry of the present sulphide blebs (see for example Figs. 4.7a, 4.10b, and 4.19b).

An example within a static system is used to determine if S-scp can provide the sulphur needed to form sulphides. In the element-mapped image of sulphur shown in Figure 5.2a, the red portions of the image are used to determine the original size of a scapolite grain before it was partially broken down. The total area inside the red delimited area is considered the original boundary of the scapolite grain. The blue is the remaining scapolite, still in existence. The black area within the grain boundary is epidote that has replaced scapolite.

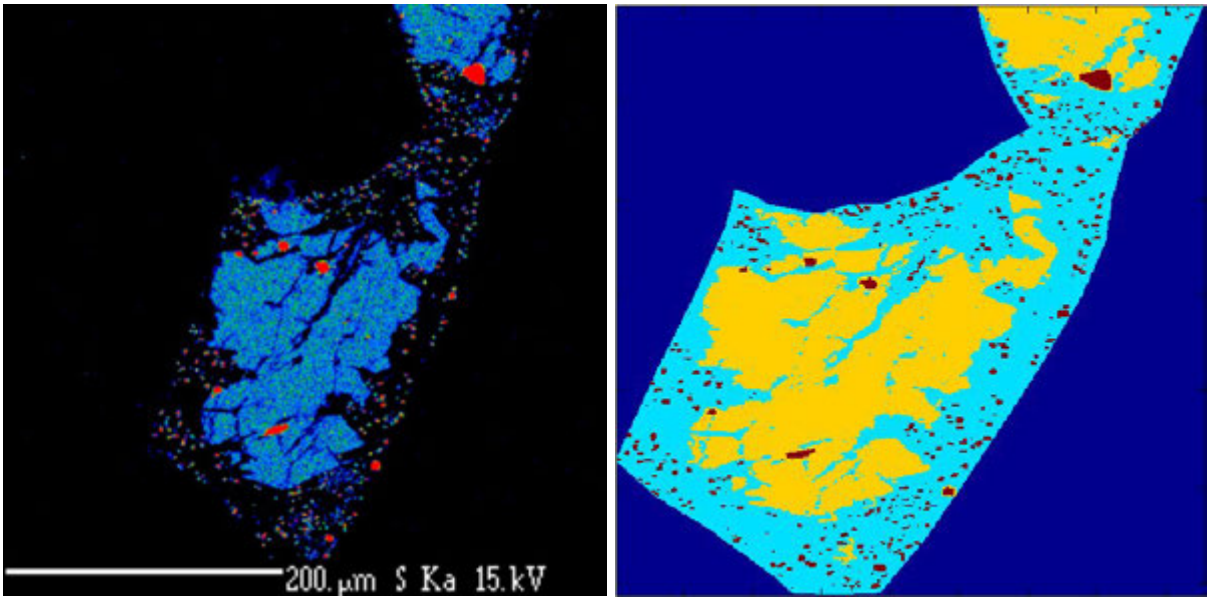

(A) (B)

FIGURE 5.2: (A) Sulphur mapped image from Fig. 4.7b showing the original scapolite grain boundary delimited by the red coloured sulphide blebs. (B) MatLab derived image dividing the old scapolite grain into 3 main areas. The red represents the sulphides, the yellow is present scapolite, and the light blue is the former scapolite, now replaced with epidote. These areas were used to derive respective area percentages for each mineral. The area bounded by the sulphide blebs in the two photos are the same; however, the MatLab image has been distorted during processing.

These three areas were separated based on grey-scale intensity using a MatLab program written by G. Saunders, creating the image in Figure 5.2b. In this image, the sulphides are red, the present scapolite is yellow, and the epidote is light blue. These areas were used to calculate area

percentage inside the grain boundary. EMP analysed compositions were used for the respective minerals in calculating atomic percentages. The original and remaining scapolite are assumed to have the same composition, averaging 3.57 wt.% SO_3. Results show there is 3.5 times more sulphur present in the area of remaining scapolite and sulphides, as there would have been if the area were filled only with the original scapolite.

Possible explanations for the over abundance of sulphur may be one or several of:
1 - There were sulphides present before the breakdown of scapolite. There is more than one mode, the sulphides form in larger clumps as well as the small blebs. Some of these may be sourced from elsewhere.
2 - The original scapolite composition was higher than it is presently. The breakdown of scapolite may be from dissolution and/or loss of SO_3 from the entire structure.
3 - Area estimation using MatLab has overestimated the presence of sulphides
4 - The sulphide compositions may not be entirely pyrite, but less sulphur-rich varieties, such as pyrrhotite or chalcopyrite.

Due to the abundance of sulphur, the Fe^{3+} in the epidote cannot account for all electrons needed to create the present sulphides in a redox reaction. Again, this may be because many of these sulphides were already present, or their presence has been over estimated by the MatLab program. Another mechanism may be found to account for the reduction of these sulphides, which occur together with two oxidised minerals, scapolite and epidote.

5.2.2.2 Shearing conditions

HIL13-17, the sheared amphibolite, contains two types of sulphides: those that are irregular, Ni- and Cu-bearing, semi-connected, elongate aggregates following the main fabric; and the others are rounded, fine grained, containing Fe-dominant sulphide blebs, found in the meionite groundmass. The co-genetic and textural relationships of these sulphides suggest a different provenance. The blebs in the scp groundmass suggest they formed post-shearing, from the both rounded, non-preferentially orientated blebs, and also from the subhedral grain boundaries. Conversely, the elongate aggregates of Ni- and Cu-rich sulphides are formed within the fabric of the rock, suggesting they were there pre- or syn-shearing. In the case of HIL13-17, the processes that breakdown the scapolite to sulphides do not remove sulphur from the system.

Figure 5.3a shows an area within the sheared vein of HIL13-17, in which three main minerals are found: C-scapolite, epidote and pyrite. This image was analysed in order to determine if S-scapolite can provide the sulphur required to form the present sulphides. Moreover, if sulphides are formed through a redox reaction with epidote, the amount of charge in the Fe^{3+} formed from Fe^{2+} of other sources, should account for the +6 to -2 reduction in the sulphur to form sulphides. Using MatLab, the image was split into three areas according to grey-scale intensity, and is shown in Figure 5.3b. The light blue area is scapolite, the yellow areas are epidote and the red areas are pyrite. It was determined the epidote comprises 11.26% of the total area; and pyrite, 0.88%. Average oxide weight percents were measured for each mineral, converted to atomic percents and divided by their respective area percent in the image. For simplicity, the entire area of the image is assumed to have been comprised wholly of S-scapolite prior to breakdown, with an average composition of 5.83 wt.% SO_3, determined from HIL13-16 analyses (see Appendix A, Table A.2).

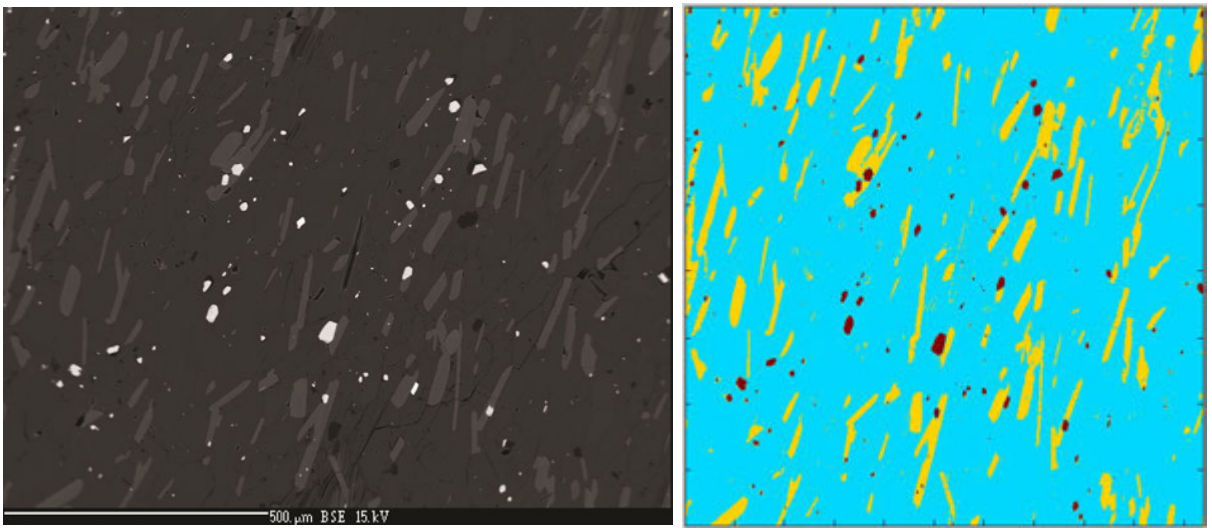

(A) (B)

FIGURE 5.3: (A) Scapolite vein in HIL13-17 showing the predominant mineralogy of the vein: scapolite, dark grey; epidote, light grey; and pyrite, white. (B) MatLab derived image dividing the area into 3 main minerals. The red represents the sulphides, the yellow is epidote, and the light blue is C-scapolite. These areas were used to derive respective area percentages for each mineral. The areas of the two photos are the same; however, the MatLab image has been compressed into a square during processing.

From the calculations, sufficient sulphur is released from the high S-scapolite to form both the new, C-scapolite and pyrite. In the hypothetical S-scp, for every 156 S atoms released during complete breakdown, 85 atoms are required to build the new C-scp and 58 S atoms form the

pyrite. There is an excess of 13 atoms, or 8% of the sulphur in the S-scp, to account for assumptions made for compositions of the present and original mineralogies.

Fe is not abundant within the assumed original mineralogy, S-scapolite. The iron must be introduced to the system, either through breakdown of pyroxenes, garnet or ilmenite. The epidote, composing 11% of the analysed area, contains 27 atoms Fe^{3+} for 58 atoms sulphur in pyrite. This is insufficient to reduce all required sulphur to sulphides. Another reducing reaction that may take place, is the S-scp to C-scp transformation, whereby sulphate is replaced by carbonate in the anion sites. Carbon in this structure is +4 valency, two less than replaced sulphur, which it replaces one-to-one during scapolite breakdown.

Assuming all the sulphides are pyrite, a reduction of S to only -1 is required, as the partial covalent bonding of pyrite, sulphur appears to have a valency of -1. To reduce all the sulphur in the present sulphides from +6 to -1, accounting for an increase in carbonate within the replaced scapolite, 7.7% more Fe^{3+} from epidote is needed.

Reduction of sulphate to sulphides, thus, requires either another source or another mechanism. Some of the pyrite was likely formed from sulphides already present in the granulite system. Also, less sulphur rich sulphides are present in this section, if chalcopyrite were the sole sulphide, only 4.1% more Fe^{3+} in epidote would be needed.

Additionally, there are zones within this rock that are more epidote-rich, such as in the more mafic areas, associated with biotite and amphibole. These areas of increased epidote content may account for the electrons needed to complete the redox reactions.

5.2.3 Role of deformation and fluids

Although it is clear that sulphides are produced through the breakdown of scapolite at amphibolite facies conditions, it is not always clear whether those sulphides remain within the rock during shearing. Examples have been found where sulphides formed from both scapolite breakdown, and from original granulite facies mineralogy, are still present in a sheared rock (HIL13-17). However, other examples show nearly no sulphur present, in sulphides or within scapolite in other highly sheared and hydrated rocks (HIL13-01B).

Whether sulphides continue to be present within an amphibolite after hydration may be a function of proximity to shear zones and fluid infiltration, leading to expedited reactions and

movement of element species. Conduits, such as fractures, grain boundaries, or faults that are common in the Bergen Arcs region, can act to concentrate and funnel fluids. If these conduits pass through areas of granulite rich in silvialite, they may contribute to removal and concentration of constituents that create mineralised occurrences.

Increased porosity may also be a factor in degree of fluid infiltration. During metasomatic, dissolution-replacement reactions, porosity is increased. This creates space for further fluids to enter and for new minerals to form (Engvik et al., 2008; Putnis, 2002; Putnis and Austrheim, 2010). The degree of metasomatic reactions, and dissolution-precipitation may play a role in the extent of porosity, and thus species introduced and removed from the system.

As seen within the micro-shear zones of HIL13-15 (see Fig. 4.12d), there is a reduction in the amount of sulphur within the recrystallised, reduced grain-size grains of scapolite. The general decrease in sulphur content in scapolite due to lower metamorphic grades, is enhanced through introduction of fluids along shears, which equilibrates the rock to ambient P, T conditions faster than it would otherwise (Austrheim, 1987; Austrheim and Griffin, 1985). Zones where shears occur in the Bergen Arcs area are known to contain mineral assemblages which more closely reflect the P, T conditions to which they were exposed.

5.3 Source of metals in sulphides

The breakdown of ilmenite and other iron oxides are numerous in the survey area. Fine-grained remnants of ilmenite are found together with titanite and rutile in an area demarked by chains of μm-sized zircons. These zircon 'necklaces' are proposed to delimit the original ilmenite grain area, thereby giving a pre-breakdown grain boundary geometry and size. This area may be used to estimate the amount of iron lost from the original ilmenite grain. The iron from these grains may precipitate iron sulphides in a concurrent process. Possible reactions involving the breakdown of ilmenite are:

Eq. 4.17:

$$FeTiO_3 + SiO_2 + Ca \longrightarrow CaTiSiO_5$$

Eq. 4.18:

$$FeTiO_3 \longrightarrow Fe + TiO_2 + 0.5O_2$$

Ni and Cu contents have been recorded in whole rock chemistry samples by Mattey et al. (1994), Rockow et al. (1997) and Kühn (2002). Nickel contents, averaging approximately 60 ppm, were found in eclogitised rocks, though some are as high as 379 ppm. Additionally, amphibolites contain an average of 110 ppm Ni; and granulites, 105 ppm Ni (Kühn, 2002). Cu values are low for all metamorphic facies of rocks, averaging approximately 10 ppm. The source of the metals, especially Cu, may not be from within the silicates, but from sulphides already within the rocks. The mangerite, HIL14-03, sourced close to the western contact of the anorthosite at Hilland, is rich in Cu and Ni sulphides, despite having low values of Cu and Ni within its opx crystal structure. Sulphides are common in granulite facies rocks that also contain high S-scapolite. It is presumed that sulphide is already present in un-economic concentrations within mafic veins and jotunite bodies within the anorthosite.

Significant amounts of Fe, as well as Cu and Ni sulphides, were found within scapolite rich rocks of the study area. Minor amounts of Co, Ag and Zn were also detected within pyrite and pyrrhotite. Reactions calculated from the breakdown of cpx, opx and garnet all show they release Fe into the system. Moreover, the loss of Fe in the granulite facies ilmenite grains, as they react to form titanite and/or rutile also introduces bivalent Fe into the system as the rocks are amphibolitised.

There appears to be a correlation between the presence of pyroxene in the rock and the amount of Ni or Cu found in the sulphides. Several opx and cpx grains were analysed showing a marked decrease in Ni within opx, in comparison to the amphiboles that formed as reaction products around the original pyroxene (see Section 4.2.5.1). To analyse how much Ni may be lost from opx, Figure 4.13c was divided into two areas. The area encompassing the breakdown of opx to am1, am2 and quartz was analysed using a MatLab code to determine the area that each respective mineral represents. The MatLab generated image is shown in Figure 5.4b, along with the Figure 4.13c BSE image, reproduced here for easier comparison. The opx in this Figure 5.4b is green, am1 is orange, am2 is light blue and quartz is red. There is 54.4% of the opx remaining assuming the original opx boundary included the areas of the current am1, am2 and qtz.

Am1 consists of 31.6% of the image, am2 is 12.0% and qtz is 1.97%. Summing the mineral products (am1, am2, qtz), mass balance is achieved for most oxide species. There is 12.7% less Fe^{2+} in this area than if it was entirely opx, and 6.6% less Mg. Ca content is still low, representing only 0.78%, which is found mostly within the am2 rim. This Ca must be brought

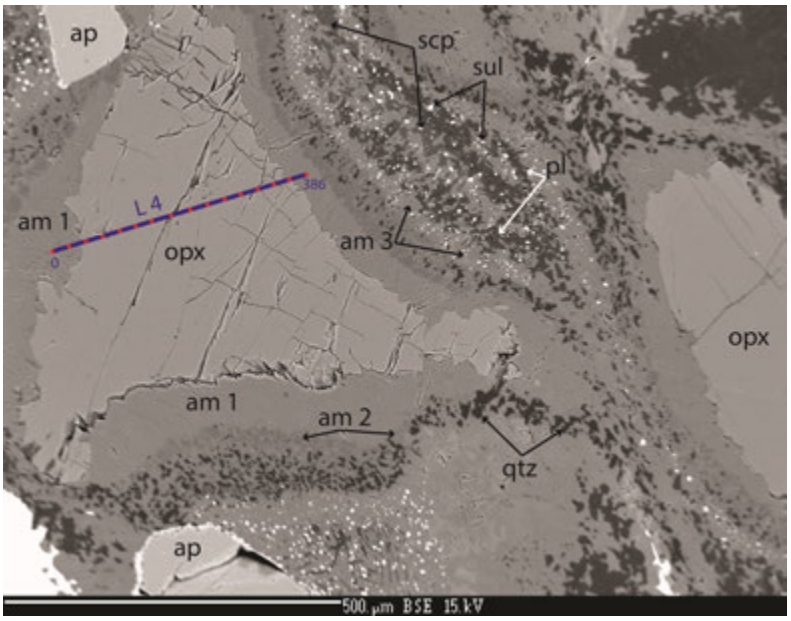

(A)

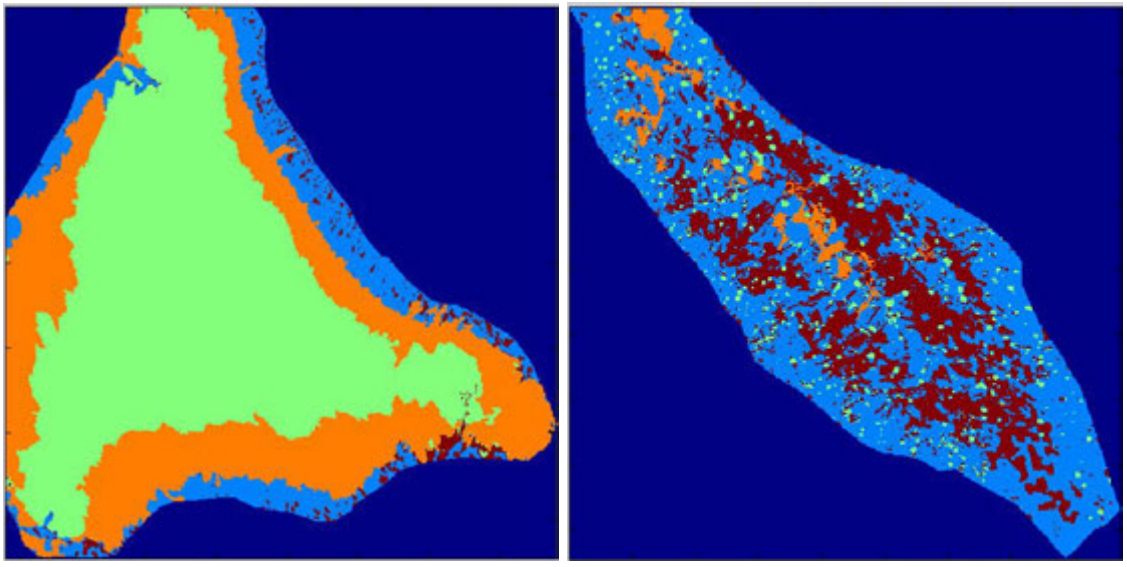

(B) (C)

FIGURE 5.4: (C) BSE image from Figure 4.13c, reproduced for comparison with the following two MatLab derived images. (B) A MatLab generated image from AK72-98II, dividing the area of the opx in (A) and its reaction products am1 and am2 into their respective areas. The opx in this figure is green, am1 is orange, am2 is light blue, and quartz is red. Dark blue is null space. (C) MatLab derived image from the upper border of image (B), identifying scapolite, plagioclase, am3 and sulphides based of grey-scale intensity of the BSE image in (A). Scp is orange, pl is red, am3 is light blue, and sulphides are light green. Null space is dark blue.

in from outside this isolated area. Importantly, however, is the loss of Ni in the opx, as it reacts to form am1 and am2. From Figure 4.27a, the average Ni concentration in the opx is 820 ppm. This decreases into the am1, to 700 and 560 ppm. Line 3 in Figure 4.27c demonstrates the Ni concentration decreases steadily to 430 ppm. Using 820 ppm as an average opx concentration and 560 for am1; also assuming am2 contains nearly no Ni, there is a 24% loss of Ni atoms from the opx grain. This represents 197 mg Ni/kg of opx, where 54% of the original opx remains, as in Figure 5.4a. The jotunite bodies constitute a high percentage of pyroxene in the study area; therefore, they can be a significant source of Ni assuming complete hydration to amphibole. This is seen in sample ISD13-04, where 0% of the original pyroxene remains.

A second analysis was completed using the area delimited by scapolite, plagioclase, am3 and sulphides. The image of these areas are shown in Figure 5.4c. The remaining scapolite is orange, plagioclase red, am3 is light blue and sulphides are light green.

One assumption made is the original scapolite grain boundary is delimited by the ovoid area of scp+pl+am3+sul in Figure 5.4c. There may be a large error with this assumption, as the sample is sheared; and the grain boundary has an elongate shape, unlikely representative of the original scapolite grain geometry. In addition, the sulphide blebs are located within the shear fabric, and it is unlikely they are located where they originally formed. Given these deficiencies, the calculated amount of scapolite remaining within this area is 4.7%. Total area of sulphides is also 4.7%, plagioclase is 30% and am3 is 36%.

Using these estimates, there is 2.1 times more sulphur present in the sulphides than in the original scapolite, which originally had 5.86 wt.% SO_3. This surplus of sulphur may be also, in part, from an overestimation of sulphide quantity by the MatLab program, as mentioned in the preceding section.

Due to the large amount of sulphur in the sulphides, a balanced redox reaction using the ferric iron in the amphibole (am3) cannot be accomplished. Even if the maximum ferric estimate calculated for am3 is used, 40% of the iron in the structure would be Fe^{3+}; not enough electrons are available to form the sulphides.

Regarding Fe, there is a net increase in this section, which can be sourced from the net loss within opx crystal in Figure 5.4b. There is also a decrease in Ca, which is likely taken up by am2 of that section. In general, the loss and gain of elements within one of the sections can be accounted for by the other section. The main exception is sulphur.

5.4 Crustal consequences

Many centimetre-sized veins consist of 20-50 modal % scapolite; additionally, scapolite has been formed metasomatically, through complete replacement of plagioclase in some anorthosites. If the Bergen Arcs are similar to other granulite terranes in equivalent sulphide abundance, granulites may form a significant global sulphur reservoir. Caquineau (2012) has estimated the total sulphur found in each of the atmosphere, biosphere, hydrosphere and lithosphere. From this, he found the sulphur in scapolite comprises approximately 25% of the sulphur cycle. Scapolite, is then a very important mineral, as such a large percentage of global sulphur uptake and release, is a consequence of its stability within the lower crust.

Carbon is also a large constituent of these lower crustal scapolites. In the absence of Cl and other anions, CO_3 replaces equally the SO_4 lost in the lower crust granulites. Consequently, scapolite breakdown plays an equally important role in the carbon cycle, as it represents both a carbon source and a carbon sink.

Unusually high conductivities of the lower crust have been recorded (Edwards et al., 1981; Haak and Hutton, 1986), and have not been sufficiently explained. Granulite, a rock formed under lower crustal conditions, is considered anhydrous, and not a source of water that may be a cause of these higher conductivities. However, if S-scapolite within the granulite becomes unstable, it may lead to the formation of sulphides in quantities sufficient enough to change the conductivity of the lower crust. Localised shears leading to fluid infiltration may eclogitise or amphibolitise granulites enough to create conductive conduits, enhanced by the presence of scapolite-sourced sulphides.

Chapter 6

Conclusions

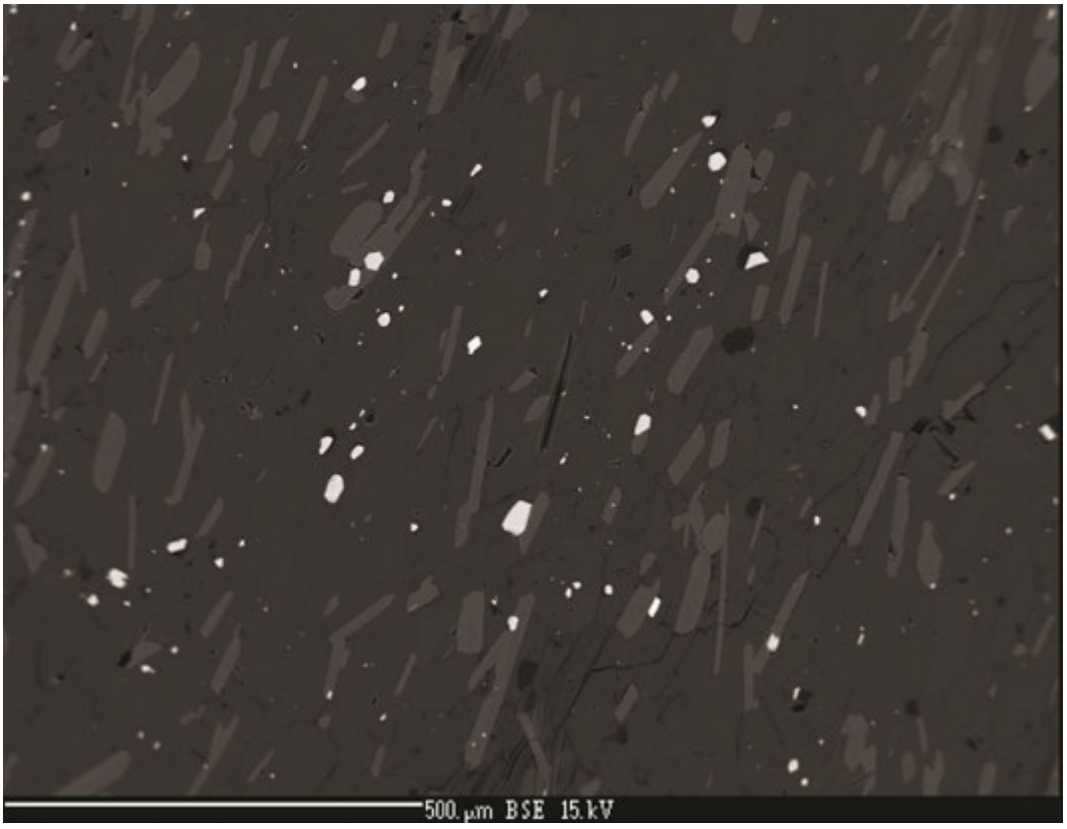

Three main types of scapolite are found within the anorthosite complex of the Lindås Nappe.
1) S-scapolite in granulite facies anorthosite groundmass, with approximately 3.8 wt.% SO_3.
2) granulite facies, high S-scapolite with over 4.8 wt.% SO_3, found in veins and as metasomatic reaction products.
3) amphibolite facies C-scapolite, with less than 3.7% SO_3.

All are high Ca end-members of 60-70% Me. Sulphur content in scapolite cannot be predicted based on Ca:Na ratio (Me%). Carbonate and sulphate are exchanged within the scapolite structure without a coupled exchange between Na and Ca.

Iron, copper and nickel sulphides are found within both granulite and amphibolite anorthosites containing scapolite.

High S-scapolite is formed at granulite conditions through a metasomatic reaction with plagioclase:
pl+ SO_2 + $CO_2 \longrightarrow$ S-scap

S-scapolite loses sulphur from its structure when it equilibrates to amphibolite facies P, T conditions, forming sulphides of μm-sized 'clouds' to larger aggregates of 10-50 μm-sized blebs.

Scapolite also breaks down both under static conditions and during deformation through P and T decrease, and introduction of fluids.

S-scapolite derived sulphides form within and around either epidote or amphibole grains. Epidote and amphibole contain ferric (Fe^{3+}) iron, which is key in redox reactions involving the reduction of sulphate to sulphides through oxidation of Fe^{2+}. A typical reaction of the breakdown of scapolite to sulphides is:
S-scp + H_2O + $CO_2 \longrightarrow$ ep + sul

Fe^{2+} is liberated to the reacting scapolite during amphibolitisation through the hydration of either garnet or pyroxene. Additionally, ilmenite releases Fe^{2+} during breakdown to rutile.

Nickel is released from orthopyroxene during hydration to amphibole, providing one possible source for Ni in the scapolite-derived sulphides.

Intense shearing and/or hydration can mobilise most sulphides, both original and scapolite-derived, leaving a sulphur depleted amphibolite anorthosite. These sulphides may be deposited in areas, like the Hilland-Espetveit fault zone, with sufficient concentration to contribute to an economic occurrence.

Chapter 7

Future Work

Further studies that can be done to supplement data and results presented in this thesis:

More robust stable isotope studies, including oxygen, carbon and sulphide can better constrain the sources of fluids within shear zones, and the relationships between the granulite facies scapolites, in both the metasomatic fronts and groundmass, compared to the amphibolitised scapolites.

Re-Os dating of sulphides within the Espetveit and Hilland mine site rocks, and in the sulphide and scapolite rich wallrocks can better define the temporal relationships between these sulphides, and the regional faults associated with the mineralisation.

More detailed mapping of scapolite-rich rocks can be performed to obtain a more systematic view on how the scapolite and related sulphidisation changes across fault zones.

Other known ore deposits can be re-examined where scapolite is present in the wallrocks. Detailed analysis on textural, isotopic and compositional changes regarding sulphur, carbon and chlorine can be conducted to better assess the relationship between scapolite, sulphides and carbonates.

Conductivity or resistivity studies across zones where sulphide blebs have formed from scapolite can be performed to asses if conductivity of lower crustal rocks changes as a result of scapolite instability; and whether this can contribute to known lower crustal conductivity anomalies.

Appendix A

Collected samples and EMP data

TABLE A.1: A list of all hand samples taken for this study. The X and Y columns give the location of the samples in UTM coordinates, WGS 83, Zone 32V. The X, Y and Elevation columns are in metres and were taken with a ± 5 metre accuracy. Analyses for each sample are indicated as ts - thin section, EMP - electron microprobe and si - stable isotope.

Sample	X	Y	Elevation	Analysis	Description
ISD13-01A	295131	6719378	61	ts	corona garnet AN with scp vein
ISD13-01B	295131	6719378	61	ts	hydrated AN with vein
ISD13-02	295079	6719417	57		granulite AN, white plagioclase
ISD13-03	295160	6719379	62		jotunite rock
ISD13-04	295155	6719374	60	ts, EMP	altered jotunite with sulphides
ISD13-05A	295155	6719374	60		pyrite cube
ISD13-05B	295155	6719374	60		jotunite w. carb, qtz, Fe-Ti ox and sul cavity fill
ISD13-05C	295155	6719374	60		jotunite w. carb, qtz, Fe-Ti ox and sul cavity fill
ISD13-06	295177	6719322	51	ts, EMP	sulphide rich mafic pod within garnet AN
ISD13-07A	295144	6719417	62	ts, EMP, si	granulite AN with scp vein
ISD13-07B	295144	6719417	62	ts, EMP, si	amphibolite AN with scp vein
ISD13-08	295224	6719375	30	ts	sulphide rich mafic pod within AN
HIL13-01	292175	6721680	52	ts	mine wallrock, bleached, white AN
HIL13-02	292161	6721669	53		hydrated garnet corona AN
HIL13-03	292161	6721669	53	ts, EMP, si	qtz vein sulphide ore slag
HIL13-04	292158	6721670	50		hydrated coronitic grt AN, fractured
HIL13-05	292157	6721669	55	ts	corona-less sheared AN
HIL13-06	292157	6721669	55		amphibole flower on wall rock AN
HIL13-07	292170	6721725			original AN from mine area
HIL13-08	292170	6721725		ts	mafic bands with garnets, px in original AN
HIL13-09	292163	6721675			fault breccia
HIL13-10	292234	6721634			fault gouge breccia
HIL13-11	292234	6721634		ts	sulphides and carbonate in wallrock
HIL13-12	292218	6721623	11	ts	quartz breccia with sulphides
HIL13-13	292137	6721488	12	ts, EMP, si	retrograded eclogite AN
HIL13-14	292153	6721503	24		sulphides in quartz-rich AN
HIL13-15	292444	6721834		ts, EMP	scapolite front
HIL13-16	292425	6721855		ts, EMP	vein through lilac AN
HIL13-17	292425	6721855		ts, EMP	vein through sheared hydrated AN
HIL13-18	292425	6721855		ts, EMP, si	scapolite front
HIL13-19	292425	6721855		ts, EMP	most lilac AN sample found
HIL13-20	292323	6721899	18		PST in grt-rich mafic granulite
HIL13-21	292285	6721996		ts	lilac AN with scp vein
HIL13-22A	292034	6722193		ts	granulite grt in lilac AN

continued on next page...

...continued from previous page

Sample	X	Y	Elevation	Analysis	Description
HIL13-22B	292034	6722193		ts	hydrated grt coronas
HIL13-22C	292034	6722193		ts	vein in hydrated AN
HIL13-22D	292034	6722193		ts	sulphides in hydrated rock
HIL14-01	292351	6722102	53		cataclasite, AN with no foliation
HIL14-02	292333	6722000	63		non-sheared calaclasite
HIL14-03	291358	6722602	89	ts	norite-type mafic
HIL14-04	292226	6721642	18	ts	wallrock protolith at Hilland
HIL14-05	292159	6721673	52		Hilland wallrock
HIL14-06	292199	6721692	72		massive hydrated AN
HIL14-07	292151	6721716	83	ts	An granulite without corona garnets
ESP13-01	291557	6720515			ore slag, qtz and sulphides
ESP13-02	291426	6720256			ore slag, qtz and sulphides
ESP14-01	290257	6721499	43	ts	mafic pl + px + grt + ep
ESP14-02	291636	6720423	16	ts	Fe-Ti rich with mafic and felsic blebs
ESP14-03	291650	6720409	20	ts	mica and ilmenite rich mafic vein?
KJE14-1A	285633	6731224	57		dark greasy pl, possible scp, porphyroblastic grt
KJE14-1B	285633	6731224	57		like KJE14-1A, transitional, foliated, light and dark zones
KJE14-1C	285633	6731224	57		like KJE14-1A, sheared, grt is reacted
KJE14-02	285542	6731809	10		pink Kspr banding with dark bands cut by PST, mafic
KJE14-03A	285439	6731780	24	ts	fault rock with PST, less altered
KJE14-03B	285439	6731780	24	ts	altered pink fault rock with more wiggly PST
KJE14-03C	285439	6731780	24	ts	most original rock, mafic, straight foliation
KJE14-03D	285439	6731780	24		small sample with PST
MAN14-01	283649	6729854	45		fault rock in mangerite, PST and pink feldspar alteration
NON14-01				ts	nickel ore wall rock from Brattlien mine adit
NON14-02				ts	ore rock from slag pile near road at Brattlien mine

TABLE A.2: Scapolite EMP analyses from granulite and amphibolite samples from Hilland and Espetveit. Values are presented in oxide weight percent. Scapolite is normalised to T = Si+Al+Fe^{3+}. C (calculated) = 100-(S+Cl), Me = Ca/(Ca+Na), Ma = Na/(Ca+Na)

Sample	HIL13-15A										HIL13-18A			HIL13-18B			
number	26	27	28	29	30	31	32	42	43	44	40	43	46	30	34	35	36
	in shear	out	in shear	out	in shear	out	wall	wall	front	front		front			front		
SiO_2	47.15	46.97	47.17	47.31	47.39	46.89	46.72	48.73	48.00	47.01	46.85	46.54	46.81	46.93	47.27	47.05	46.28
Al_2O_3	26.18	25.88	25.43	26.42	25.58	25.81	26.36	25.43	26.03	25.88	25.59	26.25	26.24	25.41	25.43	25.65	25.40
Cr_2O_3	0.01	0.00	0.00	0.00	0.00	0.00	0.01	0.00	0.02	0.00							
FeO	0.03	0.01	0.05	0.03	0.07	0.11	0.00	0.22	0.03	0.10	0.03	0.03	0.04	0.07	0.10	0.06	0.10
MnO	0.01	0.03	0.00	0.00	0.05	0.00	0.05	0.05	0.00	0.03	0.02	0.00	0.00	0.04	0.01	0.00	0.00
MgO	0.00	0.00	0.00	0.00	0.00	0.26	0.00	0.00	0.00	0.00	0.00	0.00	0.00	0.00	0.00	0.00	0.00
CaO	16.62	16.33	15.64	16.25	15.75	15.57	16.74	15.31	15.83	16.64	16.29	16.64	16.58	15.82	16.10	16.04	16.04
Na_2O	4.33	4.46	4.62	4.33	4.68	4.04	4.41	5.04	4.81	4.21	4.10	4.17	4.17	4.27	4.42	4.44	4.27
K_2O	0.26	0.17	0.23	0.14	0.18	0.16	0.21	0.26	0.35	0.12	0.42	0.43	0.32	0.34	0.29	0.28	0.29
Cl	0.40	0.35	0.48	0.31	0.37	0.39	0.40	0.59	0.73	0.29	0.49	0.52	0.40	0.40	0.35	0.35	0.37
SO_3	2.87	3.76	3.21	3.63	4.01	3.48	2.74	1.56	1.48	3.92	3.99	3.65	3.52	5.44	4.89	5.11	5.10
Total	97.86	97.96	96.81	98.40	98.01	96.66	97.60	97.17	97.27	98.17	97.78	98.22	98.08	98.69	98.84	98.93	97.83
Si	7.25	7.27	7.33	7.24	7.33	7.27	7.21	7.41	7.32	7.27	7.30	7.21	7.22	7.32	7.34	7.30	7.28
Al	4.74	4.72	4.66	4.76	4.66	4.72	4.79	4.56	4.68	4.72	4.70	4.79	4.77	4.67	4.65	4.69	4.71
Fe^{3+}	0.00	0.00	0.01	0.00	0.01	0.01	0.00	0.03	0.00	0.01	0.00	0.00	0.01	0.01	0.01	0.01	0.01
Mn	0.00	0.00	0.00	0.00	0.01	0.00	0.01	0.01	0.00	0.00	0.00	0.00	0.00	0.00	0.00	0.00	0.00
Mg	0.00	0.00	0.00	0.00	0.00	0.06	0.00	0.00	0.00	0.00	0.00	0.00	0.00	0.00	0.00	0.00	0.00
Ca	2.74	2.71	2.61	2.66	2.61	2.59	2.77	2.50	2.59	2.76	2.72	2.76	2.74	2.64	2.68	2.67	2.70
Na	1.29	1.34	1.39	1.29	1.40	1.21	1.32	1.49	1.42	1.26	1.24	1.25	1.25	1.29	1.33	1.33	1.30
K	0.05	0.03	0.05	0.03	0.03	0.03	0.04	0.05	0.07	0.02	0.08	0.08	0.06	0.07	0.06	0.06	0.06
S	0.33	0.44	0.37	0.42	0.46	0.41	0.32	0.18	0.17	0.45	0.47	0.42	0.41	0.64	0.57	0.60	0.60
Cl	0.10	0.09	0.13	0.08	0.10	0.10	0.10	0.15	0.19	0.08	0.13	0.14	0.11	0.10	0.09	0.09	0.10
C (calc.)	0.56	0.47	0.50	0.50	0.44	0.49	0.58	0.67	0.64	0.47	0.40	0.44	0.49	0.26	0.34	0.31	0.30
tot. cat.	16.52	16.62	16.55	16.47	16.62	16.40	16.55	16.37	16.44	16.58	16.64	16.66	16.56	16.75	16.72	16.75	16.76
tot. oxy.	26.03	26.35	26.11	26.19	26.39	26.12	26.01	25.51	25.50	26.40	26.43	26.30	26.23	26.90	26.75	26.80	26.83
Me	67.14	66.36	64.41	67.00	64.45	67.50	67.07	61.90	63.44	68.18	67.27	67.39	67.64	66.05	65.90	65.73	66.53
Ma	31.62	32.81	34.44	32.34	34.68	31.69	31.94	36.85	34.87	31.22	30.66	30.55	30.82	32.24	32.71	32.90	32.05

Sample	HIL13-16			HIL13-17										HIL13-19		ESP-5-13	
number	1	5	8	1	4	5	11	12	13	14	17	23	25	45	52	6	10
	wall	in vein						hydrated in vein						granulite		hydrated	
SiO_2	47.42	47.60	47.26	50.07	48.40	48.54	49.32	47.79	48.29	48.70	47.81	48.29	48.20	45.96	45.17	50.60	53.50
Al_2O_3	25.04	24.61	24.64	24.01	25.00	24.74	24.72	25.79	25.25	24.85	25.28	25.51	25.28	25.99	26.88	23.09	23.11
Cr_2O_3				0.00	0.00	0.00	0.00	0.01	0.02	0.00	0.00	0.00	0.00				
FeO	0.07	0.03	0.05	0.12	0.02	0.00	0.09	0.15	0.17	0.04	0.04	0.07	0.10	0.08	0.10	0.13	0.11
MnO	0.00	0.01	0.00	0.03	0.04	0.02	0.03	0.00	0.03	0.00	0.00	0.05	0.01	0.00	0.01	0.02	0.00
MgO	0.00	0.01	0.00	0.00	0.00	0.00	0.00	0.00	0.00	0.00	0.00	0.00	0.01	0.00	0.00	0.00	0.00
CaO	15.69	15.41	15.06	13.77	15.10	14.87	14.35	16.00	15.21	15.01	15.72	15.17	15.51	17.31	17.67	13.01	10.71
Na_2O	4.75	4.90	4.78	5.70	4.80	5.24	5.67	4.66	4.96	5.27	4.76	5.02	4.87	3.76	3.57	6.35	7.91
K_2O	0.23	0.20	0.21	0.10	0.17	0.11	0.13	0.17	0.13	0.11	0.08	0.12	0.17	0.34	0.22	0.12	0.35
Cl	0.51	0.59	0.59	0.42	0.41	0.51	0.68	0.42	0.47	0.47	0.35	0.48	0.49	0.38	0.33	0.59	1.76
SO_3	5.28	5.78	5.88	4.82	3.87	3.73	3.48	2.97	3.36	3.60	3.73	2.61	3.22	3.91	3.79	5.43	1.90
Total	98.94	99.16	98.46	99.04	97.79	97.72	98.44	97.93	97.88	98.02	97.74	97.32	97.84	97.70	97.70	99.33	99.30
Si	7.39	7.45	7.43	7.66	7.46	7.50	7.54	7.32	7.41	7.49	7.39	7.39	7.41	7.19	7.05	7.79	7.94
Al	4.60	4.54	4.57	4.33	4.54	4.50	4.45	4.66	4.57	4.50	4.61	4.60	4.58	4.80	4.94	4.19	4.04
Fe^{3+}	0.01	0.00	0.01	0.02	0.00	0.00	0.01	0.02	0.02	0.00	0.01	0.01	0.01	0.01	0.01	0.02	0.01
Mn	0.00	0.00	0.00	0.00	0.01	0.00	0.00	0.00	0.00	0.00	0.00	0.01	0.00	0.00	0.00	0.00	0.00
Mg	0.00	0.00	0.00	0.00	0.00	0.00	0.00	0.00	0.00	0.00	0.00	0.00	0.00	0.00	0.00	0.00	0.00
Ca	2.62	2.58	2.54	2.26	2.49	2.46	2.35	2.63	2.50	2.47	2.60	2.49	2.55	2.90	2.95	2.15	1.70
Na	1.43	1.49	1.46	1.69	1.43	1.57	1.68	1.38	1.48	1.57	1.43	1.49	1.45	1.14	1.08	1.90	2.28
K	0.05	0.04	0.04	0.02	0.03	0.02	0.03	0.03	0.03	0.02	0.02	0.02	0.03	0.07	0.04	0.02	0.07
S	0.62	0.68	0.69	0.55	0.45	0.43	0.40	0.34	0.39	0.42	0.43	0.30	0.37	0.46	0.44	0.63	0.21
Cl	0.13	0.16	0.16	0.11	0.11	0.13	0.17	0.11	0.12	0.12	0.09	0.12	0.13	0.10	0.09	0.15	0.44
C (calc.)	0.25	0.16	0.15	0.34	0.45	0.43	0.43	0.55	0.49	0.46	0.47	0.58	0.50	0.44	0.47	0.22	0.35
tot. cat.	16.85	16.95	16.89	16.63	16.52	16.62	16.63	16.49	16.52	16.60	16.57	16.43	16.54	16.67	16.61	16.85	16.70
tot. oxy.	26.91	27.12	27.08	26.60	26.30	26.30	26.17	26.02	26.13	26.26	26.32	25.84	26.12	26.48	26.37	26.89	25.48
Me	63.92	62.83	62.84	56.90	62.91	60.73	57.93	64.98	62.45	60.82	64.36	62.17	63.23	70.58	72.45	52.79	42.11
Ma	34.98	36.19	36.13	42.63	36.22	38.74	41.44	34.22	36.90	38.65	35.25	37.23	35.93	27.77	26.45	46.65	56.26

TABLE A.3: Scapolite EMP analyses from granulite and amphibolite samples from Isdal. Values are presented in oxide weight percent. Scapolite is normalised to T = Si+Al+Fe^{3+}. C (calculated) = 100-(S+Cl), Me = Ca/(Ca+Na), Ma = Na/(Ca+Na)

Sample	ISD13-01A					ISD13-01B			ISD13-04				ISD13-06				44-91A
number	7	13	14	16	17	20	27	29	4	10	12	14	23	37	41	42	1
	edge	wall		edge	wall	edge	in vein	wall	mafic				mafic		wall		granulite
SiO_2	48.30	47.87	48.42	47.11	49.23	48.20	48.31	49.20	47.44	47.60	47.04	47.78	48.45	46.42	46.91	46.91	47.40
Al_2O_3	25.72	26.21	25.50	25.27	25.18	24.75	25.58	25.85	25.11	24.23	25.15	25.59	22.99	23.98	25.65	25.18	24.23
Cr_2O_3																	
FeO	0.06	0.07	0.14	0.05	0.07	0.02	0.13	0.11	0.07	0.00	0.06	0.23	0.97	0.89	0.08	0.04	0.05
MnO	0.00	0.01	0.00	0.03	0.03	0.00	0.03	0.00	0.02	0.01	0.02	0.05	0.02	0.03	0.00	0.03	0.00
MgO	0.00	0.00	0.01	0.00	0.00	0.00	0.00	0.00	0.00	0.00	0.00	0.12	0.64	0.45	0.00	0.00	0.00
CaO	15.64	16.42	15.83	16.15	14.72	15.37	15.72	15.34	15.53	15.39	16.03	15.85	14.04	15.18	16.62	16.00	15.72
Na_2O	4.93	4.55	5.04	4.44	5.54	4.89	4.93	5.28	4.79	4.94	4.49	4.97	5.23	4.47	4.16	4.49	4.84
K_2O	0.10	0.09	0.08	0.05	0.12	0.04	0.13	0.12	0.08	0.04	0.04	0.10	0.06	0.06	0.21	0.17	0.06
Cl	0.52	0.42	0.53	0.18	0.81	0.21	0.61	0.70	0.24	0.16	0.10	0.41	0.16	0.10	0.15	0.16	0.02
SO_3	2.44	1.07	2.73	5.53	1.38	5.27	1.18	1.41	5.93	6.11	5.92	1.38	5.99	6.10	5.88	6.09	7.21
Total	97.65	96.69	98.27	98.79	97.06	98.74	96.59	97.98	99.16	98.44	98.84	96.49	98.54	97.70	99.64	99.05	99.52
Si	7.37	7.29	7.39	7.35	7.48	7.47	7.38	7.40	7.38	7.50	7.36	7.34	7.61	7.39	7.29	7.35	7.48
Al	4.62	4.70	4.59	4.64	4.51	4.52	4.60	4.58	4.61	4.50	4.63	4.63	4.26	4.50	4.70	4.65	4.51
Fe^{3+}	0.01	0.01	0.02	0.01	0.01	0.00	0.02	0.01	0.01	0.00	0.01	0.03	0.13	0.12	0.01	0.00	0.01
Mn	0.00	0.00	0.00	0.00	0.00	0.00	0.00	0.00	0.00	0.00	0.00	0.01	0.00	0.00	0.00	0.00	0.00
Mg	0.00	0.00	0.00	0.00	0.00	0.00	0.00	0.00	0.00	0.00	0.00	0.03	0.15	0.11	0.00	0.00	0.00
Ca	2.56	2.68	2.59	2.70	2.40	2.55	2.57	2.47	2.59	2.60	2.69	2.61	2.36	2.59	2.77	2.69	2.66
Na	1.46	1.34	1.49	1.34	1.63	1.47	1.46	1.54	1.45	1.51	1.36	1.48	1.59	1.38	1.25	1.36	1.48
K	0.02	0.02	0.02	0.01	0.02	0.01	0.02	0.02	0.02	0.01	0.01	0.02	0.01	0.01	0.04	0.03	0.01
S	0.28	0.12	0.31	0.65	0.16	0.61	0.14	0.16	0.69	0.72	0.69	0.16	0.71	0.73	0.69	0.72	0.85
Cl	0.13	0.11	0.14	0.05	0.21	0.06	0.16	0.18	0.06	0.04	0.03	0.11	0.04	0.03	0.04	0.04	0.00
C (calc.)	0.59	0.77	0.55	0.30	0.63	0.33	0.71	0.66	0.25	0.24	0.28	0.73	0.25	0.24	0.27	0.24	0.14
tot. cat.	16.45	16.27	16.55	16.75	16.42	16.70	16.35	16.37	16.81	16.88	16.78	16.41	16.87	16.85	16.79	16.85	17.01
tot. oxy.	25.82	25.37	25.98	27.00	25.44	26.86	25.41	25.43	27.09	27.28	27.14	25.54	27.25	27.28	27.12	27.21	27.71
Me	63.38	66.33	63.19	66.62	59.14	63.32	63.42	61.27	63.92	63.11	66.23	63.49	59.54	65.01	68.13	65.77	64.01
Ma	36.14	33.24	36.42	33.13	40.29	36.46	35.97	38.15	35.67	36.68	33.55	36.04	40.17	34.66	30.87	33.42	35.68

Sample	ISD13-07A2					ISD13-07B								AK72-98II			
number	46	50	67	78	84	7	9	10	13	14	17	22	25	12	18	22	28
			in vein					hydrated in vein				wall		mafic		wall	mafic
SiO_2	47.80	47.69	46.23	45.94	46.68	47.52	46.71	47.09	46.93	46.91	47.91	47.70	46.66	48.25	48.51	46.60	47.51
Al_2O_3	24.76	25.45	25.45	24.65	25.09	25.88	26.09	26.04	26.10	26.21	25.56	25.82	25.98	24.60	24.53	25.40	24.99
Cr_2O_3	0.00	0.00															
FeO	0.08	0.20	0.04	0.18	0.24	0.12	0.11	0.09	0.07	0.09	0.14	0.03	0.13	0.25	0.42	0.05	0.13
MnO	0.00	0.00	0.00	0.03	0.00	0.00	0.01	0.03	0.01	0.00	0.00	0.01	0.02	0.01	0.01	0.01	0.00
MgO	0.00	0.00	0.00	0.00	0.00	0.00	0.01	0.02	0.00	0.00	0.00	0.00	0.16	0.00	0.03	0.00	0.00
CaO	15.47	16.15	16.27	16.01	16.09	16.30	16.85	16.84	16.72	16.94	16.28	16.52	15.98	15.43	14.85	16.24	15.77
Na_2O	4.84	4.35	4.29	4.39	4.45	4.33	3.98	4.28	4.22	4.06	4.40	4.41	3.81	4.91	5.15	4.21	4.67
K_2O	0.15	0.21	0.23	0.18	0.11	0.08	0.07	0.06	0.05	0.06	0.10	0.05	0.08	0.04	0.03	0.11	0.03
Cl	0.11	0.24	0.21	0.14	0.17	0.20	0.15	0.18	0.19	0.11	0.17	0.24	0.18	0.07	0.07	0.09	0.03
SO_3	6.32	3.37	6.03	7.01	6.84	3.09	2.78	3.18	3.21	3.63	3.15	2.73	2.43	5.41	5.86	6.29	6.34
Total	99.46	97.59	98.74	98.51	99.62	97.52	96.77	97.80	97.49	97.99	97.70	97.49	95.43	98.98	99.45	98.99	99.47
Si	7.44	7.35	7.28	7.34	7.33	7.30	7.23	7.26	7.24	7.23	7.36	7.32	7.24	7.48	7.49	7.30	7.40
Al	4.55	4.62	4.72	4.64	4.64	4.69	4.76	4.73	4.75	4.76	4.63	4.67	4.75	4.49	4.46	4.69	4.59
Fe^{3+}	0.01	0.03	0.01	0.02	0.03	0.02	0.01	0.01	0.01	0.01	0.02	0.00	0.02	0.03	0.05	0.01	0.02
Mn	0.00	0.00	0.00	0.00	0.00	0.00	0.00	0.00	0.00	0.00	0.00	0.00	0.00	0.00	0.00	0.00	0.00
Mg	0.00	0.00	0.00	0.00	0.00	0.00	0.00	0.01	0.00	0.00	0.00	0.00	0.04	0.00	0.01	0.00	0.00
Ca	2.58	2.67	2.74	2.74	2.71	2.68	2.79	2.78	2.76	2.80	2.68	2.72	2.66	2.56	2.46	2.73	2.63
Na	1.46	1.30	1.31	1.36	1.36	1.29	1.19	1.28	1.26	1.21	1.31	1.31	1.15	1.48	1.54	1.28	1.41
K	0.03	0.04	0.05	0.04	0.02	0.02	0.01	0.01	0.01	0.01	0.02	0.01	0.01	0.01	0.01	0.02	0.01
S	0.74	0.39	0.71	0.84	0.81	0.36	0.32	0.37	0.37	0.42	0.36	0.31	0.28	0.63	0.68	0.74	0.74
Cl	0.03	0.06	0.06	0.04	0.04	0.05	0.04	0.05	0.05	0.03	0.05	0.06	0.05	0.02	0.02	0.02	0.01
C (calc.)	0.23	0.55	0.23	0.12	0.15	0.59	0.64	0.59	0.58	0.55	0.59	0.62	0.67	0.35	0.30	0.24	0.25
tot. cat.	16.84	16.46	16.87	17.02	16.93	16.40	16.37	16.49	16.46	16.47	16.42	16.42	16.19	16.69	16.71	16.79	16.79
tot. oxy.	27.27	26.18	27.20	27.63	27.48	26.05	25.98	26.17	26.14	26.28	26.11	25.98	25.74	26.93	27.02	27.25	27.26
Me	63.40	66.53	66.92	66.24	66.26	67.28	69.81	68.34	68.49	69.56	66.82	67.30	69.59	63.33	61.35	67.70	65.02
Ma	35.85	32.43	31.95	32.87	33.19	32.34	29.85	31.39	31.29	30.14	32.71	32.48	30.02	36.49	38.50	31.74	34.85

TABLE A.4: Plagioclase EMP analyses from granulite and amphibolite samples. Values are presented in oxide weight percent. Plagioclase is normalised to 5 cations. All iron is Fe^{2+}.

Sample	HIL13-15A				HIL13-16	HIL13-17		HIL13-18A			HIL13-19			AK72-98II		
#	34	35	38	41	3	20	19	44	47	47	46	55	60	11	19	23
Rock	scapolite front w. shears				granulite	hydrated					granulite			mafic		granulite
mineral	andesine				andesine	andesine	oligoclase	andesine		bytownite	labradorite			oligoclase	andesine	
SiO_2	56.76	57.20	57.23	59.94	57.02	58.00	62.65	57.38	56.52	58.98	54.89	53.31	54.06	59.87	58.40	59.79
Al_2O_3	27.39	27.09	26.68	25.46	26.51	26.59	23.47	27.29	27.39	25.20	28.33	29.16	28.49	25.13	26.10	24.99
TiO_2	0.00	0.00	0.01	0.00	0.03	0.00	0.00	0.00	0.01	0.03	0.01	0.02	0.00	0.00	0.01	0.02
Cr_2O_3	0.01	0.01	0.00	0.00	0.03	0.00	0.01	0.00	0.00	0.00	0.00	0.00	0.03	0.01	0.00	0.02
FeO	0.00	0.00	0.03	0.19	0.00	0.02	0.00	0.04	0.03	0.05	0.04	0.03	0.15	0.14	0.39	0.04
MnO	0.01	0.00	0.00	0.01	0.00	0.02	0.00	0.00	0.00	0.00	0.00	0.01	0.00	0.00	0.00	0.02
MgO	0.00	0.00	0.00	0.00	0.00	0.00	0.00	0.00	0.00	0.21	0.00	0.00	0.00	0.00	0.02	0.00
CaO	9.26	9.15	8.98	7.00	9.01	8.24	4.74	9.46	9.46	12.47	11.08	12.26	11.42	6.95	8.06	6.50
Na_2O	6.46	6.49	6.73	7.80	6.56	6.93	9.01	6.36	6.26	1.05	5.53	4.88	5.20	7.91	7.14	7.81
K_2O	0.13	0.11	0.11	0.11	0.07	0.05	0.05	0.23	0.19	1.62	0.17	0.12	0.16	0.09	0.06	0.32
Total	99.99	99.98	99.75	100.49	99.19	99.81	99.89	99.46	99.46	99.56	100.00	99.78	99.47	99.46	99.46	99.46
Si^{4+}	2.54	2.56	2.57	2.66	2.57	2.60	2.77	2.56	2.54	2.77	2.47	2.41	2.45	2.77	2.61	2.68
Ti	0.00	0.00	0.00	0.00	0.00	0.00	0.00	0.00	0.00	0.00	0.00	0.00	0.00	0.00	0.00	0.00
Al	1.45	1.43	1.41	1.33	1.41	1.40	1.23	1.44	1.45	1.39	1.50	1.56	1.52	1.22	1.37	1.32
Cr	0.00	0.00	0.00	0.00	0.00	0.00	0.00	0.00	0.00	0.00	0.00	0.00	0.00	0.00	0.00	0.00
Fe^{2+}	0.00	0.00	0.00	0.01	0.00	0.00	0.00	0.00	0.00	0.00	0.00	0.00	0.01	0.00	0.01	0.00
Mn	0.00	0.00	0.00	0.00	0.00	0.00	0.00	0.00	0.00	0.00	0.00	0.00	0.00	0.00	0.00	0.00
Mg	0.00	0.00	0.00	0.00	0.00	0.00	0.00	0.00	0.00	0.01	0.00	0.00	0.00	0.00	0.00	0.00
Ca	0.44	0.44	0.43	0.33	0.44	0.40	0.22	0.45	0.45	0.63	0.53	0.59	0.55	0.22	0.39	0.31
Na	0.56	0.56	0.59	0.67	0.57	0.60	0.77	0.55	0.55	0.10	0.48	0.43	0.46	0.77	0.62	0.68
K	0.01	0.01	0.01	0.01	0.00	0.00	0.00	0.00	0.01	0.10	0.01	0.01	0.01	0.00	0.00	0.00
Sum	5	5	5	5	5	5	5	5	5	5	5	5	5	5	5	5
An	43.90	43.52	42.19	32.95	42.97	39.53	22.45	45.09	44.99	76.52	52.04	57.76	54.36	22.45	38.40	31.47
Ab	55.39	55.84	57.19	66.42	56.63	60.18	77.25	54.91	53.92	11.62	46.99	41.56	44.75	77.25	61.56	68.43
Or	0.71	0.64	0.62	0.63	0.40	0.29	0.30	0.00	1.09	11.86	0.97	0.68	0.89	0.30	0.05	0.11

Sample	ISD13-01A			ISD13-01B				ISD13-04			ISD13-06			ISD13-07B	
#	1	8	12	18	22	24	26	30	9	15	32	36	38	21	26
Rock		hydrated				sheared			altered jotunite			mafic zone			hydrated
mineral		andesine				andesine			andesine	oligoclase	oligoclase	andesine			andesine
SiO_2	59.43	58.83	57.79	58.77	59.02	60.55	58.72	57.55	59.88	61.54	62.91	58.75	60.20	60.07	58.89
Al_2O_3	25.52	25.43	26.46	26.44	26.19	24.94	25.84	26.97	24.82	24.43	23.10	25.49	25.09	24.99	25.37
TiO_2	0.00	0.00	0.01	0.01	0.00	0.02	0.01	0.00			0.02	0.01	0.01	0.00	0.00
Cr_2O_3	0.00	0.01	0.00	0.00	0.00	0.02	0.02	0.00			0.02	0.00	0.00	0.07	0.00
FeO	0.01	0.03	0.05	0.01	0.01	0.08	0.04	0.09	0.00	0.04	0.09	0.12	0.02	0.00	0.01
MnO	0.00	0.00	0.00	0.03	0.00	0.02	0.00	0.01	0.00	0.03	0.01	0.00	0.00	0.00	0.00
MgO	0.00	0.00	0.00	0.00	0.00	0.00	0.00	0.00	0.00	0.01	0.00	0.00	0.00	0.01	0.00
CaO	7.46	7.41	8.70	8.24	8.01	6.89	7.57	9.12	6.45	5.76	4.68	7.73	6.61	6.77	7.67
Na_2O	7.71	7.62	6.99	7.24	7.21	7.93	7.47	6.65	8.11	8.71	9.03	7.42	7.80	7.83	7.51
K_2O	0.07	0.02	0.06	0.05	0.05	0.03	0.05	0.04	0.05	0.05	0.23	0.14	0.44	0.04	0.05
Total	100.14	99.35	100.03	100.73	100.48	100.49	99.68	100.39	99.27	100.58	100.05	99.62	100.14	99.75	99.46
Si^{4+}	2.64	2.64	2.58	2.60	2.62	2.68	2.62	2.57	2.68	2.71	2.78	2.63	2.67	2.68	2.64
Ti	0.00	0.00	0.00	0.00	0.00	0.00	0.00	0.00	0.00	0.00	0.00	0.00	0.00	0.00	0.00
Al	1.34	1.34	1.39	1.38	1.37	1.30	1.36	1.42	1.31	1.27	1.20	1.34	1.31	1.31	1.34
Cr	0.00	0.00	0.00	0.00	0.00	0.00	0.00	0.00	0.00	0.00	0.00	0.00	0.00	0.00	0.00
Fe^{2+}	0.00	0.00	0.00	0.00	0.00	0.00	0.00	0.00	0.00	0.00	0.00	0.00	0.00	0.00	0.00
Mn	0.00	0.00	0.00	0.00	0.00	0.00	0.00	0.00	0.00	0.00	0.00	0.00	0.00	0.00	0.00
Mg	0.00	0.00	0.00	0.00	0.00	0.00	0.00	0.00	0.00	0.00	0.00	0.00	0.00	0.00	0.00
Ca	0.36	0.36	0.42	0.39	0.38	0.33	0.36	0.44	0.31	0.27	0.22	0.37	0.31	0.32	0.37
Na	0.66	0.66	0.61	0.62	0.62	0.68	0.65	0.58	0.70	0.74	0.77	0.64	0.67	0.68	0.65
K	0.00	0.00	0.00	0.00	0.00	0.00	0.00	0.00	0.00	0.00	0.01	0.01	0.02	0.00	0.00
Sum	5	5	5	5	5	5	5	5	5	5	5	5	5	5	5
An	34.70	34.90	40.62	38.52	37.94	32.40	35.79	43.01	30.45	26.68	21.98	36.26	31.09	32.26	35.96
Ab	64.92	64.98	59.06	61.21	61.76	67.42	63.93	56.77	69.25	73.05	76.74	62.97	66.45	67.52	63.75
Or	0.38	0.12	0.32	0.27	0.30	0.18	0.28	0.22	0.29	0.27	1.27	0.76	2.45	0.22	0.28

TABLE A.5: Epidote EMP analyses from granulite and amphibolite samples. Values are presented in oxide weight percent. Epidote is normalised to 12.5 oxygen units. All iron is Fe^{3+}.

Sample	HIL-15A				HIL13-16		HIL13-17						HIL13-19			HIL13-18B				
number	33	39	46	50	6	9	8	9	15	16	22	24	48	53	59	27	28	33	37	40
		dark			in vein		rim	core								light	dark			
SiO_2	38.58	38.41	38.58	38.92	37.72	37.75	37.85	38.16	38.12	38.60	38.35	38.04	38.84	38.99	41.10	37.35	38.14	38.29	38.12	37.62
Al_2O_3	27.77	26.63	26.83	26.90	25.66	24.98	27.26	28.32	26.96	27.37	27.33	26.76	28.29	26.93	25.99	21.94	25.41	27.87	25.43	24.70
TiO_2	0.10	0.11	0.09	0.05	0.07						0.11	0.09	0.04		0.02	0.09	0.03	0.02	0.13	0.02
Cr_2O_3	0.00	0.00	0.04	0.00	0.00		0.00	0.00	0.03	0.00	0.01	0.00	0.00		0.02	0.00	0.00	0.00	0.00	0.00
FeO	6.68	8.27	7.59	8.13	9.05	9.85	7.35	5.60	7.57	7.73	7.15	7.73	7.08	6.21	6.71	13.49	10.14	6.41	9.43	10.26
MnO	0.12	0.05	0.09	0.08	0.09	0.09	0.14	0.06	0.14	0.11	0.13	0.18	0.01	0.00	0.02	0.10	0.10	0.48	0.06	0.07
MgO	0.04	0.05	0.03	0.06	0.04	0.00	0.05	0.20	0.10	0.04	0.10	0.08	0.03	0.66	0.00	0.00	0.03	0.00	0.03	0.00
CaO	23.90	23.80	24.14	23.93	23.83	24.01	23.76	23.73	23.17	23.79	23.92	23.72	23.73	24.45	23.36	23.37	23.83	23.77	23.68	23.34
Na_2O	0.02	0.02	0.03	0.00	0.01	0.03	0.00	0.01	0.00	0.02	0.02	0.02	0.02	0.04	0.00	0.00	0.00	0.00	0.01	0.00
K_2O	0.01	0.01	0.01	0.00	0.00	0.00	0.00	0.00	0.00	0.00	0.00	0.01	0.03	0.03	0.00	0.00	0.01	0.00	0.00	0.00
Total	97.18	97.35	97.41	98.03	96.46	96.70	96.42	96.08	96.05	97.67	97.11	96.60	98.07	97.31	97.21	96.29	97.64	96.81	96.89	96.00
Si^{4+}	3.00	3.00	3.01	3.01	2.99	2.99	2.98	3.00	3.01	3.00	2.99	2.99	2.99	3.03	3.18	3.00	2.99	3.00	3.00	3.00
Ti	0.01	0.01	0.01	0.00	0.00	0.00	0.00	0.00	0.00	0.00	0.01	0.01	0.00	0.00	0.00	0.01	0.00	0.00	0.01	0.00
Al	2.55	2.45	2.47	2.45	2.39	2.33	2.53	2.62	2.51	2.51	2.52	2.48	2.57	2.47	2.37	2.08	2.34	2.57	2.36	2.32
Fe^{3+}	0.43	0.54	0.50	0.53	0.60	0.65	0.48	0.37	0.50	0.50	0.47	0.51	0.46	0.40	0.43	0.91	0.66	0.42	0.62	0.68
Mn	0.01	0.00	0.01	0.01	0.01	0.01	0.01	0.00	0.01	0.01	0.01	0.01	0.00	0.00	0.00	0.01	0.01	0.03	0.00	0.00
Mg	0.00	0.01	0.00	0.01	0.01	0.00	0.01	0.02	0.01	0.00	0.01	0.01	0.00	0.08	0.00	0.00	0.00	0.00	0.00	0.00
Ca	1.99	1.99	2.02	1.99	2.02	2.04	2.00	2.00	1.96	1.98	2.00	2.00	1.96	2.04	1.94	2.01	2.00	1.99	2.00	1.99
Na	0.00	0.00	0.00	0.00	0.00	0.00	0.00	0.00	0.00	0.00	0.00	0.00	0.00	0.01	0.00	0.00	0.00	0.00	0.00	0.00
K	0.00	0.00	0.00	0.00	0.00	0.00	0.00	0.00	0.00	0.00	0.00	0.00	0.00	0.00	0.00	0.00	0.00	0.00	0.00	0.00
Sum	8.00	8.00	8.01	7.99	8.02	8.02	8.01	8.01	7.99	8.00	8.01	8.01	7.99	8.03	7.92	8.00	8.01	8.01	8.00	8.00

Sample	HIL13-03		ISD13-01A		ISD13-01B		ISD13-04		ISD13-07A2		ISD13-07B					44-91A			ESP-5-13		
number	27	32	2	5	6	19	5	8	70	75	1	3	8	11	15	2	3	4	5	7	8
			in vein	edge	edge	wall							in vein							core	rim
SiO_2	37.47	37.78	40.60	39.83	38.42	38.15	38.52	38.24	38.17	38.58	38.68	38.40	38.52	38.40	38.40	38.24	38.67	38.27	38.31	38.95	38.05
Al_2O_3	25.01	25.19	26.95	26.27	26.51	26.55	28.19	26.79	26.17	25.87	28.00	27.64	28.44	27.91	27.72	27.66	27.06	28.20	25.13	27.78	24.96
TiO_2	0.00	0.05	0.08	0.04	0.07	0.04			0.32	0.02	0.17	0.20	0.11	0.18	0.18	0.09	0.13	0.15	0.12	0.07	0.11
Cr_2O_3	0.00	0.02	0.06	0.02	0.00	0.02			0.00	0.00	0.00	0.00	0.00	0.05	0.00	0.00	0.00	0.03	0.04	0.01	0.00
FeO	9.79	9.62	7.27	8.47	8.69	8.23	6.03	7.87	8.08	7.44	6.59	6.59	6.38	6.43	6.71	6.55	7.50	6.58	9.98	7.00	9.84
MnO	0.04	0.09	0.06	0.02	0.05	0.08	0.06	0.09	0.01	0.06	0.03	0.03	0.05	0.04	0.05	0.08	0.04	0.05	0.15	0.04	0.21
MgO	0.00	0.00	0.02	0.02	0.03	0.00	0.06	0.02	0.89	0.08	0.13	0.13	0.08	0.12	0.11	0.03	0.14	0.06	0.00	0.04	0.01
CaO	24.01	24.03	23.83	23.71	24.32	23.88	24.13	24.09	22.38	23.69	24.28	23.73	24.24	23.92	24.03	24.30	23.50	23.74	23.80	23.30	23.69
Na_2O	0.00	0.00	0.01	0.00	0.00	0.00	0.00	0.00	0.00	0.01	0.00	0.00	0.00	0.00	0.00	0.02	0.03	0.00	0.01	0.01	0.02
K_2O	0.00	0.00	0.00	0.00	0.00	0.00	0.00	0.01	0.78	0.00	0.01	0.01	0.00	0.02	0.00	0.12	0.03	0.00	0.01	0.00	0.00
Total	96.26	96.73	98.88	98.36	98.07	96.95	96.99	97.10	96.74	95.74	97.87	96.72	97.81	97.08	97.19	97.04	97.08	97.07	97.55	97.20	96.86
Si^{4+}	2.98	2.99	3.10	3.07	2.99	2.99	3.00	2.99	3.00	3.06	2.99	3.00	2.98	2.99	2.99	2.99	3.02	2.98	3.00	3.02	3.00
Ti	0.00	0.00	0.00	0.00	0.00	0.00	0.00	0.00	0.02	0.00	0.01	0.01	0.01	0.01	0.01	0.01	0.01	0.01	0.01	0.00	0.01
Al	2.34	2.35	2.43	2.39	2.43	2.46	2.59	2.47	2.42	2.42	2.55	2.55	2.59	2.56	2.55	2.55	2.49	2.59	2.32	2.54	2.32
Fe^{3+}	0.65	0.64	0.46	0.55	0.56	0.54	0.39	0.52	0.53	0.49	0.43	0.43	0.41	0.42	0.44	0.43	0.49	0.43	0.65	0.45	0.65
Mn	0.00	0.01	0.00	0.00	0.00	0.00	0.00	0.01	0.00	0.00	0.00	0.00	0.00	0.00	0.00	0.00	0.00	0.00	0.01	0.00	0.01
Mg	0.00	0.00	0.00	0.00	0.00	0.00	0.01	0.00	0.10	0.01	0.02	0.02	0.01	0.01	0.01	0.00	0.02	0.01	0.00	0.00	0.00
Ca	2.05	2.04	1.95	1.96	2.02	2.01	2.01	2.02	1.88	2.01	2.01	1.99	2.01	2.00	2.01	2.03	1.96	1.98	2.00	1.94	2.00
Na	0.00	0.00	0.00	0.00	0.00	0.00	0.00	0.00	0.00	0.00	0.00	0.00	0.00	0.00	0.00	0.00	0.00	0.00	0.00	0.00	0.00
K	0.00	0.00	0.00	0.00	0.00	0.00	0.00	0.00	0.08	0.00	0.00	0.00	0.00	0.00	0.00	0.01	0.00	0.00	0.00	0.00	0.00
Sum	8.03	8.02	7.95	7.96	8.01	8.01	8.01	8.01	8.04	7.99	8.01	8.00	8.01	8.00	8.01	8.03	7.99	8.00	8.00	7.97	8.00

TABLE A.6: Garnet EMP analyses from granulite and amphibolite samples. Values are presented in oxide weight percent. Garnet is normalised to 12 oxygens and 8 cations.

Sample	HIL13-15A	HIL13-18A			HIL13-19		ISD13-01A	ISD13-01B		ISD13-06			ISD13-07A2	ISD13-07B
#	45	45	48	49	56	57	10	28	20	24	31	43	74	18
	front	granulite	front	rxn rim	granulite	rxn rim	granulite	hydrated	rxn rim	rxn rim	rxn rim	granulite	granulite	hydrated
SiO_2	39.28	39.67	39.68	37.87	39.42	38.35	40.04	39.65	38.24	38.25	38.38	39.77	39.33	39.86
Al_2O_3	21.92	22.29	22.17	21.10	22.13	21.86	22.06	22.00	21.07	21.24	21.67	21.75	21.96	22.45
TiO_2	0.10	0.26	0.27	0.03	0.12	0.03	0.12	0.14		0.06	0.05	0.16	0.07	0.15
Cr_2O_3	0.00	0.01	0.00	0.02	0.04	0.00	0.00	0.00		0.00	0.02	0.07	0.01	0.00
FeO	20.11	19.48	19.79	26.13	19.84	18.28	21.40	20.87	29.29	25.61	26.99	20.65	22.31	18.61
MnO	0.62	0.56	0.52	0.25	0.39	0.18	0.48	0.50	0.47	0.13	0.33	0.36	0.42	0.34
MgO	10.99	11.05	10.84	2.47	10.53	5.53	10.98	11.01	6.92	3.97	6.72	11.33	10.43	12.06
CaO	6.47	7.38	7.20	11.82	7.50	15.43	5.96	5.95	3.80	11.46	6.15	5.90	5.47	6.60
Na_2O	0.00	0.01	0.02	0.01	0.00	0.00	0.00	0.02	0.00	0.00	0.02	0.01	0.01	0.03
K_2O	0.00	0.00	0.00	0.01	0.00	0.03	0.00	0.02	0.00	0.00	0.00	0.00	0.01	0.00
Total	99.46	100.70	100.49	99.72	99.95	99.66	101.05	100.14	99.80	100.71	100.33	100.01	100.04	100.08
Si^{4+} (T)	2.97	2.96	2.97	2.99	2.97	2.94	2.99	2.98	2.99	2.97	2.97	2.99	2.98	2.97
Al^{IV} (T)	0.03	0.04	0.03	0.01	0.03	0.06	0.01	0.02	0.01	0.03	0.03	0.01	0.02	0.03
Ti (M1)	0.01	0.01	0.02	0.00	0.01	0.00	0.01	0.01	0.00	0.00	0.00	0.01	0.00	0.01
Al^{VI} (M1)	1.92	1.92	1.93	1.96	1.93	1.92	1.93	1.93	1.93	1.91	1.94	1.92	1.94	1.94
Cr (M1)	0.00	0.00	0.00	0.00	0.00	0.00	0.00	0.00	0.00	0.00	0.00	0.00	0.00	0.00
Fe^{3+} (M1)	0.07	0.07	0.06	0.04	0.06	0.08	0.06	0.06	0.07	0.08	0.05	0.07	0.06	0.05
Fe^{3+} (M2)	0.03	0.03	0.01	0.00	0.03	0.06	0.01	0.01	0.01	0.03	0.03	0.00	0.02	0.02
Fe^{2+} (M2)	1.17	1.12	1.17	1.69	1.16	1.03	1.27	1.24	1.83	1.55	1.67	1.23	1.33	1.09
Mn (M2)	0.04	0.04	0.03	0.02	0.02	0.01	0.03	0.03	0.03	0.01	0.02	0.02	0.03	0.02
Mg (M2)	1.24	1.23	1.21	0.29	1.18	0.63	1.22	1.23	0.81	0.46	0.78	1.27	1.18	1.34
Ca (M2)	0.52	0.59	0.58	1.00	0.61	1.27	0.48	0.48	0.32	0.95	0.51	0.48	0.44	0.53
Sum	8.00	8.00	8.00	8.00	8.00	8.00	8.00	8.00	8.00	8.00	8.00	8.00	8.00	8.00
almandine	39.44	38.22	39.33	56.36	39.62	36.30	42.37	41.79	61.47	52.65	56.46	41.03	45.07	36.62
pyrope	41.61	40.96	40.31	9.72	39.39	21.05	40.72	41.15	26.87	15.30	25.84	42.34	39.23	44.96
grossular	16.72	18.83	18.55	32.69	19.47	40.50	15.32	15.46	10.24	30.39	16.50	15.21	14.32	17.03
spessartine	1.34	1.17	1.10	0.56	0.82	0.38	1.02	1.06	1.05	0.28	0.73	0.77	0.90	0.72
andradite	0.84	0.67	0.57	0.62	0.61	1.75	0.51	0.47	0.37	1.32	0.44	0.54	0.44	0.60

TABLE A.7: Pyroxene EMP analyses from granulite and amphibolite samples, inside veins and wallrock. Values are presented in oxide weight percent. Pyroxene is normalised to 4 cations and 6 oxygens. Wo - wollastonite = (Ca/Ca+Mg+Fe), En - enstatite = (Mg/Ca+Mg+Fe), Fs - ferrosilite = (Fe/Ca+Mg+Fe)

Sample	HIL14-03				HIL13-15A	HIL13-18A			AK72-98II				
#	34	35	36	37	48	38	39	41	7	15	20	25	27
mineral	opx	cpx	opx	opx	cpx	cpx	cpx	cpx	opx	opx	opx	opx	cpx
SiO_2	50.47	50.45	52.08	51.87	47.41	46.97	47.08	47.12	51.63	51.68	51.90	51.60	50.39
Al_2O_3	3.36	4.55	2.57	2.34	8.70	8.86	8.89	8.22	2.87	2.79	2.78	2.80	5.12
TiO_2	0.07	0.50	0.04	0.12	1.70	1.61	1.67	1.75	0.10	0.06	0.05	0.04	0.68
Cr_2O_3	0.05	0.04	0.00	0.00	0.00	0.03	0.04	0.06	0.00	0.03	0.00	0.04	0.00
FeO	22.80	9.49	22.49	23.45	8.16	8.63	8.11	11.20	22.21	21.83	22.82	22.40	11.92
MnO	0.54	0.26	0.62	0.70	0.10	0.12	0.08	0.17	0.21	0.22	0.24	0.25	0.12
MgO	21.04	11.91	21.62	21.32	10.93	10.66	10.54	11.63	21.89	21.92	21.48	22.52	12.50
CaO	0.34	21.28	0.48	0.39	21.39	21.65	21.90	17.60	0.56	0.50	0.55	0.53	19.23
Na_2O	0.01	1.21	0.04	0.01	1.11	1.29	1.25	1.04	0.06	0.02	0.01	0.04	1.02
K_2O	0.00	0.01	0.00	0.01	0.01	0.00	0.01	0.00	0.00	0.00	0.01	0.01	0.00
Total	98.67	99.70	99.94	100.20	99.49	99.82	99.59	98.79	99.52	99.05	99.85	100.22	100.98
Si^{4+} (T)	1.91	1.88	1.94	1.94	1.77	1.75	1.76	1.78	1.93	1.94	1.94	1.91	1.86
Al^{IV} (T)	0.09	0.12	0.06	0.06	0.23	0.25	0.24	0.22	0.07	0.06	0.06	0.09	0.14
Ti (M1)	0.00	0.01	0.00	0.00	0.05	0.04	0.05	0.05	0.00	0.00	0.00	0.00	0.02
Al^{VI} (M1)	0.06	0.08	0.05	0.04	0.15	0.14	0.15	0.15	0.05	0.06	0.06	0.03	0.09
Cr (M1)	0.00	0.00	0.00	0.00	0.00	0.00	0.00	0.00		0.00	0.00	0.00	0.00
Fe^{3+} (M1)	0.03	0.10	0.00	0.02	0.06	0.12	0.10	0.05	0.02	0.00	0.00	0.06	0.09
Fe^{2+} (M1)	0.34	0.19	0.35	0.35	0.18	0.14	0.15	0.24	0.33	0.34	0.35	0.31	0.23
Mg (M1)	0.57	0.62	0.60	0.59	0.56	0.56	0.56	0.51	0.60	0.60	0.59	0.60	0.57
Fe^{2+} (M2)	0.36	0.01	0.35	0.36	0.01	0.01	0.01	0.07	0.34	0.35	0.36	0.33	0.05
Mn (M2)	0.02	0.01	0.02	0.02	0.00	0.00	0.00	0.01	0.01	0.01	0.01	0.01	0.00
Mg (M2)	0.61	0.04	0.61	0.60	0.05	0.03	0.03	0.14	0.62	0.62	0.61	0.64	0.11
Na (M2)	0.01	0.85	0.02	0.02	0.86	0.86	0.87	0.71	0.02	0.02	0.02	0.02	0.76
Ca (M2)	0.00	0.09	0.00	0.00	0.08	0.09	0.09	0.08	0.00	0.00	0.00	0.00	0.07
Sum	4.00	4.00	4.00	4.00	4.00	4.00	4.00	4.00	4.00	4.00	4.00	4.00	4.00
Xwo	0.71	47.01	1.00	0.80	49.79	50.10	51.05	41.38	1.16	1.04	1.14	1.07	41.87
XEn	61.75	36.63	62.52	61.34	35.38	34.32	34.20	38.06	62.99	63.49	61.95	63.50	37.87
XFs	37.54	16.36	36.48	37.86	14.83	15.59	14.75	20.56	35.86	35.46	36.92	35.43	20.26

Sample	ISD13-06					ISD13-7A2						HIL13-19	
#	22	25	34	35	40	43	68	72	73	88	89	3	61
mineral	cpx	cpx	cpx	cpx	cpx	diopside	cpx	pigeonite	cpx	hyperthsene	cpx	cpx	
SiO_2	50.32	50.54	48.61	48.98	49.28	53.30	50.53	52.69	49.98	51.69	50.00	45.00	45.85
Al_2O_3	5.33	5.29	5.72	5.69	6.75	1.64	5.62	4.36	6.16	3.60	6.05	11.49	10.26
TiO_2		0.36	0.52	0.55	0.90	0.09	0.53	0.06	0.69	0.04	0.65	1.60	1.76
Cr_2O_3		0.06	0.07	0.05	0.00	0.01	0.03	0.00	0.06	0.00	0.02	0.00	0.02
FeO	10.59	8.56	8.77	9.33	8.95	5.87	8.27	15.60	7.60	19.83	7.94	8.13	7.92
MnO	0.06	0.05	0.07	0.11	0.11	0.09	0.08	0.32	0.03	0.12	0.09	0.08	0.05
MgO	10.85	11.30	10.71	11.26	11.89	14.54	13.78	19.73	12.30	23.26	11.99	10.13	10.50
CaO	20.15	20.80	20.87	21.38	21.14	23.48	19.28	3.61	21.74	0.30	21.77	21.33	22.03
Na_2O	2.17	1.99	1.67	1.41	1.37	0.93	0.89	0.35	0.96	0.01	1.39	1.26	1.14
K_2O	0.00	0.01	0.00	0.00	0.00	0.01	0.00	0.16	0.01	0.01	0.01	0.01	0.00
Total	99.49	98.95	97.00	98.75	100.38	99.96	99.02	96.89	99.53	98.83	99.92	99.04	99.51
Si^{4+} (T)	1.87	1.88	1.86	1.84	1.82	1.96	1.88	2.00	1.86	1.92	1.85	1.68	1.71
Al^{IV} (T)	0.13	0.12	0.14	0.16	0.18	0.04	0.12	0.00	0.14	0.08	0.15	0.32	0.29
Ti (M1)	0.00	0.01	0.01	0.02	0.02	0.00	0.01	0.00	0.02	0.00	0.02	0.05	0.05
Al^{VI} (M1)	0.11	0.12	0.11	0.09	0.11	0.03	0.13	0.20	0.13	0.08	0.11	0.19	0.16
Cr (M1)	0.00	0.00	0.00	0.00	0.00	0.00	0.00	0.00	0.00	0.00	0.00	0.00	0.00
Fe^{3+} (M1)	0.18	0.12	0.12	0.14	0.12	0.08	0.03	0.00	0.05	0.00	0.10	0.13	0.12
Fe^{2+} (M1)	0.14	0.14	0.15	0.15	0.14	0.10	0.19	0.25	0.18	0.30	0.13	0.01	0.12
Mg (M1)	0.57	0.61	0.59	0.60	0.60	0.79	0.64	0.55	0.63	0.62	0.63	0.04	0.55
Fe^{2+} (M2)	0.01	0.00	0.00	0.01	0.01	0.00	0.04	0.25	0.01	0.32	0.01	0.11	0.01
Mn (M2)	0.00	0.00	0.00	0.00	0.00	0.00	0.00	0.01	0.00	0.00	0.00	0.00	0.00
Mg (M2)	0.03	0.02	0.02	0.03	0.05	0.01	0.13	0.57	0.05	0.67	0.03	0.52	0.03
Na (M2)	0.80	0.83	0.85	0.86	0.83	0.92	0.77	0.15	0.87	0.01	0.86	0.09	0.88
Ca (M2)	0.16	0.14	0.12	0.10	0.10	0.07	0.06	0.03	0.07	0.00	0.10	0.85	0.08
Sum	4.00	4.00	4.00	4.00	4.00	4.00	4.00	4.00	4.00	4.00	4.00	4.00	4.00
Xwo	46.32	48.15	48.98	48.23	47.32	48.63	42.93	8.34	48.54	0.62	48.76	51.07	51.45
XEn	34.68	36.39	34.96	35.33	37.04	41.89	42.68	63.49	38.21	67.23	37.36	33.73	34.11
XFs	19.00	15.46	16.06	16.43	15.64	9.48	14.38	28.17	13.25	32.15	13.88	15.20	14.44

TABLE A.8: Pyroxene EMP analyses showing concentrations of nickel and copper and their respective standard deviations in ppm. Points were taken at a consistent distance apart (X, in microns) for each crystal.

HILL13-19 cpx

Line	x (μm)	Ni	STD	Cu	STD
1	0	350	58	14	54
1	56	369	58	48	54
1	112	367	58	30	54
1	169	358	58	13	55
1	225	376	58	30	54
1	281	354	58	17	55
1	337	391	58	2	54
1	393	353	58	-1	54
1	450	387	58	33	55
1	506	387	58	25	55
1	562	347	58	35	54
1	618	367	58	25	54
1	675	384	58	42	55
1	731	363	58	32	54
1	787	391	58	-4	54
1	843	376	58	28	54
1	899	378	58	58	54
1	956	338	58	64	54
1	1012	378	58	33	54
1	1068	331	58	1	54

AK72-98II opx-1

Line	x (μm)	Ni	STD	Cu	STD
2	0	825	58	4	55
2	22	862	58	38	55
2	43	816	59	-5	55
2	65	843	58	2	55
2	86	878	59	5	55
2	108	816	58	1	55
2	129	872	58	-16	55
2	151	874	58	24	55
2	172	867	58	-10	55
2	194	828	58	-21	55

AK72-98II am rim around opx-1

Line	x (μm)	Ni	STD	Cu	STD
3	0	434	58	-6	54
3	6	469	58	14	54
3	12	483	58	-47	55
3	17	501	58	10	54
3	23	514	58	-5	54

AK72-98II opx-2 with am rim

Line	x (μm)	Ni	STD	Cu	STD
4	0	702	57	-20	54
4	28	757	57	-9	54
4	55	799	58	42	54
4	83	839	58	-19	55
4	110	802	58	-7	55
4	138	815	58	8	55
4	166	826	57	161	54
4	193	819	58	-27	55
4	221	833	58	17	55
4	248	824	58	-10	55
4	276	819	58	11	54
4	304	798	58	23	54
4	331	740	58	23	54
4	359	781	58	47	55
4	386	562	57	5	53

AK72-98II cpx-1

Line	x (μm)	Ni	STD	Cu	STD
5	0	536	58	-28	55
5	21	485	59	6	55
5	42	537	59	65	55
5	63	591	58	184	55
5	85	539	59	25	55
5	106	599	59	17	55
5	127	523	59	-1	55
5	148	519	59	9	55
5	169	529	59	0	54
5	190	614	59	-6	55
5	212	493	59	8	55
5	233	534	59	36	55
5	254	483	59	-16	55
5	275	613	59	-4	55
5	296	478	59	7	55
5	317	462	59	-10	55
5	339	483	59	4	55
5	360	485	59	25	55
5	381	494	59	12	55
5	402	525	59	13	55

AK72-98II cpx-2

Line	x (μm)	Ni	STD	Cu	STD
6	0	491	58	-13	54
6	27	527	58	39	54
6	55	544	58	-3	54
6	82	508	58	8	54
6	110	524	58	-12	55
6	137	539	58	23	55
6	165	523	58	4	54
6	192	551	58	28	54
6	220	541	58	-9	55
6	247	566	58	8	54

HIL13-18A cpx

Line	x (μm)	Ni	STD	Cu	STD
7	0	162	59	34	54
7	51	137	59	20	54
7	101	148	59	19	54
7	152	166	59	20	55
7	203	133	59	44	54
7	253	132	59	16	55
7	304	165	59	108	54
7	355	126	59	34	54
7	405	138	59	-2	55
7	456	155	59	-13	55
7	507	128	59	20	54
7	557	125	59	41	54
7	608	149	59	36	55
7	659	130	59	26	54
7	709	134	59	132	54
7	760	128	59	8	54

HIL14-03 opx

Line	x (μm)	Ni	STD	Cu	STD
8	0	49	59	42	55
8	75	65	59	22	54
8	150	24	59	33	55
8	225	102	58	256	54
8	300	52	59	48	54
8	375	28	59	31	54
8	449	42	59	24	55
8	524	56	59	84	55
8	599	80	58	7	55
8	674	103	57	242	52
8	749	42	59	40	54
8	824	66	59	41	54
8	899	39	59	57	55
8	974	50	58	10	54
8	1049	40	59	26	54
8	1124	22	59	41	54
8	1198	53	59	19	54
8	1273	66	59	26	54
8	1348	54	59	27	55
8	1423	63	59	32	55

TABLE A.9: Amphibole EMP analyses from granulite and amphibolite samples, inside veins and wallrock. Amphibole is normalised to 13 cations, excluding the A and M4 sites.

Sample	HIL13-15A		HIL13-17	HIL13-18A	HIL13-18B		HIL13-19			AK72-98II				ISD13-01A		ISD13-01B			ISD13-06		
#	47	49	6	42	32	38	6	8	9	10	13	16	17	3	4	23	25	21	26	33	39
	front		in vein	front	front		granulite	opx rim	w. qtz	w. sul	in pl	opx rim	w. qtz	in vein		edge	in vein		mafic		wall
SiO_2	48.85	40.54	44.58	41.88	48.64	52.86	49.44	50.74	51.71	42.18	42.05	55.00	50.91	49.09	41.86	40.80	41.45	43.20	43.25	48.76	44.41
Al_2O_3	8.78	19.60	13.50	14.35	7.19	7.31	8.28	5.82	5.67	15.63	16.14	1.27	6.85	7.49	14.19	16.53	16.68	13.88	11.65	7.69	10.70
TiO_2	0.62	0.04		2.10	0.36	0.45	0.73	0.22	0.10	0.08	0.17	0.05	0.12	0.47	0.81	0.61	0.50		0.74	0.56	2.08
Cr_2O_3	0.01	0.07	0.01	0.01	0.01	0.01	0.00	0.00	0.05	0.00	0.00	0.00	0.00	0.03	0.02	0.01	0.00		0.00	0.09	0.01
FeO	9.55	12.55	11.41	11.08	11.99	10.60	9.51	16.11	10.80	14.04	12.53	18.90	10.51	11.24	14.45	15.61	15.04	14.63	15.37	11.39	9.29
MnO	0.13	0.18	0.17	0.11	0.15	0.10	0.00	0.19	0.07	0.10	0.08	0.30	0.12	0.05	0.08	0.14	0.16	0.26	0.00	0.01	0.02
MgO	15.74	10.47	13.01	11.89	14.46	13.51	14.67	17.43	17.04	11.07	11.19	20.49	16.87	14.76	10.57	8.86	9.03	10.74	11.41	15.49	13.94
CaO	12.80	11.85	12.04	12.52	12.70	11.40	12.77	5.51	11.47	11.55	11.27	1.05	11.22	12.60	12.04	11.26	11.73	11.46	11.46	12.23	12.26
Na_2O	1.00	1.94	1.42	0.97	0.78	0.70	0.52	0.87	0.76	1.88	1.94	0.11	1.02	0.68	1.07	1.70	1.75	1.85	1.95	1.05	1.02
K_2O	0.50	0.71	0.48	2.31	0.77	0.76	0.83	0.24	0.16	0.71	0.79	0.02	0.21	0.40	1.66	0.79	0.52	0.32	0.80	0.60	1.89
Total	97.97	97.95	96.72	97.22	97.05	97.71	96.75	97.13	97.82	97.23	96.15	97.19	97.84	96.82	96.75	96.30	96.85	96.46	96.62	97.88	95.62
Si^{4+}	6.98	5.93	6.53	6.23	7.10	7.56	7.17	7.37	7.37	6.24	6.28	7.90	7.26	7.13	6.28	6.17	6.20	7.08	6.51	7.03	6.64
Al^{IV}	1.02	2.07	1.47	1.77	0.90	0.44	0.83	0.63	0.63	1.76	1.72	0.10	0.74	0.87	1.72	1.83	1.80	0.92	1.49	0.97	1.36
Al^{VI}	0.46	1.31	0.86	0.74	0.34	0.79	0.59	0.37	0.32	0.97	1.11	0.11	0.42	0.42	0.79	1.12	1.15	0.42	0.58	0.34	0.53
Ti	0.07	0.00		0.24	0.04	0.05	0.08	0.02	0.01	0.01	0.02	0.01	0.01	0.05	0.09	0.07	0.06		0.08	0.06	0.23
Fe^{3+}	0.05	0.08	0.13	0.00	0.11	0.00	0.00	0.00	0.05	0.10	0.00	0.01	0.00	0.08	0.13	0.00	0.00	0.08	0.02	0.10	0.00
Fe^{2+}	1.07	1.33	1.17	1.38	1.35	1.27	1.15	0.84	1.00	1.48	1.38	0.49	0.98	1.25	1.63	1.82	1.78	1.27	1.76	1.17	1.13
Mg	3.35	2.28	2.84	2.63	3.15	2.88	3.17	3.77	3.62	2.44	2.49	4.39	3.59	0.01	0.01	0.02	0.02	3.23	2.56	3.33	3.11
Mn	0.02	0.02	0.01	0.01	0.02	0.01	0.00	0.02	0.01	0.01	0.01	0.04	0.01	3.20	2.36	2.00	2.01	0.00	0.00	0.00	0.00
Fe^{2+}	0.02	0.12	0.10	0.00	0.00	0.00	0.00	1.12	0.24	0.16	0.19	1.77	0.27	0.03	0.05	0.16	0.10	0.12	0.15	0.11	0.03
Ca_{M4}	1.96	1.86	1.89	1.99	1.98	1.75	1.99	0.86	1.75	1.83	1.80	0.16	1.72	1.96	1.94	1.83	1.88	1.88	1.85	1.89	1.97
Na_{M4}						0.19															
Ca_A					0.01																
Na_A	0.28	0.55	0.40	0.28	0.22		0.15	0.24	0.21	0.54	0.56	0.03	0.28	0.19	0.31	0.50	0.51	0.36	0.57	0.29	0.30
K	0.09	0.13	0.09	0.44	0.14	0.14	0.15	0.05	0.03	0.13	0.15	0.00	0.04	0.07	0.32	0.15	0.10	0.06	0.15	0.11	0.36
Sum	15.37	15.68	15.49	15.71	15.36	15.08	15.28	15.29	15.24	15.67	15.71	15.00	15.32	15.26	15.63	15.65	15.61	15.42	15.72	15.40	15.66

Sample	ISD13-04						ISD13-07A2						ISD13-07B						
#	2	3	6	7	11	13	44	69	71	85	86	87	2	4	12	16	20	23	24
	dark	light		light	dark		in vein						in vein				wall	edge	wall
SiO_2	53.06	46.88	43.94	42.76	49.78	43.20	51.80	49.50	53.39	41.03	51.36	50.80	57.03	45.70	48.04	46.34	40.04	44.72	41.87
Al_2O_3	3.53	9.59	13.14	13.18	6.16	13.88	6.37	8.40	4.67	16.65	5.68	5.58	1.31	13.72	11.38	13.05	19.71	15.04	17.46
TiO_2							0.49	0.47	0.06	0.28	0.27	0.15	0.04	0.62	0.43	0.62	0.15	0.49	0.34
Cr_2O_3							0.02	0.00	0.01	0.00	0.01	0.00	0.02	0.00	0.03	0.00	0.00	0.00	0.02
FeO	10.30	13.19	14.64	14.31	11.26	14.63	6.06	9.32	7.53	12.39	7.94	15.48	6.30	9.62	8.52	9.20	13.33	10.68	12.80
MnO	0.24	0.21	0.16	0.25	0.23	0.26	0.08	0.03	0.08	0.08	0.07	0.30	0.09	0.10	0.09	0.09	0.23	0.16	0.16
MgO	17.30	13.22	10.95	10.70	15.28	10.74	18.79	15.77	18.41	11.46	17.98	19.88	20.17	13.54	15.29	14.27	9.50	12.53	10.56
CaO	12.27	11.65	11.65	11.72	12.21	11.46	13.17	13.15	12.56	12.18	13.12	2.48	13.34	11.66	12.19	11.97	11.61	11.95	11.64
Na_2O	0.55	1.39	1.68	1.75	0.82	1.85	0.52	0.56	0.42	1.33	0.54	0.60	0.09	1.52	1.13	1.37	1.82	1.41	1.58
K_2O	0.06	0.16	0.35	0.32	0.29	0.32	0.47	0.61	0.25	1.47	0.24	1.16	0.02	0.51	0.25	0.47	0.66	0.41	0.53
Total	97.34	96.33	96.59	95.09	96.07	96.46	97.77	97.78	97.38	96.87	97.21	96.40	98.42	96.97	97.35	97.35	97.04	97.37	96.95
Si^{4+}	7.58	6.92	6.55	6.48	7.28	6.46	7.27	7.07	7.54	6.07	7.28	7.37	7.89	6.55	6.86	6.65	5.93	6.47	6.17
Al^{IV}	0.42	1.08	1.45	1.52	0.72	1.54	0.73	0.93	0.46	1.93	0.72	0.63	0.11	1.45	1.14	1.35	2.07	1.53	1.83
Al^{VI}	0.18	0.58	0.86	0.83	0.34	0.91	0.32	0.48	0.32	0.97	0.23	0.32	0.10	0.87	0.77	0.86	1.37	1.04	1.20
Ti							0.05	0.05	0.01	0.03	0.03	0.02	0.00	0.07	0.05	0.07	0.02	0.05	0.04
Fe^{3+}	0.08	0.08	0.04	0.11	0.08	0.04	0.08	0.07	0.00	0.24	0.24	0.00	0.00	0.34	0.00	0.00	0.03	0.00	0.00
Fe^{2+}	1.06	1.43	1.67	1.63	1.25	1.66	0.61	1.05	0.80	1.23	0.70	0.36	0.73	0.81	0.93	1.02	1.48	1.21	1.44
Mg	3.68	2.91	2.43	2.43	3.33	2.39	3.93	3.35	3.87	2.53	3.80	4.30	4.16	2.90	3.25	3.05	2.10	2.70	2.32
Mn	0.03	0.03	0.02	0.03	0.03	0.03	0.01	0.00	0.01	0.01	0.01	0.04	0.01	0.01	0.01	0.01	0.03	0.02	0.02
Fe^{2+}	0.09	0.14	0.12	0.07	0.05	0.13	0.02	0.00	0.09	0.60	0.00	1.52	0.00	0.00	0.09	0.08	0.14	0.08	0.14
Ca_{M4}	1.88	1.84	1.86	1.90	1.92	1.84	1.98	2.00	1.90	1.92	1.99	0.39	1.98	1.79	0.04	1.84	1.83	1.85	1.84
Na_{M4}												0.05	0.02	0.21	1.86	0.07		0.05	
Ca_A								0.01											
Na_A	0.15	0.40	0.48	0.51	0.23	0.54	0.14	0.16	0.11	0.38	0.15	0.12	0.00	0.21	0.27	0.31	0.52	0.34	0.45
K	0.01	0.03	0.07	0.06	0.05	0.06	0.08	0.11	0.05	0.28	0.04	0.21	0.00	0.09	0.05	0.09	0.13	0.08	0.10
Sum	15.16	15.44	15.55	15.57	15.28	15.60	15.22	15.28	15.16	16.19	15.19	15.33	15.00	15.30	15.32	15.40	15.65	15.42	15.55

TABLE A.10: Muscovite, chlorite and biotite EMP analyses from granulite and amphibolite samples. Values are presented in oxide weight percent. Muscovite and biotite are normalised to 22 oxygens. The chlorite formula is based on 36 oxygens.

Sample	HIL13-16	HIL13-16	HIL13-18B		ISD13-07B		HIL13-15A	HIL13-19		ISD13-01A	
#	4	7	31	39	5	19	40	50	54	9	11
mineral	muscovite	chlorite	chlorite		chlorite		biotite	biotite		biotite	
SiO_2	45.50	27.16	29.90	28.45	28.54	26.49	36.19	36.33	35.73	37.08	36.44
Al_2O_3	33.35	19.29	19.23	18.60	20.67	22.27	16.53	17.41	16.78	17.13	18.71
TiO_2	0.57	0.05	0.00	0.01	0.03	0.07	3.13	2.21	2.63	2.07	1.73
Cr_2O_3	0.02	0.00	0.00	0.00	0.02	0.04	0.03	0.01	0.04	0.02	0.01
FeO	2.25	19.72	15.03	16.42	11.45	15.36	17.32	14.56	15.54	14.73	15.08
MnO	0.02	0.04	0.22	0.21	0.11	0.11	0.12	0.00	0.00	0.01	0.02
MgO	1.40	19.09	23.25	21.94	24.64	21.33	11.44	14.01	12.78	13.94	12.93
CaO	0.00	0.06	0.14	0.06	0.09	0.11	0.03	0.04	0.27	0.00	0.00
Na_2O	0.33	0.01	0.00	0.00	0.00	0.04	0.05	0.07	0.08	0.09	0.19
K_2O	10.57	0.00	0.00	0.03	0.01	0.03	9.60	9.95	9.22	9.07	9.04
Total	93.99	85.39	87.70	85.72	85.53	85.84	94.43	94.58	93.07	94.14	94.14
Si^{4+}	6.18	5.69	5.91	5.83	5.69	5.39	5.52	5.46	5.48	5.57	5.47
Al^{IV}	1.82	2.31	2.09	2.17	2.31	2.61	2.48	2.54	2.52	2.43	2.53
Al^{VI}	3.53	2.45	2.40	2.32	2.56	2.74	0.50	0.55	0.51	0.60	0.79
Ti	0.06	0.01	0.00	0.00	0.00	0.01	0.36	0.25	0.30	0.23	0.20
Cr	0.00	0.00					0.00	0.00	0.00	0.00	0.00
Fe^{3+}		0.08	0.18	0.08	0.14	0.07					
Fe^{2+}	0.26	3.37	2.31	2.73	1.77	2.54	2.21	1.83	1.99	1.85	1.90
Mn	0.00	0.01	0.04	0.04	0.02	0.02	0.01	0.00	0.00	0.00	0.00
Mg	0.28	5.96	6.85	6.70	7.32	6.47	2.60	3.14	2.92	3.12	2.90
Ca	0.00	0.01	0.03	0.01	0.02	0.02	0.00	0.01	0.04	0.00	0.00
Na	0.09	0.01	0.00	0.00	0.00	0.03	0.01	0.02	0.03	0.03	0.06
K	1.83	0.00	0.00	0.02	0.00	0.02	1.87	1.91	1.80	1.74	1.73
Fe/Fe+Mg	0.24	0.37	0.27	0.30	0.21	0.29	0.46	0.37	0.41	0.37	0.40

TABLE A.11: Pyrite EMP analyses from sulphide-bearing samples. Values are presented in weight percent.

Sample	HIL13-03							HIL13-18B		
#	24	25	26	28	29	30	31	17	33	34
mineral	pyrite							pyrite		
Si	0.02	0.03	0.01	0.05	0.23	0.09	0.01	0.00	0.01	0.02
Fe	47.24	46.86	44.16	46.74	46.16	46.92	46.99	47.15	47.06	47.13
Ni	0.07	0.22	0.03	0.01	0.07	0.00	0.06	0.25	0.06	0.00
Zn	0.00	0.04	0.03	0.02	0.00	0.00	0.00	0.01	0.00	0.04
S	52.32	51.71	52.65	51.21	51.13	51.69	51.87	53.62	53.15	52.91
Cu	0.00	0.02	0.23	0.00	0.11	0.11	0.03	0.00	0.00	0.05
Ag	0.04	0.01	0.00	0.04	0.02	0.05	0.00	0.01	0.01	0.02
Co	0.02	0.14	3.12	0.00	0.00	0.00	0.00	0.00	0.00	0.00
Total	99.66	99.02	100.21	98.02	97.65	98.73	98.86	100.98	100.22	100.13

Sample	HIL13-17							
#	2	5	7	9	12	13	14	15
mineral	pyrite							
Si	0.05	0.00	0.01	0.01	0.04	0.00	0.04	0.00
Fe	46.77	46.71	46.00	46.75	46.35	46.72	46.75	47.06
Ni	0.13	0.20	0.73	0.32	0.00	0.09	0.02	0.12
Zn	0.00	0.00	0.00	0.01	0.00	0.07	0.08	0.03
S	52.82	53.48	53.27	53.22	54.03	54.29	55.13	53.57
Cu	0.06	0.02	0.06	0.04	0.03	0.03	0.03	0.02
Ag	0.00	0.03	0.00	0.01	0.06	0.02	0.01	0.03
Co	0.04	0.15	0.02	0.03	0.01	0.02	0.09	0.16
Total	99.86	100.59	100.06	100.41	100.42	101.24	102.15	100.99

Sample	ISD13-06		ISD13-07A2				AK72-98II	
#	19	30	35	42	64	66	24	32
mineral	pyrite		pyrite				pyrite	
Si	0.00	0.03	0.00	0.05	0.00	0.02	0.38	0.01
Fe	46.37	45.81	46.37	45.83	46.97	45.28	46.05	45.39
Ni	0.00	0.02	0.91	0.22	0.08	0.61	0.13	0.36
Zn	0.00	0.00	0.01	0.00	0.00	0.05	0.00	0.00
S	52.85	51.48	52.60	53.13	52.77	53.76	51.22	52.74
Cu	0.04	0.07	0.04	0.01	0.02	0.01	0.03	0.16
Ag			0.00	0.00				
Co			0.11	0.65				
Total	99.17	97.36	100.02	99.85	99.78	99.72	97.79	98.65

TABLE A.12: Results of EMP analyses of Fe, Cu and Ni sulphides within the study area. Values are presented in weight percent.

Sample	HIL13-03		HIL13-17		HIL13-18B	ISD13-06		ISD13-07A2		AK72-98II
#	23	3	6	11	16	16	27	36	62	30
mineral	chalcopyrite		chalcopyrite		chalcopyrite	chalcopyrite		chalcopyrite		cubanite
Si	0.01	0.01	0.02	0.01	0.01	0.00	0.00	0.00	0.03	0.01
Fe	29.99	29.88	29.91	28.97	30.12	29.80	30.05	29.74	25.99	34.49
Ni	0.04	0.00	0.00	0.04	0.02	0.03	0.04	0.04	9.31	0.37
Zn	0.08	0.09	0.04	0.03	0.05	0.20	0.05	0.00	0.02	0.02
S	34.52	33.73	35.17	35.09	34.51	34.16	34.61	34.28	35.23	41.22
Cu	33.87	33.58	33.31	33.25	33.13	33.34	34.19	33.54	26.76	20.96
Ag	0.01	0.01	0.00	0.00	0.01			0.01		
Co	0.00	0.00	0.00	0.00	0.00			0.00		
Total	98.50	97.26	98.36	97.27	97.82	97.51	98.95	97.54	97.35	97.08

Sample	ISD13-06		ISD13-07A2			AK72-98II		HIL13-17		
#	17	28	38	41	83	29	31	1	4	8
mineral	pentlandite		pentlandite			pentlandite		millerite		
Si	0.02	0.00	0.00	0.00	0.01	0.00	0.01	0.00	0.00	0.00
Fe	26.29	27.44	29.23	29.36	27.47	28.78	28.88	0.59	0.75	0.53
Ni	35.87	35.77	37.06	36.35	38.44	36.06	36.63	63.35	63.57	63.69
Zn	0.00	0.04	0.00	0.00	0.03	0.00	0.06	0.05	0.10	0.04
S	32.45	32.63	32.71	32.19	32.73	32.46	32.71	35.85	35.66	35.84
Cu	0.17	0.00	0.04	0.00	0.00	0.02	0.00	0.00	0.00	0.00
Ag			0.00	0.06				0.00	0.01	0.00
Co			0.02	0.09				0.00	0.00	0.00
Total	94.79	95.88	99.00	98.01	98.62	97.32	98.24	99.76	100.09	100.03

Sample	HIL13-18B		HIL13-18B		ISD13-06		ISD13-07A2		AK72-98II	
#	18	19	21	22	18	29	37	39	26	33
mineral	millerite		violarite		pyrrhotite		pyrrhotite		pyrrhotite	
Si	0.02	0.01	0.26	0.15	0.00	0.02	0.00	0.01	0.19	0.02
Fe	0.60	0.42	12.88	8.27	57.79	58.60	58.97	59.32	56.69	59.36
Ni	62.48	63.60	42.81	49.43	1.10	0.98	0.53	0.62	0.89	0.48
Zn	0.00	0.04	0.06	0.01	0.00	0.04	0.00	0.00	0.00	0.01
S	35.36	35.13	41.67	39.05	39.78	39.36	39.60	39.07	38.40	39.44
Cu	0.00	0.00	0.05	0.00	0.05	0.13	0.00	0.01	0.03	0.00
Ag	0.00	0.05	0.00	0.00			0.06	0.02		
Co	0.05	0.11	0.02	0.02			0.00	0.00		
Total	98.39	99.32	97.69	96.85	98.72	99.12	99.08	98.93	96.17	99.30

Bibliography

Alexander, C. D. O., Hutchison, R., Graham, A. L., and Yabuki, H. (1987). Discovery of scapolite in the Bishunpur (LL3) chondritic meteorite. *Mineralogical Magazine*, 51:733–735.

Austrheim, H. (1978). *The metamorphic evolutions of the granulite-facies rocks of Radøy, with special emaphasis on the rocks of the Mangerite Complex*. Cand. real. thesis, University of Bergen.

Austrheim, H. (1987). Eclogitization of lower crustal granulites by fluid migration through shear zones. *Earth and Planetary Science Letters*, 81:221–232.

Austrheim, H. (1990). The granulite-eclogite facies transition: A comparison of experimental work and a natural occurrence in the Bergen Arcs, western Norway. *Lithos*, 25:163–169.

Austrheim, H., Corfu, F., Bryhni, I., and Andersen, T. B. (2003). The Proterozoic Hustad igneous complex: a low strain enclave with a key to the history of the Western Gneiss Region of Norway. *Precambrian Research*, 120:149–175.

Austrheim, H. and Griffin, W. L. (1985). Shear defomation and eclogite formation within granulite-facies anorthosites of the Bergen Arcs, western Norway. *Chemical Geology*, 50:267–281.

Austrheim, H., Putnis, C. V., Engvik, A. K., and Putnis, A. (2008). Zircon coronas around Fe–Ti oxides: a physical reference frame for metamorphic and metasomatic reactions. *Contributions to Mineralogy and Petrology*, 156:517–527.

Barnes, S.-J. and Francis, D. (1995). The Distribution of Platinum-Group Elements, Nickel, Copper, and Gold in the Muskox Layered Intrusion, Northwest Territories, Canada. *Economic Geology*, 90:135–154.

Bickle, M. J. and Mckenzie, D. (1987). The transport of heat and matter by fluids during metamorphism. *Contributions to Mineralogy and Petrology*, 95:384–392.

Bingen, B., Davis, W. J., and Austrheim, H. (2001). Zircon U-Pb geochronology in the Bergen arc eclogites and their Proterozoic protoliths, and implications for the pre-Scandian evolution of the Caledonides in western Norway. *Geological Society of America Bulletin*, 113:640–649.

Bjørlykke, H. (1949). Hosanger Nikkelgruve, rapport nr. 172. Technical report, Norges Geologiske Undersøkelse.

Blattner, P. and Black, P. M. (1980). Apatite and Scapolite as Petrogenetic Indicators in Granolites of Milford Sound, New Zealand. *Contributions to Mineralogy and Petrology*, 74:339–348.

Boivin, P. and Camus, G. (1981). Igneous Scapolite-Bearing Associations in the Chaîne des Puys, Massif Central (France) and Atakor (Hoggar, Algeria). *Contributions to Mineralogy and Petrology*, 77:365–375.

Boomeri, M., Mizuta, T., Nakashima, K., Ishiyama, D., and Ishikawa, Y. (1997). Geochemical characteristics of halogen-bearing hastingsite, scapolite and phlogopite from the Sangan iron skarn deposits, northeastern Iran. *Journal of Mineralogy, Petrology and Economic Geology*, 92(12):481–501.

Boundy, T. M., Donohue, C. L., Essene, E. J., Mezger, K., and Austrheim, H. (2002). Discovery of eclogite facies carbonate rocks from the Lindås Nappe, Caledonides, Western Norway. *Journal of Metamorphic Geology*, 20:649–667.

Boundy, T. M., Fountain, D. M., and Austrheim, H. (1992). Structural development and petrofabrics of eclogite facies shear zones, Bergen Arcs, western Norway: implications for deep crustal deformational processes. *Journal of Metamorphic Geology*, 10:127–146.

Boundy, T. M., Mezger, K., and Essene, E. J. (1997). Temporal and tectonic evolution of the granulite-eclogite association from the Bergen Arcs, western Norway. *Lithos*, 39:159–178.

Camacho, A., Lee, J. K. W., Hensen, B. J., and Braun, J. (2005). Short-lived orogenic cycles and the eclogitization of cold crust by spasmodic hot fluids. *Nature*, 435:1191–1196.

Caquineau, T. (2012). Sulfur-rich scapolite from the Western Gneiss Region and the Bergen Arcs, Norway: implications for sulfides formation and the sulfur budget. Technical report, University of Oslo.

Chappell, B. W. and White, A. J. R. (1968). The X-ray spectrographic determination of sulphur co-ordination in scapolite. *American Mineralogist*, 53:1735–1738.

Cohen, A. S., O'Nions, R. K., Siegenthaler, R., and Griffin, W. L. (1988). Chronology of the pressure-temperature history recorded by a granulite terrain. *Contributions to Mineralogy and Petrology*, 98:303–311.

Coolen, J. J. M. M. M. (1980). *Chemical petrology of the Furua granulite complex, southern Tanzania.* Papers of geology, series 1, no. 13, GUA (University of Amsterdam).

Coolen, J. J. M. M. M. (1982). Carbonic fluid inclusions in granulites from Tanzania - a comparison of geobarometric methods based on fluid density and mineral chemistry. *Chemical Geology*, 37:59–77.

Deer, W. A., Howie, R. A., Wise, W. S., and Zussman, J. (2006). *Rock-Forming Minerals. Volume 4B. Framework Silicates - Silica Minerals, Feldspathoids and the Zeolites.* The Geological Society of London.

Edwards, R., Bailey, R., and Garland, G. (1981). Conductivity anomalies: lower crust or asthenosphere? *Physics of the Earth and Planetary Interiors*, 25:263–272.

Ekström, T. K. (1972). Coexisting scapolite and plagioclase from two iron formations in northern Sweden. *Lithos*, 5:175–185.

Engvik, A. K., Golla-Schindler, U., Berndt, J., Austrheim, H., and Putnis, A. (2009). Intragranular replacement of chlorapatite by hydroxy-fluor-apatite during metasomatism. *Lithos*, 112:236–246.

Engvik, A. K., Mezger, K., Wortelkamp, S., Bast, R., Corfu, F., Korneliussen, A., Ihlen, P., Bingen, B., and Austrheim, H. (2011). Metasomatism of gabbro - mineral replacement and element mobilization during the Sveconorwegian metamorphic event. *Journal of Metamorphic Geology*, 29:399–423.

Engvik, A. K., Putnis, A., Fitz Gerald, J. D., and Austrheim, H. (2008). Albitization of Granitic Rocks: the Mechanism of Replacement of Oligoclase by Albite. *The Canadian Mineralogist*, 46:1401–1415.

Evans, B. W., Shaw, D. M., and Haughton, D. R. (1969). Scapolite stoichiometry. *Contributions to Mineralogy and Petrology*, 24:293–305.

Evans, K., Tomkins, A., Cliff, J., and Fiorentini, M. (2014). Insights into subduction zone sulfur recycling from isotopic analysis of eclogite-hosted sulfides. *Chemical Geology*, 365:1–19.

Fasting, H. (1909). Rapport over Espetveit og Grønskarret Kobbergruber, Bergarkivet rapport nr. 416. Technical report, Norges Geologiske Undersøkelse.

Faure, G. and Mensing, T. M. (2005). *Isotopes: Principles and Applications, Third Edition*. John Wiley & Sons, Inc., pp. 824–853.

Fossen, H. (1998). Advances in understanding the post-Caledonian structural evolution of the Bergen area, West Norway. *Norsk Geologisk Tidsskrift*, 78:33–46.

Frietsch, R., Tuisku, P., Martinsson, O., and Perdahl, J.-A. (1997). Early Proterozoic Cu-(Au) and Fe ore deposits associated with regional Na-Cl metasomatism in northern Fennoscandia. *Ore Geology Reviews*, 12(1):1–34.

Glodny, J., Kühn, A., and Austrheim, H. (2008). Geochronology of fluid-induced eclogite and amphibolite facies metamorphic reactions in a subduction–collision system, Bergen Arcs, Norway. *Contributions to Mineralogy and Petrology*, 156(1):27–48.

Goldsmith, J. R. (1976). Scapolites, granulites, and volatiles in the lower crust. *Geological Society of America Bulletin*, 87:161–168.

Haak, V. and Hutton, R. (1986). Electrical resistivity in continental lower crust. In Dawson, J. B., Carswell, D. A., Hall, J., and Wedepohl, K. H., editors, *The Nature of the Lower Continental Crust*, pages 35–49. Geological Society Special Publication No. 24.

Haber, G. (1940). Bericht über Erzvorkommen auf der Insel Radøy nördlich von Bergen, Bergarkivet rapport nr. 1063. Technical report, Norges Geologiske Undersøkelse.

Harley, S. L. and Buick, I. S. (1992). Wollastonite-Scapolite Assemblages as Indicators of Granulite Pressure-Temperature-Fluid Histories: The Rauer Group, East Antarctica. *Journal of Petrology*, 33(3):693–728.

Hoefs, J. (2009). *Stable Isotope Geochemistry*. Springer, pp. 71–73, 111–136.

Hoefs, J., Coolen, J., and Touret, J. (1981). The Sulfur and Carbon Isotope Composition of Scapolite-Rich Granulites from Southern Tanzania. *Contributions to Mineralogy and Petrology*, 78:332–336.

Jiang, S.-Y., Palmer, M. R., Xue, C.-J., and Li, Y.-H. (1994). Halogen-rich scapolite-biotite rocks from the Tongmugou Pb-Zn deposit, Qinling, north-western China: implications for the ore-forming processes. *Mineralogical Magazine*, 58:543–552.

Kolderup, C. F. and Kolderup, N. H. (1940). Geology of the Bergen Arcs system. *Bergens Museums Skrifter*, 20:1–137.

Kühn, A. (2002). *The influence of fluid on the granulite to eclogite and amphibolite facies transition: a study in the anorthositic rocks from the Lindås Nappe, Bergen Arcs, West Norway.* Doctoral dissertation, Univeristy of Oslo.

Kwak, T. A. P. (1977). Scapolite compositional change in a metamorphic gradient and its bearing on the identification of meta-evaporite sequences. *Geologiical Magazine*, 114(5):343–354.

Lovering, J. F. and White, A. J. R. (1964). The Significance of Primary Scapolite in Granulitic Inclusions from Deep-seated Pipes. *Journal of Petrology*, 5(2):195–218.

Lovering, J. F. and Widdowson, J. R. (1968). Electron microprobe determination of sulphur coordination in minerals. *Lithos*, 1:264–267.

Lowell, G. R. L. and Noll Jr, P. D. (2001). Fe-Cu-Au-bearing scapolite skarn in moat sediments of the Taum Sauk Caldera, southeastern Missouri, USA. *Mineralogical Magazine*, 65(3):373–396.

Mattey, D., Jackson, D., Harris, B., and Kelley, S. (1994). Isotopic constraints on fluid infiltration from an eclogite facies shear zone, Holsenøy, Norway. *Journal of Metamorphic Geology*, 12:311–325.

Moecher, D. P., Essene, E. J., and Valley, J. W. (1992). Stable isotopic and petrological constraints on scapolitization of the Whitestone meta-anorthosite, Grenville Province, Ontario. *Journal of Metamorphic Geology*, 10:745–762.

Moecher, D. P., Valley, J. W., and Essene, E. J. (1994). Extraction and carbon isotope analysis of CO_2 from scapolite in deep crustal granulites and xenoliths. *Geochimica et Cosmochimica Acta*, 58(2):959–967.

Morisset, C.-E. and Scoates, J. S. (2008). Origin of zircon rims around ilmenite in mafic plutonic rocks of Proterozoic anorthosite suites. *The Canadian Mineralogist*, 46:289–304.

Mukai, H., Austrheim, H., Putnis, C. V., and Putnis, A. (2014). Textural Evolution of Plagioclase Feldspar across a Shear Zone: Implications for Deformation Mechanism and Rock Strength. *Journal of Petrology*, 55(8):1457–1477.

Naldrett, A. J. (1989). *Magmatic Sulphide Deposits*. Oxford Monographs on Geology and Geophysics. Clarendon Press.

Newton, R. C. and Goldsmith, J. R. (1975). Stability of the Scapolite Meionite ($3CaAl_2S_2O_2$ * $CaCO_3$) at High Pressures and Storage of CO_2 in the Deep Crust. *Contributions to Mineralogy and Petrology*, 49:49–62.

Newton, R. C. and Manning, C. E. (2004). Solubility of Anhydrite, $CaSO_4$, in NaCl-H_2O Solutions at High Pressures and Temperatures: Applications to Fluid-Rock Interaction. *Journal of Petrology*, 46(4):701–716.

Ohmoto, H. (1972). Systematics of Sulfur and Carbon Isotopes in Hydrothermal Ore Deposits. *Economic Geology*, 67:551–578.

Okrusch, M., Schröder, B., and Schnütgen, A. (1979). Granulite-facies metabasic ejecta in the Laacher See area, Eifel, West Germany. *Lithos*, 12:251–270.

Pan, Y., Fleet, M. E., and Ray, G. E. (1994). Scapolite in two Canadian gold deposits: Nickel Plate, British Columbia and Hemlo, Ontario. *The Canadian Mineralogist*, 32:825–837.

Putnis, A. (2002). Mineral replacement reactions: from macroscopic observations to microscopic mechanisms. *Mineralogical Magazine*, 66(5):689–708.

Putnis, A. and Austrheim, H. (2010). Fluid-induced processes: metasomatism and metamorphism. *Geofluids*, 10:254–269.

Ragnhildstveit, J. and Helliksen, D. (1997). Geological map of Norway, bedrock map Bergen, scale 1:250 000.

Ramsay, C. R. and Davidson, L. R. (1970). The Origin of Scapolite in the Regionally Metamorphosed Rocks of Mary Kathleen, Queensland, Australia. *Contributions to Mineralogy and Petrology*, 25:41–51.

Rockow, K. M., Haskin, L. A., Jolliff, B. L., and Fountain, D. M. (1997). Constraints on element mobility associated with the conversion of granulite to eclogite along fractures in an anorthositic complex on Holsnøy, Norway. *Journal of Metamorphic Geology*, 15:401–418.

Roffeis, C., Corfu, F., and Austrheim, H. (2012). Evidence for a Caledonian amphibolite to eclogite facies pressure gradient in the Middle Allochthon Lindås Nappe, SW-Norway. *Contributions to Mineralogy and Petrology*, 164:81–99.

Romer, R., Martinsson, O., and Perdahl, J.-A. (1996). Scapolite: a tracer for the initial lead isotopic composition in sulfide deposits with later additions of radiogenic lead. *Mineralium Deposita*, 31:134–139.

Rosman, K. J. R. and Taylor, P. D. P. (1998). Isotopic Compositions of the Elements 1997. *Journal of Physical and Chemical Reference Data Reprints*, 20:1275–1287.

Rozen, O. M., Sidorkenko, S. A., and Kuznetsova, N. N. (1977). Scapolite and apatite as indexes of composition of volatile components at metamorphization of granulitic complex of Kola Peninsula. *Doklady Akademii Nauk SSSR*, 237(2):441–444.

Rudnick, R. L. and Taylor, S. R. (1987). The Composition and Petrogenesis of the Lower Crust: A Xenolith Study. *Journal of Geophysical Research*, 92(B13):13981–14005.

Rye, R. O. and Ohmoto, H. (1974). Sulfur and Carbon Isotopes and Ore Genesis: A Review. *Economic Geology*, 69:826–842.

Sandvik, K. O. (1977). Befaringer av malmforekomster, Hordaland, Norges Geologiske Undersøkelse, rapport nr. 1560/17C. Technical report, Norges Geologiske Undersøkelse.

Serdyuchenko, D. P. (1975). Some Precambrian scapolite-bearing rocks evolved from evaporites. *Lithos*, 8:1–7.

Stolz, A. J. (1987). Fluid activity in the lower crust and upper mantle: mineralogical evidence bearing on the origin of amphibole and scapolite in ultramafic and mafic granulite xenoliths. *Mineralogical Magazine*, 51:719–732.

Teertstra, D. K., Schindler, M., Sherriff, B. L., and Hawthorne, F. C. (1999). Silvialite, a new sulfate-dominant member of the scapolite group with an Al-Si composition near the I4/m-P4_2/n phase transition. *Mineralogical Magazine*, 63(3):321–329.

Teertstra, D. K. and Sherriff, B. L. (1996). Scapolite cell-parameter trends along the solid-solution series. *American Mineralogist*, 81:169–180.

Teertstra, D. K. and Sherriff, B. L. (1997). Substitutional mechanisms, compositional trends and the end-member formulae of scapolite. *Chemical Geology*, 136:233–260.

Van Wyck, N., Valley, J., and Austrheim, H. (1996). Oxygen and carbon isotopic constraints on the development of eclogites, Holsnøy, Norway. *Lithos*, 38:129–145.

von Knorring, O. and Kennedy, W. Q. (1958). The mineral paragenesis and metamorphic status of garnet-hornblende-pyroxene-scapolite gneiss from Ghana (Gold Coast). *Mineralogical Magazine*, 31(241):846–859.

Wilson, A. F. (1969). Problems of exploration for metals in granulite terrains, with particular reference to Australian localities. *Geological Society of Australia, Special Publications No. 2*, pages 375–376.

Wilson, A. F. (1974). The mineral potential of granulite terranes and other highly metamorphosed segments of the Earth's crust. In *Centenaire de la Société Géologique de Belgique, Géologie des Domaines Cristallins*, pages 301–321, Liège.

Yoshino, T. and Satish-Kumar, M. (2001). Origin of scapolite in deep-seated metagabbros of the Kohistan Arc, NW Himalayas. *Contributions to Mineralogy and Petrology*, 140:511–531.